Validation and Quantification of cardiac parameters obtained by cine MR imaging in crustaceans

Master-Thesis

Sebastian Gutsfeld | 1996142
M.Sc. Technical Biology

ALFRED-WEGENER-INSTITUT
HELMHOLTZ-ZENTRUM FÜR POLAR- UND MEERESFORSCHUNG

TECHNISCHE UNIVERSITÄT DARMSTADT

Sebastian Gutsfeld
Matrikelnummer: 1996142
Studiengang: M.Sc. Technical Biology

Master-Thesis
Thema: Validation and quantification of cardiac parameters obtained by cine MR imaging in crustaceans

Eingereicht: 22.10.2018

Betreuer/in extern: Dr. Christian Bock

Betreuer/in: PD Dr. Michael Heethoff

Prof. Dr. Gerhard Thiel

Fachbereich Biologie
Schnittspahnstraße 10
64287 Darmstadt

Erklärung zur Abschlussarbeit gemäß § 23 Abs. 7 APB der TU Darmstadt

Hiermit versichere ich, Sebastian Gutsfeld, die vorliegende Master-Thesis / Bachelor-Thesis ohne Hilfe Dritter und nur mit den angegebenen Quellen und Hilfsmitteln angefertigt zu haben. Alle Stellen, die Quellen entnommen wurden, sind als solche kenntlich gemacht worden. Diese Arbeit hat in gleicher oder ähnlicher Form noch keiner Prüfungsbehörde vorgelegen.

Mir ist bekannt, dass im Falle eines Plagiats (§38 Abs.2 APB) ein Täuschungsversuch vorliegt, der dazu führt, dass die Arbeit mit 5,0 bewertet und damit ein Prüfungsversuch verbraucht wird. Abschlussarbeiten dürfen nur einmal wiederholt werden.

Bei der abgegebenen Thesis stimmen die schriftliche und die zur Archivierung eingereichte elektronische Fassung überein.

Bei einer Thesis des Fachbereichs Architektur entspricht die eingereichte elektronische Fassung dem vorgestellten Modell und den vorgelegten Plänen.

English translation for information purposes only:

Thesis Statement pursuant to § 23 paragraph 7 of APB TU Darmstadt

I herewith formally declare that I, Sebastian Gutsfeld, have written the submitted thesis independently. I did not use any outside support except for the quoted literature and other sources mentioned in the paper. I clearly marked and separately listed all of the literature and all of the other sources which I employed when producing this academic work, either literally or in content. This thesis has not been handed in or published before in the same or similar form.

I am aware, that in case of an attempt at deception based on plagiarism (§38 Abs. 2 APB), the thesis would be graded with 5,0 and counted as one failed examination attempt. The thesis may only be repeated once.

In the submitted thesis the written copies and the electronic version for archiving are identical in content.

For a thesis of the Department of Architecture, the submitted electronic version corresponds to the presented model and the submitted architectural plans.

Datum / Date: Unterschrift/Signature:

_____ _____

Contents

Zusammenfassung

Marine Lebewesen und Ökosysteme müssen in Zukunft in den Weltmeeren nicht nur mit steigenden Temperaturen, sondern auch mit einer zunehmenden Anreicherung von CO_2 zurechtkommen.

Im Rahmen dieser Studie wurde untersucht, ob sich unter CO_2 Einfluss das Temperaturtoleranz-Fenster des Taschenkrebses, *Cancer pagurus*, in seinem Habitat in der Nordsee verändert. Dafür wurde eine Temperaturrampe verwendet, die Temperaturschwankungen, welche im Laufe eines Tages in der Nordsee vorkommen können, simulieren soll und deshalb auch Akklimatisierungseffekte berücksichtigt. Die Temperaturrampe reichte deshalb von 12-20°C, wobei Erwärmungsschritte immer in 2°C Schritten binnen 2 Stunden durchgeführt wurden. Einzelne Temperaturschritte wurden jeweils für 10 Stunden gehalten, wobei die ersten 5 Stunden als Akklimatisationszeit und die zweiten 5 Stunden als Messzeit genutzt wurden. Die Versuchstiere wurden dabei CO_2 Levels ausgesetzt, die die heutigen Bedingungen (ca. 480 µatm) und prognostizierte Bedingungen nach 2100 (ca. 1400 µatm) repräsentieren. Mithilfe eines multi-parametrischen Versuchsaufbaus konnten hochaufgelöste und kontinuierliche Daten der Sauerstoffverbrauchsrate, der Herzrate, des Herzschlagvolumens und der Herzleistung nicht-invasiv aufgenommen, beziehungsweise berechnet werden. Dies ermöglichte Untersuchungen darüber, wie die aerobe Stoffwechselrate und das Herz-Kreislaufsystem als Schlüssel-Komponenten der Leistungsfähigkeit im Laufe eines Tages durch Temperaturanstiege und verschiedene CO_2 Partialdrücke moduliert werden. Da im Rahmen dieser Messmethoden allerdings nur relative Änderungen des Schlagvolumens bestimmt werden konnten, wurde versucht einen nicht-invasiven Ansatz zur Quantifizierung des Schlagvolumens mit Hilfe von cine-Magnetresonanztomographie zu definieren. Dieser Ansatz konnte darüber hinaus auch komplexe innere Strukturen des Herzmuskels identifizieren, die wahrscheinlich die Effizienz des Pump-Mechanismus verstärken.

Trotz der hohen inter-individuellen Variabilität der Versuchstiere konnten beispielhaft an den Herzraten durchgeführte Analysen zeigen, dass die temperaturabhängig steigenden Amplituden der rhythmischen Muster (ausgebildet bei aerobem Metabolismus) auf steigenden Leistungsmaxima beruhen, während die Minima konstant bleiben. Außerdem konnte ein temperaturabhängiger Wechsel von niedrigen zu hohen Frequenzen gezeigt werden.

Neben diesen temperaturabhängigen Effekten konnte gezeigt werden, dass CO_2-Konzentrationen von ca. 1400 µatm über die Zeit leicht narkotische Effekte auf die Herzaktivität von *C. pagurus* haben.

Da die anderen Parameter allerdings keine einheitlichen Reaktionen zeigen und keine CO_2-abhängigen Änderungen der Temperatureffekte beobachtet werden konnten, legen diese Ergebnisse nahe, dass die projizierten CO_2-Level in der Nordsee über das Jahr 2100 hinaus das Temperaturtoleranz-Fenster des Taschenkrebses nicht verringern.

Abstract

In future oceans, aquatic animals and marine ecosystems will have to cope with combined effects of ongoing warming and CO_2 accumulation. This study investigated possible effects of ambient CO_2 on the thermal tolerance window of the North Sea edible crab *Cancer pagurus*. To enhance ecological relevance, the temperature ramp was chosen to mimic daily temperature changes and allow for acclimation effects. Applied temperatures ranged from 12°C to 20°C with 2°C warming steps (within 2 hours). Temperature steps were held for 10 hours including 5 hours acclimation time and 5 h measurement time. Animals were exposed to present day normocapnia (ca. 480 µatm) and CO_2 levels projected beyond 2100 (ca. 1400 µatm). Using a multi-parameter approach (measured/calculated parameters: metabolic rate, heart rate, cardiac stroke volume proxy, cardiac output proxy) enabling non-invasive recording of highly resolved and continuous data, it was investigated how aerobic metabolic rate and the cardiovascular system as key components of animal performance are modulated on a daily basis by changes in temperature and ambient CO_2. As non-invasive measurements only allowed for detection of relative changes in cardiac stroke volume, an approach for non-invasive quantification using cine magnetic resonance imaging (MRI) is presented. This approach further revealed complex inner structures of the ventricle likely enhancing efficiency of the pumping mechanism.

Despite high interindividual variability, exemplary analysis of the heart rate over time could reveal, that increasing amplitudes of rhythmic patterns (representing aerobic metabolism) in response to rising temperatures mostly depended on increases at the maximum level of performance, whereas minimum levels remained stable. Additionally, temperature-dependent changes from low to high frequencies could be observed.

Beside these temperature-dependent effects, it could be shown, that CO_2-concentrations around 1400 µatm can have light narcotic effects on the heart activity over time of *C. pagurus*. The diverse responses of the other parameters and no apparent CO_2-dependent shifts in the performance response to temperature imply, that projected CO_2 levels in the North Sea beyond the year 2100 do not narrow the thermal tolerance window of *C. pagurus*.

List of Abbreviations

$[B]_T$	Total boron concentration
$[HCO_3^-]_w$	Bicarbonate concentrations in seawater
°C	Degree Celsius
µatm	Micro atmosphere
µm	Micrometer
3D	Three dimensional
A	Ampere
A.U.	Arbitrary units
A/D	Analog to digital
ALA	Anterolateral arteries
ATP	Adenosine-5´-triphosphate
BCV	Branchiocardiac veins
bpm	Beats per minute
c	Concentration
CH_4	Methane
cine	Cinematic
cm	Centimeter
CO_3^{2-}	Carbonate ion
CO_2	Carbon dioxide
COP	Cardiac output proxy
CT_{max}	Critical thermal maximum
DIC	Dissolved inorganic carbon
Fc	Flow compensated
FFT	Fast Fourier Transform
FLASH	Fast low angle shot
g	Gram
GHG	Global greenhouse gas
Gt	Gigatonnes
h	Hour
H^+	Hydrogen ion/proton
HA	Hepatic arteries
HCO_3^-	Hydrogen carbonate/bicarbonate ion
HFC	Hydrofluorocarbon
Hz	Hertz
IR-PPG	Infrared photo plethysmography
K_1	First dissociation constant of carbonic acid (mol/kg)
K_2	Second dissociation constant of carbonic acid (mol/kg)
kg	Kilogram
KSO_4	Potassium sulfate
L	Liter
LED	Light emitting diode
m	Meter
min	Minute(s)
mL	Milliliter
mm	Millimeter
$\dot{M}O_2$	Metabolic- /respiration- / oxygen consumption rate
mol	Mol
MRI	Magnetic resonance imaging
n	Group size
N_2	Nitrogen

N_2O	Nitrous oxide
O_2	Oxygen
OCLTT	Oxygen- and capacity-limited thermal tolerance
OWA	Ocean warming and acidification
$P(CO_2)$	Partial pressure of CO2
$P(CO_2)_w$	Partial pressure of CO2 in sewater
PA	Posterior aorta
PFC	Perfluorocarbon
pH	$-\log_{10}[H^+]$
pH_w	Seawater pH (free scale)
$P(O_2)$	Partial pressure of oxygen
P_{air}	Air pressure
P_{wv}	Vapor pressure of water
RF	Resonance frequency
RMR	Routine metabolic rate
s	Second(s)
SA	Sternal artery
sccm	Standard Cubic Centimeters per Minute
SF_6	Sulphurhexafluoride
SMR	Standard metabolic rate
spMR	Spontaneous metabolic rate
SVP	Stroke volume proxy
SW	Seawater
T	Tesla
T	Temperature
T_c	Critical temperature
T_d	Denaturation temperature
T_p	Pejus temperature
V·s	Volt times seconds
V_{amp}	Voltage amplifier
$\dot{V}w$	Water flow
w_f	Fresh weight
α	Solubility coefficient
$\Delta P(O_2)$	Difference in oxygen partial pressure

Figures and Tables

Figures

Tables

1. Introduction

1.1 Impacts of climate change on marine ecosystems

Since the beginnings of industrialization, the global greenhouse gas (GHG) emissions (comprising carbon dioxide (CO_2), methane (CH_4), nitrous oxide (N_2O), hydrofluorocarbons (HFCs), perfluorocarbons (PFCs) and sulphurhexafluoride (SF_6)) have constantly grown due to human activities. An increase of 70% in emissions was observed between 1970 and 2004. GHGs enhance warming effects in the atmosphere, as they allow for short-wavelength radiation emitted by the sun to pass onto the earth surface, but absorb the subsequent infrared radiation emitted from there. Due to Kirchhoff´s law of thermal radiation, the heated GHGs emit infrared radiation themselves, with a considerable amount towards the earth surface. This additional radiation enhances warming of the land and water surfaces beyond levels which would be reached by short-wavelength radiation alone (IPCC 2007). Between 1979 and 2012, the global average sea surface temperatures increased by 0.12°C per decade (Hartmann *et al.* 2013).

The oceans play an important role with regard to global warming trends, as they actively act as sinks for heat. Since 1960, the net amount of heat absorption of the oceans was about 20 times higher than the heat absorption of the atmosphere (Levitus *et al.* 2005). Simultaneously ongoing deforestation combined with increased rates of fossil-fuel-burning have led to increasing atmospheric concentrations of CO_2, one of the most important anthropogenic GHG, due to its high-quantity emission (Ciais *et al.* 2013; Doney *et al.* 2009).

Between 1970 and 2004 its annual emissions have grown by about 80%, from 21 to 38 Gt, representing 77% of total anthropogenic GHG emissions in 2004 (IPCC 2007). Generally, atmospheric amounts of CO_2 grew by 40% since 1750 (Hartmann *et al.* 2013).

These values should have been even higher, if not for the oceans absorbing up to one third of the additional atmospheric CO_2 and therefore effectively acting as sinks (Sabine and Feely 2007).

However, increasing amounts of CO_2 in the seawater lead to alterations of the carbonate chemistry in the following ways:

$$CO_2 + H_2O \leftrightarrow H_2CO_3 \overset{aq.}{\leftrightarrow} H^+ + HCO_3^- \quad [1]$$

$$HCO_3^- \overset{aq.}{\leftrightarrow} H^+ + CO_3^{2-} \quad [2]$$

Increases in ambient CO_2 ($P(CO_2)$) are termed hypercapnia. Under hypercapnic conditions, the amount of $[H^+]$ increases and causes a decrease in seawater pH, a process called ocean acidification (Doney *et al.* 2009). As a general response to increasing CO_2 concentrations in seawater, concentrations of bicarbonate buffers (HCO_3^-) will slightly increase, whereas concentrations of carbonates (CO_3^{2-}) decrease.

Effects of hypercapnic conditions on energy metabolism of aquatic animals can range from metabolic depression (Michaelidis *et al.* 2005; Pörtner *et al.* 1998; Pörtner *et al.* 2005; Pörtner *et al.* 2004) over no changes (Gutowska *et al.* 2008; Lannig *et al.* 2010) to increases in metabolic rates (Thomsen and Melzner 2010; Walther *et al.* 2009) across different species, indicating different strategies in response to ocean acidification (Melzner *et al.* 2009; Whiteley 2011).

In future oceans, aquatic animals will have to cope with combined effects of ongoing warming and acidification. For the North Sea as a shallow sea in particular, bottom water temperatures are projected to warm > 1°C with a simultaneous drop in surface water pH of 0.12 until the year 2055 (RCP8.5; Earth Systems Research Laboratory 2018). These changes may not only have severe effects on the species, but also on ecosystem levels. Projected effects include shifts in geographical distribution to increasing risks of local extinctions of species or even entire ecosystems like coral reefs (Hoegh-Guldberg 2005; Parmesan and Yohe 2003; Perry *et al.* 2005).

1.2 The edible crab, *Cancer pagurus*

1.2.1 Morphology and ecology

The edible crab, *Cancer pagurus* (Linnaeus 1758) belongs to the subphylum Crustacea, order Decapoda and infraorder Brachyura. Adult *C. pagurus* can reach a carapace width of around 27 cm and are colored reddish-brown (**Fig. 1**; Neal and Wilson 2008). It is found in sublittoral regions in the North East Atlantic from Norway to Morocco, even occurring in the Mediterranean Sea (**Fig. 2**).

For animals living in the German Bight in sublittoral regions near Helgoland in particular, temperatures can range from 8°C to 20°C during the course of the year, with highest temperatures reached during summer times. The annual average temperature reported for this region is 12°C (COSYNA 2018).

As nocturnal predators and scavengers, their food includes a broad variety of prey, such as other crustaceans, smaller members of their own species, molluscs, like the blue mussel *Mytilus edulis* or the European oyster *Ostrea edulis*, or simply any dead matter they come across (Neal and Wilson 2008). Sexual maturity is reached with a carapace width of about 11-13 cm, whereby a clear sexual dimorphism is shown. The abdomen folded under the thorax of females has a wide round shape, whereas in males it is more narrow and pointed (Kaestner *et al.* 1970).

Fig. 1: Anterior view of *C. pagurus*. The displayed individual had a carapace width of 18 cm and weighted ca. 400 g.

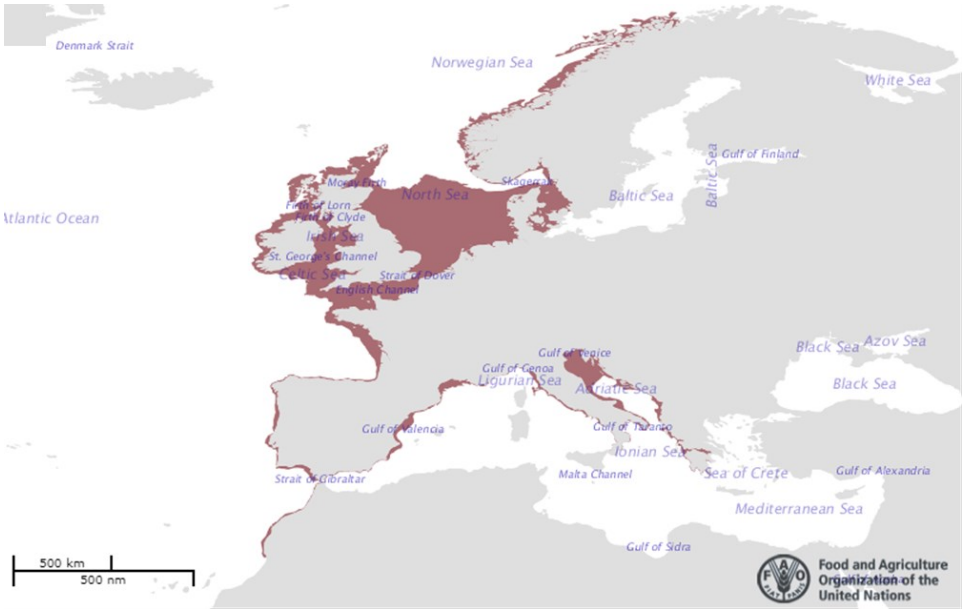

Fig. 2: Geographical distribution of the edible crab *C. pagurus* (red areas). Source: Food and Agriculture Organization of the United Nations.

1.1.2 Open circulatory system of decapod crustaceans

The general open circulatory system, roughly fits *C. pagurus* as well as other members of the brachyuran (**Fig. 3**; (Maynard 1960). While they technically possess an open haemocoel, they show a high degree of vascularization. Despite well-established arteries, venous structures are simply formed by cavities of their shell (see below), so the organs are still bathed in the circulated fluid, called hemolymph (McGaw 2005). Analogous to vertebrate blood, crab hemolymph is responsible for the transport of respiratory gases, nutrients and waste products. The total volume of hemolymph varies between 20-50% of the total volume of the animal (Taylor and Wheatly 1982). The decapod crustacean circulatory system contains some level of adjustability and its efficiency may be comparable to closed systems of equally sized vertebrates (McMahon and Burnett 1990; Taylor 1982). The efficiency is visible in the 3-4 times higher cardiac output at an up to 10 times higher hemolymph volume compared to vertebrate blood volume. These two properties compensate for the relatively lower oxygen carrying capacity of crustacean hemolymph, limited by the low oxygen binding capacity of hemocyanin (the arthropod respiratory blood pigment). This results in a comparable total capacity-per-unit-mass between fish and crustaceans (Taylor 1982).

The decapod crustacean circulatory system possesses different arterial systems, originating from the heart, spreading into fine, capillary-like structures, which are especially well developed around the central nervous system. In larger and active species, these small vessels can have 2-10 µm in diameter (Sandeman 1967). The arterial system supplies organs and tissues with oxygenated hemolymph (**Fig. 3**, **Fig. 4**).

After systemic circulation, the hemolymph flows into interstitial spaces and ventral lacunae and subsequently over large sinuses into the infrabranchial sinus (**Fig. 3**). This sinus runs ventrally on both sides of the body and is connected to the locomotory appendages of each segment.

The infrabranchial sinus supplies and obtains hemolymph from the limbs, but also serves it to the afferent branchial sinuses of the gills. In the gills, the hemolymph gets reoxygenated and accumulates in the branchiopericardial veins (**Fig. 3**). These veins are connected to the pericardial sinus and from there, the hemolymph enters the heart again through valved ostia at diastole for subsequent recirculation (Taylor 1982).

The heart itself is upheld by suspensory ligaments in the pericardial sinus. Contraction at systole works against the elasticity of these ligaments. The filling of the heart at diastole relies on elastic recoil, with hemolymph entering via the ostia from the pericardial sinus (Wilkens 1981). The cardiac stroke volume resulting from this process is controlled by Sterling´s law, corresponding to heart rates and modifying cardiac output. It is adjustable through nervous and hormonal control (Taylor 1982).

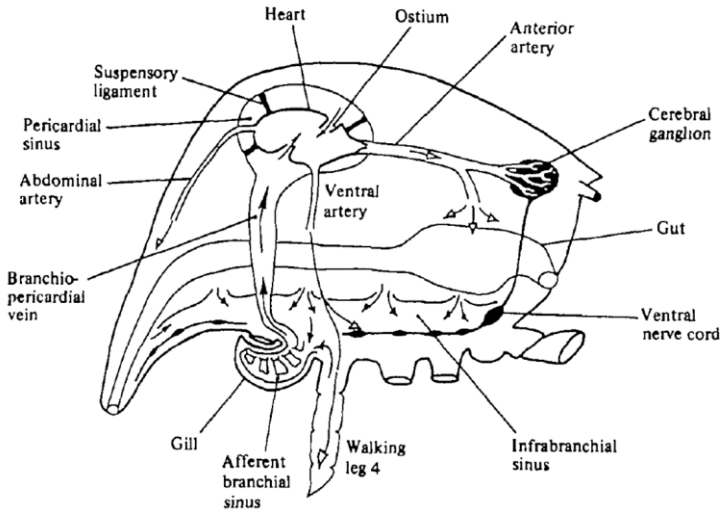

Fig. 3: General circulation in decapod crustaceans. Open arrows indicate arterial flow (from the heart to the supplied tissues), whereas closed arrows show the venous return via the gills. The principle of supply for the appendages is shown by example for one walking leg and its particular gill. Taken from Taylor (1982).

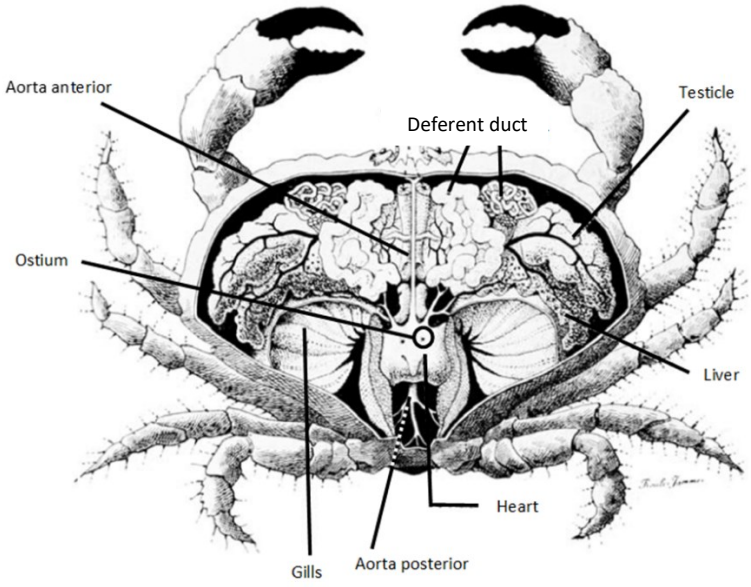

Fig. 4: Anatomical overview over specific organs and vessels of *C. pagurus.* Taken and modified from Roule (1898).

The gas exchange with the environment effected at the gills (**Fig. 3**, **Fig. 4**, **Fig. 5**). In brachyuran crabs, they are encased in branchial chambers called branchiostegites and can be delineated as folds of the body wall. The gills themselves are connected to the major appendages like the walking legs and the chelipeds (Dejours 1975).

Since gas exchange relies on passive diffusion across the gill epithelia, the gills possess an elaborate design, minimizing diffusion distance at maximum surface area for an efficient gas exchange (Taylor 1982). However, gas exchange can be facilitated by enhanced ventilation, ensuring a high diffusion gradient from oxygen-rich water to oxygen-depleted body fluids.

To move water through the branchial chamber, decapod crustaceans developed a specialized appendage, the scaphognathite, which is the flattened exopodite of the second maxilla (**Fig. 5**; Young 1975). The scaphognathite oscillates dorsoventrally, creating a pulsatile hydrostatic pressure, sucking water through openings around the bases of the walking legs into the branchial chambers over the gills (McDonald *et al.* 1977; Taylor 1982; Taylor and Wheatly 1980).

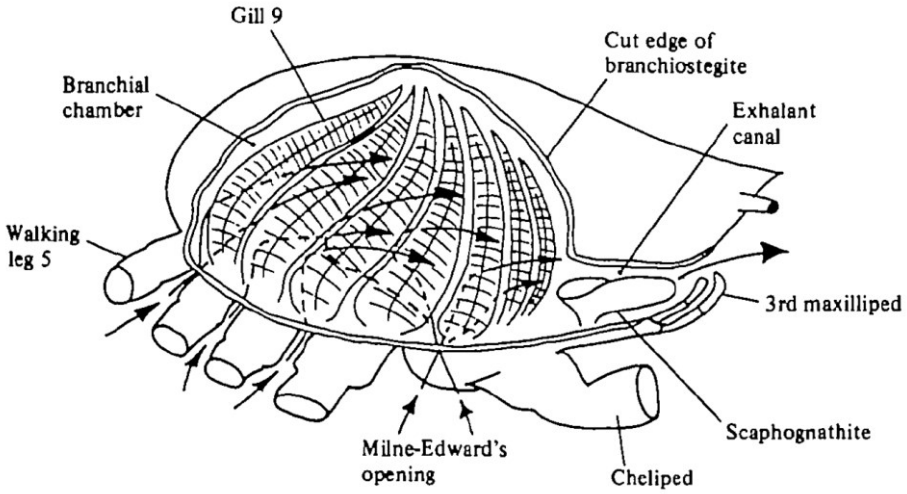

Fig. 5: Water flow and functional anatomy of the gills in decapod crustaceans. The branchiostegite has been removed. Water enters at the bases of the walking legs and flows over the gill lamellae into the epibranchial space, where it gets drawn forward by the oscillating scaphognathite and outcasted anteriorly. Taken from Taylor (1982).

Blood perfusion of the gills depends on the performance of the heart. Unlike vertebrates, crustacean hearts do not possess a myogenic pacemaker, and display no propagating muscle action potentials (Taylor 1982). Muscle contraction in crustaceans originates in a number of motor endplates on the muscle fibers, which induce cumulative depolarizations of their membranes (Fatt and Katz 1953; Hoyle and Wiersma 1958).

To achieve simultaneous contraction of all necessary muscle fibers at systole, a burst of propagated action potentials is sent from cumulative neurons located in the dorsal wall of the heart. This group of neurons is also termed as the cardiac ganglion (Maynard 1960; Van Der Kloot 1970).

When resting and undisturbed, many decapod crustaceans display rhythmic patterns of metabolic activity: Spontaneous peaks in overall physiological performance are interrupted by apnoea and bradycardia, or cardiac arrest (Bradford and Taylor 1982; McMahon and Wilkens 1977). This behavior showed high variability within and between species (i.e. Bradford and Taylor 1982; Burnett and Bridges 1981; McMahon and Wilkens 1977).

The presence of rhythmic patterns represents the resting state of decapod crustaceans in which metabolic energy is saved by reducing the energy costs of pumping water (through ventilation) and hemolymph (through the cardiovascular system; Bradford and Taylor 1982; Burnett and Bridges 1981; McMahon and Wilkens 1977).

As onsets of respiratory pauses immediately result in decreases in heart rate, the cardioregulatory system has a functional connection to the respiratory system, which may have implications on general whole animal performance (McMahon and Wilkens 1977; McMahon and Wilkens 1972; Taylor *et al.* 1973). First evidence for this neural link comes from Wilkens *et al.* (1974), who identified command fibers which trigger activity in hearts and scaphognathites at the same time after electrical stimulation.

1.3 Metabolic rate and respiration

Metabolic rate describes the heat production of catabolic processes, including both, aerobic and anaerobic processes (Fry 1971). Over a longer period of time, aerobic metabolism displays the only way to sustain animal life. Therefore, measurements of oxygen consumption rates provide reliable proxies for energy demand and metabolic rate. Besides the utilization of oxygen for oxidative phosphorylation, 20-40% of basal oxygen consumption can be consumed in other cellular processes, e.g. in proton permeability of the mitochondrial inner membrane (Brand 1990; Nobes *et al.* 1990). Therefore, whole-animal metabolic rate, which includes all these processes, is usually equivalent to oxygen-uptake- or respiration rate. It should be noted however, that these two parameters still derive from different concepts. Considering the whole-organism level, respiration rates describe the integral of all energy consuming processes. This may result in decreasing qualitative significance, since total metabolic rates can remain stable due to summation of depressed and elevated metabolic processes from different tissues. However, metabolic rates remain valuable measures for the physiological states of animals (Fry 1971).

Minimum respiration rates, sustained over an extended period of time without the necessity of acquisition of additional sources of energy in a resting, post-absorptive animal are defined as standard metabolic rates (SMR). These SMRs comprise the oxygen- and energy demands of resting cells and mechanisms maintaining their functioning (Brand 1990; Fry 1971). Additionally, spontaneous and unforced onsets of restricted activity cause routine (or spontaneous) metabolic rates (RMR or spMR).Both can be determined from time series of respiration rates (Breteler 1975; Fry 1971; Maus *et al.* 2018).

1.4 The Concept of Oxygen- and Capacity-Limited Thermal Tolerance (OCLTT)

Since temperature exerts an influence on any level of biological organization, it is crucial to consider mechanisms occurring on the different levels of organization (i.e. from cells to tissues and whole-animal levels), their cumulative impact and therefore their influence on shaping the overall thermal limitations of an organism in the context of its ecosystem (Hochachka and Somero 2002; Pörtner *et al.* 2017). One prominent concept dealing with the physiological consequences changing habitat temperatures is first described as a thermal tolerance concept in *Maja squinado* by Frederich and Pörtner (2000). They proposed thermal tolerance thresholds, matched by limits for aerobic performance of temperature dependent heart- and ventilation rates, and temperature dependent hemolymph oxygen partial pressure (Frederich and Pörtner 2000; Walther *et al.* 2009).

The apparent influence of tissue oxygenation and oxygen transport capacities on thermal tolerance of ectothermic animals refined this concept to what is now known as oxygen- and capacity-limited thermal tolerance (OCLTT). Briefly, constant warming or cooling of an animal's environment towards limiting values leads to restrictions on the animal's capacity to sufficiently supply oxygen to the tissues. This results in a mismatch of oxygen demand and -delivery, and subsequently in a progressive decline in performance (Giomi *et al.* 2014; Pörtner *et al.* 2017; Pörtner and Giomi 2013). Based on that principle, animals at their thermal optimum can fulfill their energy needs under standard metabolic rates (SMR) by aerobic metabolism.

Fig. 6 shows how the OCLTT can be applied to *M. squinado* (Frederich and Pörtner 2000). It should be noted, that the shape of the curve differs between species, but the described parameters are considered applicable across phyla.

Optimal temperatures for an animal are reflected in peak steady state aerobic performance (as shown by maximum body fluid $P(O_2)$). The temperature range which can be permanently tolerated is known as active thermal tolerance window. Processes which are supported within the active thermal tolerance window are for example cardiovascular scope and –cost and metabolism (grey box, **Fig. 6**; Pörtner *et al.* 2017).

Towards higher or lower temperatures, the above-mentioned mismatches between oxygen demand and -delivery will limit aerobic capacities, effectively reducing an animal's performance and thus its active thermal tolerance. The loss of maximum aerobic performance is defined to occur beyond the pejus temperatures (T_p, **Fig. 6**). Beyond upper and lower T_p, active thermal tolerance is shifted to passive thermal tolerance (solid arrows, **Fig. 6**), marked by a decline in the steady state aerobic window, and venous $P(O_2)$.

At temperatures beyond critical thresholds (T_c), anaerobic metabolism sets in, eventually causing oxidative stress, triggering the heat shock response. As these reactions rely on finite resources when feeding is restricted, passive thermal tolerance is limited in time. Despite these properties, this part of the thermal window may be commonly experienced, especially in the intertidal, with daily temperature changes involving a less-than-optimal temperature range (Pörtner *et al.* 2017).

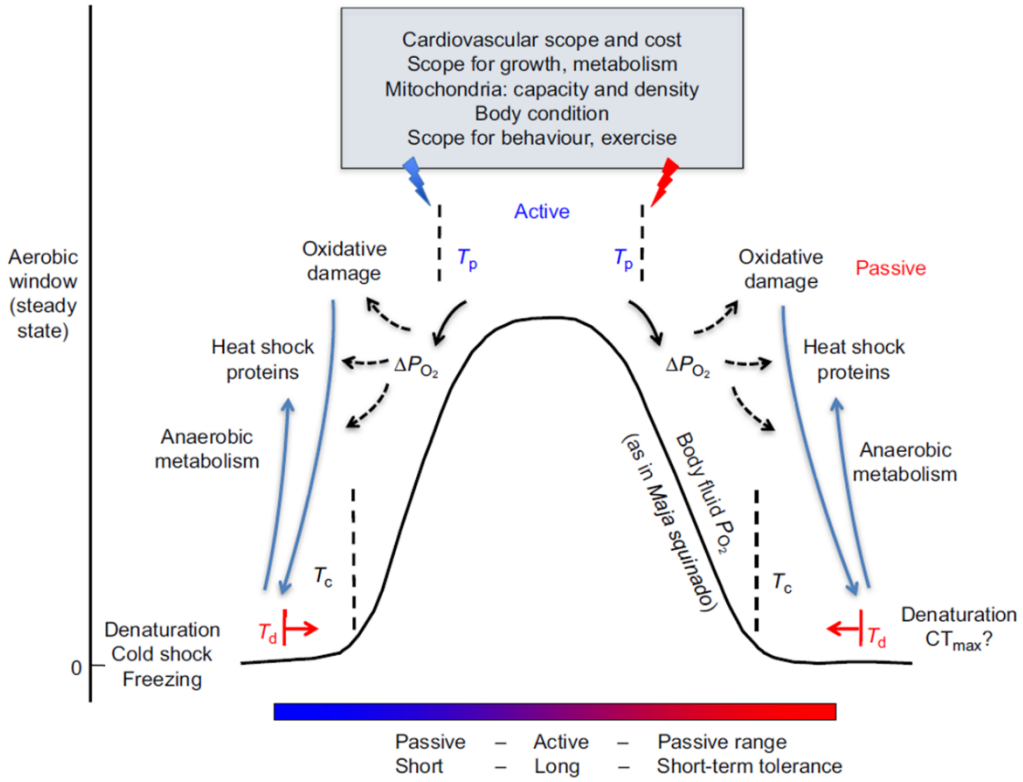

Fig. 6: Concept of oxygen- and capacity-limited thermal tolerance (OCLTT). The black curve shows the body fluid $P(O_2)$ of *M. squinado* against body temperature (Frederich and Pörtner 2000). The grey box lists processes which are supported under active thermal tolerance. The performance of these processes is reduced by reaching pejus temperatures (T_p). Solid black arrows indicate the transition to passive thermal tolerance. Dashed black arrows indicate the induction of oxidative damage, heat shock protein expression and anaerobic metabolism. Blue arrows indicate the onset of these processes after reaching critical temperature. Red arrows indicate shifts of denaturation temperatures (T_d) likely due to whole-organism feedbacks. CT_{max}, critical thermal maximum. Taken from Pörtner et al. (2017).

To finally apply the OCLTT concept to current challenges under climate change, it is not only necessary to consider changes in temperatures, but also other abiotic drivers, such as acidification of the oceans (see above). Metzger et al. (2007) showed, that exposure of *C. pagurus* to 1% atmospheric CO_2 (10000 µatm CO_2) shifts pejus- and critical temperatures to values 5°C below control $P(CO_2)$ (measured by arterial oxygen tension). These results show, that acidification can cause a narrowing of the thermal window.

Despite this principal evidence for the effects of acidification, 10000 µatm CO_2 are beyond what can be expected for average surface ocean CO_2 levels. For the year 2100 projections assume 700-1000 µatm CO_2 for atmospheric and surface ocean levels, for 2300 values around 3000 µatm CO_2 are considered (Orr *et al.* 2001). Walther *et al.* (2009) used these projections of anthropogenic CO_2 accumulation to predict possible impacts on the thermal tolerance window of spider crabs *Hyas araneus*. Therefore, they measured temperature-dependent changes in heart rate and hemolymph $P(O_2)$ under different CO_2 levels. The cardiovascular system is a key driver in oxygen uptake and distribution, so constraints in its performance likely result in reduced hemolymph $P(O_2)$ causing constraints in thermal tolerance. For the predicted CO_2 values of the near future they found a dose-dependent reduction of T_c, from >25°C under normocapnia to 23.5°C under 710 µatm and 21.1°C under 3000 µatm, recognized by breakpoints in heart rates. Considering these results, Walther *et al.* (2009) concluded, that even CO_2 levels projected for current ocean acidification can cause a narrowing of the thermal tolerance windows of crustaceans.

Maus *et al.* (2018) showed different levels of hemolymph flow in the central artery at steady heart rates of *Carcinus maenas* under different seawater carbonate systems. Taking these studies together, it should be noted, that acidification levels and their impact on cardiovascular should not be underestimated when investigating thermal tolerance windows.

1.5 Aim of the study

This study shall investigate the performance response of the cardiac system of sublittoral *C. pagurus* to future climate change conditions, regarding temperature changes and CO_2 levels. Previous studies focused on mechanistic principles by investigating specific physiological parameters over rapidly induced temperature changes (e.g. Walther *et al.* 2009), or considering only one parameter like arterial oxygen tension (Metzger *et al.* 2007). So far, little is known about the immediate interaction of several parameters shaping the thermal tolerance or key performance indicators like the cardiac system.

Since most studies on temperature responses in marine ectotherms choose monotonically, continuously increasing temperatures with rates around 1-3°C/h (Joyce *et al.* 2018; Madeira *et al.* 2016; Metzger *et al.* 2007; Walther *et al.* 2009), they aimed to exclude acclimation effects, as they focused on investigations of mechanistic principles. Ocean warming is a slow process, offering enough time to enable acclimations, and acclimation effects in decapod crustaceans already occur after 4-6 h (Cuculescu *et al.* 1998). These effects have to be considered when investigating physiological responses in an ecological context. To examine possible effects on the thermal tolerance window of *C. pagurus* under additional CO_2 exposure, it shall be investigated how aerobic metabolic rate and the cardiovascular system are modulated on a daily basis.

Since decapod crustaceans possess neurogenic pacemakers exhibiting changing patterns of cardiac performance as well as changing patterns of metabolic activity, it is of interest to see how these traits affect each other in response to changing environmental conditions. Besides improving the understanding of the physiological response to global warming, measurements across the reported upper pejus temperatures of this species will help to better understand how oxygen demand and allocation is affected by rising temperatures and modulated by CO_2. Due to neurogenic pacemakers, decapod crustaceans can modify their cardiac stroke volume, but non-invasive measurements can only detect for relative changes. Therefore, methods for non-invasive quantification of the stroke-volume shall be defined to provide references for relative changes and finally enable non-invasive quantification of all key parameters of heart performance. This will include cine magnetic resonance imaging (MRI) to visualize the heart beat in *C. pagurus* non-invasively.

2. Materials and Methods

2.1 Experimental animals

Edible crabs, *Cancer pagurus*, were caught in sublittoral zones (10-25 m) at the German Bight near Helgoland (North Sea, north-western Germany, 54° 11'' N, 7° 53''E) by the research vessel Uthörn (Alfred-Wegener-Institute, Helmholtz Centre for Polar- and Marine Research, Bremerhaven, Germany (AWI)). Until experimentation, *C. pagurus* were kept in aerated and recirculated seawater aquaria at ambient $P(CO_2)$ of ca. 400 µatm and constant temperature of 12°C at the AWI and were fed twice a week with frozen blue mussels (*Mytilus edulis*). Seven animals were used in total, from which four were employed for preliminary trials (Pre-group, **Tab. 1**), and three for the main experiments (Main-group, **Tab. 2**). Animals of the Main-group had an average weight of 358 ± 43 g and an average carapace width of 13 ± 0.46 cm.

All individuals were labeled prior to experimentation.

Tab. 1: Pre-group body parameters. The four individuals of the Pre-group described by three parameters: Sex, weight and carapace-width. Weight differed up to 57% between *Cancer* 3 and *Cancer* 7.

Animal	Sex	Weight (g)	Carapace-width (cm)
Cancer 2	f	337	12.7
Cancer 3	f	407	13.4
Cancer 6	f	249	11.4
Cancer 7	f	232	12.1

Tab. 2: Main-group body parameters. The three individuals of the Main-group described by three parameters: Sex, weight and carapace-width. Animals show no greater differences in weight and carapace-width.

Animal	Sex	Weight (g)	Carapace-width (cm)
Cancer 1	m	379	13.1
Cancer 4	f	308	12.5
Cancer 5	f	386	13.4

2.2 Respirometry and cardiovascular performance experiments

2.2.1 General setup requirements

In order to measure the physiological response of *C. pagurus* to ocean warming and acidification (OWA) at the whole-animal level, the experimental setup should fulfill several criteria: Firstly, controllable and adjustable temperature and $P(CO_2)_w$ of the seawater. Secondly, constant flow of water through a respirometer chamber to ensure sufficient oxygen supply to the animal while still allowing for measurements of oxygen consumption rates. Thirdly, the implementation of simultaneous and continuous oxygen consumption- and heart rate measurements over the whole period of the experiments.

2.2.2 Experimental setup and experimental protocol

Prior to the start of the particular experiment, the animal was fixed on a plastic grid with zip ties to restrain movement, so that they cannot remove the sensors attached to them (see below; **Fig. 7**). To measure oxygen consumption rates ($\dot{M}O_2$) and the cardiovascular parameters, individual *C. pagurus* were placed in a respiratory chamber with a total water volume of 1870 mL (**Fig. 8**). After subtracting an average volume of 350 mL for one experimental animal, the approximate volume of the permanently circulated water was around 1520 mL (**Fig. 8**).

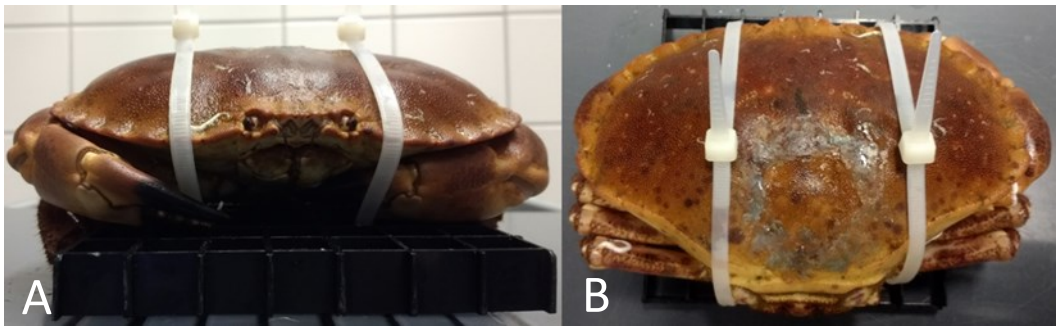

Fig. 7: Preparation of the experimental animal. The animal was fixed on a plastic grid with zip ties to restrain movement. (A) Frontal view (B) dorsal view.

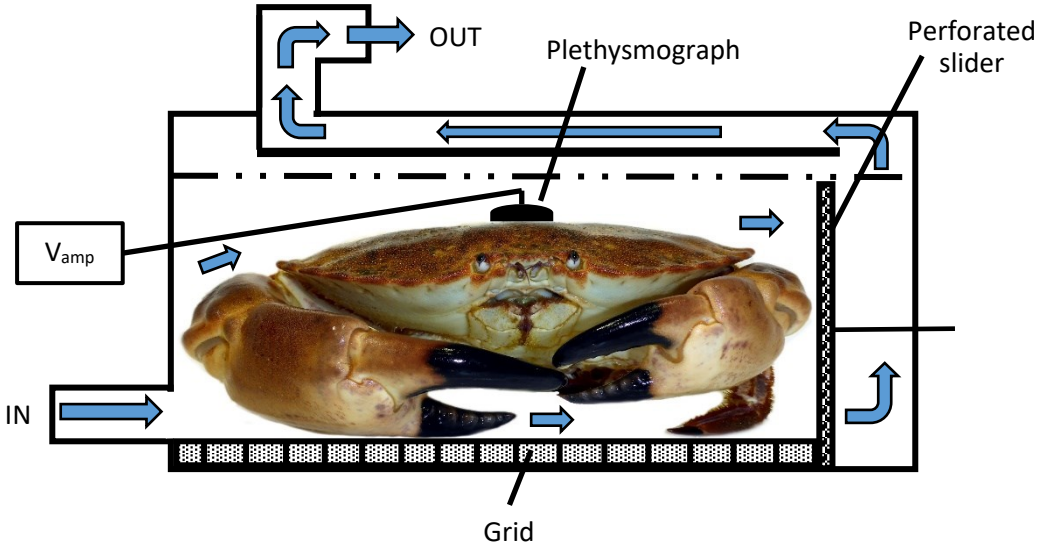

Fig. 8: Schematic setup of the respiratory chamber. The experimental animal was placed and fixed on a grid. Lateral movement was further restricted by a perforated slider. The plethysmograph used for heart rate measurements was placed on the carapace above the heart. Dashed lines indicate the inner edge of the lid. Blue arrows indicate water flow direction. V_{amp}, voltage amplifier.

The chamber was placed in a 50 L tank making sure the chamber is entirely submerged in seawater. The water temperature in the system was regulated by a thermostat (Lauda Eco RE 630; LAUDA DR. R. WOBSER GmbH & Co. KG, Germany; **Fig. 9**, **Fig. 10**).

A constant flow of water through the chamber was achieved by an aquarium pump with a maximum performance of 490 L/h (Eheim GmbH & Co. KG, Deizisau, Germany). The incorporated hoses had an inner diameter of 0.6 cm (Tygon S3 E3603 meets NSF-51 STD; Saint-Gobain, France), effectively reducing water flow through the system to 400-600 mL/min. During the experiments, the setup was covered by a lid to prevent visual disturbance of the animal.

Experiments were conducted under normo- (control, with water $P(CO_2)_w$ at present day levels) and hypercapnic conditions (elevated $P(CO_2)_w$). For the year 2100, 700-1000 µatm CO_2 are projected for atmospheric and surface ocean levels; for 2300 values around 3000 µatm CO_2 are projected (Orr *et al.* 2001). Based on these projections, the values set for normocapnic conditions were 483 µatm ± 16.75 µatm (controls) and for hypercapnic conditions they were 1367 µatm ± 13 µatm, representing conditions beyond 2100. Compared to previous studies that focused more on mechanistic principles (Metzger *et al.* 2007; Walther *et al.* 2009), the design of this study followed the intention to investigate ecologically relevant processes during *in situ* temperature changes.

$P(CO_2)_w$ for normocapnic conditions was achieved by permanent aeration of the water in the tank with ambient air using a membrane pump (Schego MK2K3 220-240 V ~ 50 Hz 5 W; SCHEGO Schemel & Goetz GmbH & Co KG, Offenbach, Germany). Hypercapnic conditions were created by using a mix of compressed air and CO_2 provided by a gas mixing device (ratio: air 3000 sccm, CO2 2.5-3 sccm; mks Instruments, Andover, MA, USA; **Fig. 9**, **Fig. 10**).

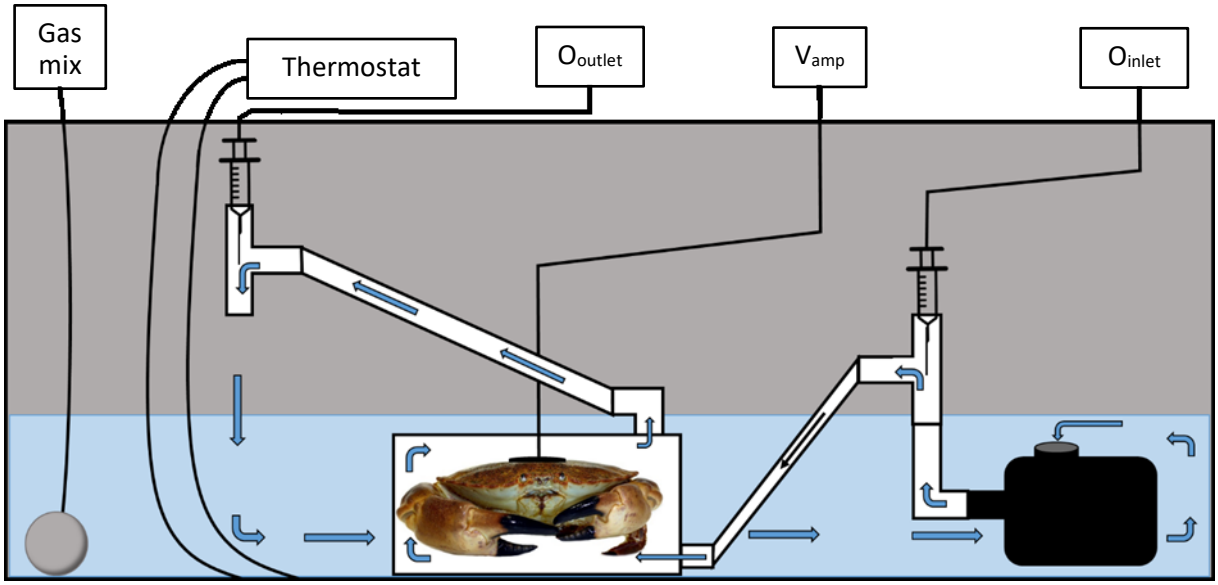

Fig. 9: Schematic experimental setup. The cuboid chamber containing the experimental animal is submerged in seawater. Temperature of the water was controlled by a thermostat. Water $P(O_2)$ and $P(CO_2)_w$ were set by respective gas mixes (see text) and supplied via an aeration stone. O_{inlet} indicates the microoptode measuring 100% oxygen saturation of the water, whereas O_{outlet} indicates the microoptode measuring the oxygen saturation of the seawater minus the oxygen consumption of the animal. V_{amp} indicates the voltage amplifier connected to the photo plethysmograph at the dorsal side of the animal. Blue arrows show the approximate flow of water within the system maintained by an aquarium pump.

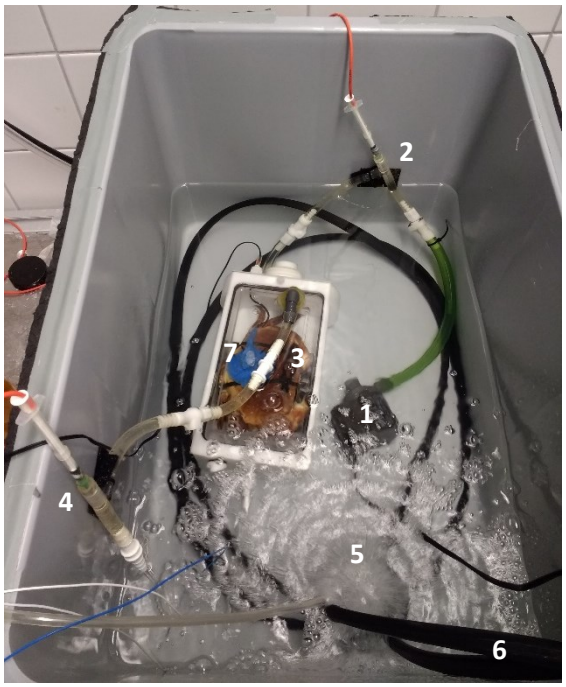

Fig. 10: Experimental setup. Order of numbers 1-4 represent the direction of water flow through the setup. At the pump (1), the water got sucked into the circulation and passed the inlet-optode (2). From there it entered the chamber containing the crab (3) with the attached photo plethysmograph fixed with dental wax (7, blue). From there, the water passed the outlet-optode (4) and exited the hose system. Set levels of water $P(O_2)$ and $P(CO_2)$ were maintained using an aeration stone (5). Water temperature was controlled by using thermic hoses connected to a thermostat (6).

2.2.3 Temperature ramp

In the habitat the experimental animals were caught from (sublittoral regions near Helgoland, 10-25 m), the annual average temperature reported for this region is 12°C (COSYNA 2018). For *C. pagurus* acclimated at 10°C, the upper pejus temperature indicating the uppermost temperature permanently tolerated is reported to be 16°C and the critical temperature to be 20°C (Metzger *et al.* 2007).

Based on these values the range of the temperature ramp was set to range from 12°C to 20°C to cover the thermal optimum as well as the upper passive thermal tolerance range of *C. pagurus.* It has been shown that acclimation has a significant effect on the thermal tolerance of *C. pagurus* (Cuculescu et al. 1998) and already occurs to certain extends after 4-6 h under the particular conditions (De Wachter and McMahon 1996). This had to be considered when investigating physiological responses in an ecological context.

Therefore, during one temperature step, the animals were allowed to acclimate for 5 h to the specific temperature before the 5 h measurement steps (**Fig. 11**, blue bars show acclimation time, red bars show measurement time). After placing the animal in the chamber, 14-19 h of acclimation time were set prior to first measurements at 12°C for the animal to recover from handling stress. Increase between the temperature steps was performed in 2°C steps over 2 hours, from 12 to 20°C. The end of the 20°C step was followed by a cool down to 12°C (**Fig. 11**). Temperature was controlled with a thermostat with deviations of ± 0.2°C (Lauda Eco RE 630; LAUDA DR. R. WOBSER, Germany). The total duration of the temperature ramp was approximately 80 h (**Fig. 11**). As mentioned above, the animals of the Main-group were subjected to two temperature ramps, one under normocapnic and one under hypercapnic conditions. To prevent training effects, the order of the treatments were randomized and animals were given at least one week to recover between the experiments.

In summary, the temperature ramp was designed to generate physiological responses of *C. pagurus* during its thermal optimum and passive thermal tolerance under climate change conditions with regard to temperature courses likely experienced in its natural habitat.

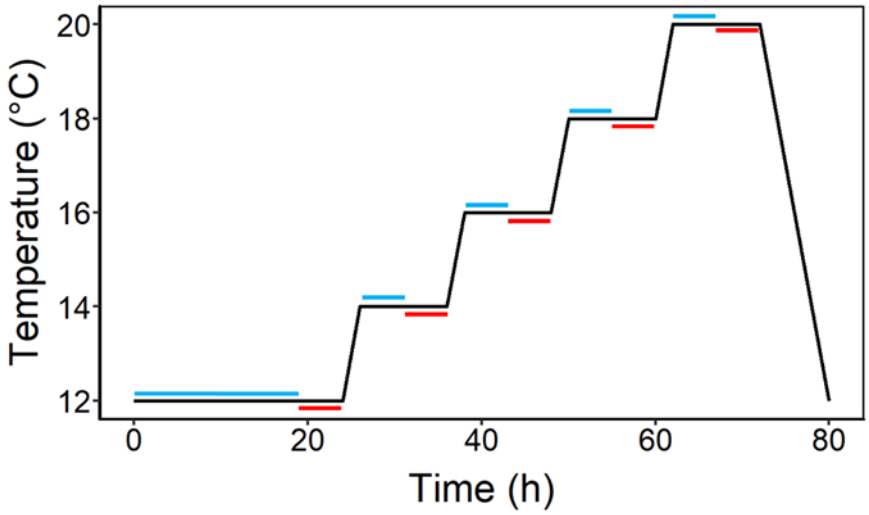

Fig. 11: Temperature ramp. The graph exemplifies the course of temperature changes over time. The animal was inserted into the setup at 0 h and 12°C. 12°C were maintained between 19-24 h to ensure acclimation of the animal within 9-14 h to the setup before conducting measurements. All other temperature steps were maintained for 10 h. Warming between the steps was performed with 2°C over 2 h. The animal was removed from the setup after 80 h. Blue bars indicate acclimation time to the apparent temperature, red bars indicate measurement time.

2.2.4 Monitoring of sea water carbonate parameters

To ensure defined conditions throughout the experiments, water temperature, salinity, $P(CO2)_w$ and pH_w (free scale) were determined prior to insertion of the animals into the experimental setup (Maus *et al.* 2018). Water temperature and salinity were measured using a conductivity meter (LF197; WTW, Weilheim, Germany). $P(CO2)_w$ determination followed from using a combination of a carbon dioxide probe (CARBOCAP GMP343; Vaisala, Helsinki, Finland) and carbon dioxide meter (CARBOCAP GM70, Vaisala) from the gas phase of the sea water. The pH meter (pH3310; WTW, Germany) was calibrated prior to the measurements using NIST buffers (pH 6.865; pH 9.180; itw Reagents, Darmstadt, Barcelona, Milano, Germany, Spain, Italy) at the apparent water temperature. The obtained values were then transferred to the free scale by using corrections for a reference buffer-pH in artificial sea water (Waters and Millero 2013) ionic strength and temperature, as recommended by Dickson (2010). The parameters and given values are summarized in **Tab. 6** in the appendix. Using these data, the water carbonate chemistry (including water bicarbonate concentrations, $[HCO_3^-]_w$) was calculated via the Microsoft Excel macro "CO2Sys" (v2.1; Pierrot and Wallace 2006). Values for K_1 and K_2 were taken from Millero (2010), KSO_4 from Dickson (1990) and $[B]_T$ from Uppström (1974). Before starting animal experiments, the water parameters were checked for stability between start (T = 12°C) and finish (T = 20°C) of the experimental temperature ramp. No significant differences were found in global carbonate parameters, specifically bicarbonate concentration (paired t-test: Normocapnia: p = 0.73, hypercapnia: p= 0.4) and dissolved inorganic carbon (paired t-test: Normocapnia: p = 0.36, hypercapnia: p = 0.35; Appendix: **Tab. 7**, **Tab. 8**). Confirmed by a stable water carbonate system across the temperature ramp, it was sufficient to only measure its set level before the insertion of the animal. A summary of the water carbonate system in the experimental setup prior to the start of the particular experiment is given in **Tab. 3**.

Tab. 3: Water parameters for different experimental conditions prior to start of experiments (n=3). Average values for the two treatments normocapnia and hypercapnia were calculated from three experiments within each group. Values are given for temperature (°C), salinity (PSU), pH (free scale), CO_2 partial pressure $P(CO_2)_w$ (µatm), bicarbonate concentration $[HCO_3^-]_w$ (µmol/kg sea water) and dissolved inorganic carbon (DIC) (µmol/kg sea water). Values are displayed in means ± standard deviation.

Treatment	Temperature (°C)	Salinity (PSU)	pH_w (free)	$P(CO_2)_w$ (µatm)	$[HCO_3^-]_w$ (µmol/kg SW)	DIC (µmol/kg SW)
Normo-capnia	11.6 ± 0.16	33.33 ± 0.17	8.07 ± 0.015	480 ± 16.33	2569.83 ± 142.82	2792.36 ± 173.74
Hyper-capnia	11.57 ± 0.52	33.7 ± 0.14	7.63 ± 0.02	1366.67 ± 13.12	2424.55 85.14	2544.97 90.25

2.2.5 Heart rate measurements

Heart rate of the animal was measured by using an infrared photo plethysmograph (IR-PPG, **Fig. 12**, **Fig. 13**; iSiTEC GmbH, Bremerhaven, Germany), attached dorsally to the carapace (**Fig. 14**). As this study emphasizes on non-invasive *in vivo* measurements, IR-PPGs were chosen over "more conventional" impedance electrodes.

This technique has been introduced for monitoring heart rates in crustaceans by Depledge (1984). The employed sensors and the amplifiers were constructed following the circuit proposed by Depledge (1984).

The IR-PPG consists of an infrared light emitting diode (LED) and a phototransistor detector, which are arranged parallel and face in the same direction (**Fig. 12**, **Fig. 13**).When active, the diode emits low intensity infrared light, which passes through the dorsal carapace into the pericardium. Since the ventricle changes its shape during systole and diastole, different amounts of light are reflected and recorded by the detector, returning high values for diastole and low values for systole (**Fig. 13**; Depledge 1984; Depledge and Andersen 1990). The obtained signal got pre-amplified by a 5 V preamplifier (iSiTEC, Bremerhaven, Germany) and digitized by an A/D transducer (Powerlab /8SP; AD Instruments, Sydney, Australia). The digitized signal was transferred to a computer (HP EliteBook 8470p; HP Inc, Palo Alto, CA, USA) and visualized using LabChart 7.3.8 Software at a sampling rate of 1000/s (AD Instruments, Australia).

Following the fixation of the animal, the IR-PPG was attached watertight to the cardiac region of the carapace, using dental wax (Surgident Periphery wax; Heraeus Kulzer Inc., Armonk, NY, USA) and "superglue" (**Fig. 14** ; Pattex Ultra Gel; Henkel AG & Co. KGaA, Düsseldorf, Germany). Then, the animal was placed in the experimental chamber, which was subsequently flooded with sea water and connected to the circulation for respirometry (see Section 2.2.6).

To drain the air from the gills of the animal, the chamber was gently turned in different directions. The experiment started by initializing the temperature ramp under the particular CO_2 level.

Heart rates were recorded over the entire course of the experiment using LabChart 7.3.8 software (AD Instruments, Australia). For analysis, only heartbeats during the last five hours of one temperature step were considered. The signal peaks were averaged over one minute intervals, giving values in beats per minute (bpm).

From the shape of the plethysmograph signal, further parameters characterizing cardiac performance were calculated, namely proxies for stroke volume and cardiac output.

The stroke volume proxy (SVP) is assumed to be described by the integral of the heartbeat signal as proposed by Giomi and Pörtner (2013). As additional proof is lacking, the suitability of this assumption shall be further assessed. Therefore, the integral signal will be stated as such. The cardiac output proxy (COP) can then be calculated as the product of heart rate and the integral. Both calculated parameters were normalized to the mean value at 12°C for each experimental run, to allow for analyses of relative changes.

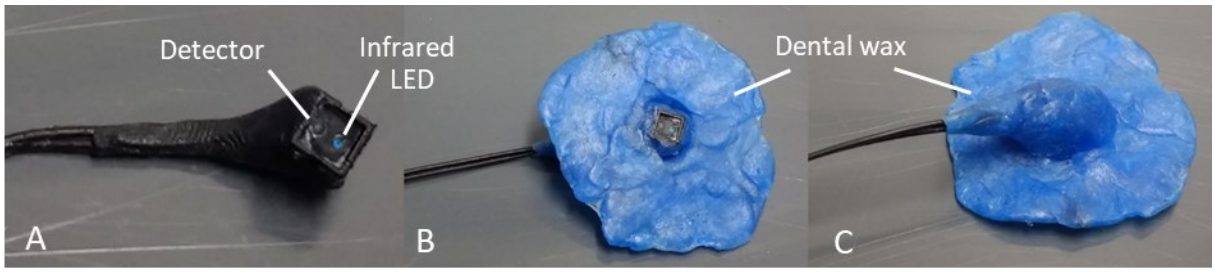

Fig. 12: Employed infrared photo plethysmographs. (A) Ventral view on the unmodified IR-PPG, revealing the location of the infrared light emitting diode and the phototransistor detector. (B) The IR-PPG in ventral position was modified for experimentation through covering with dental wax. (C) The modified IR-PPG is turned by 180° representing its positioning on the animal during experimentation.

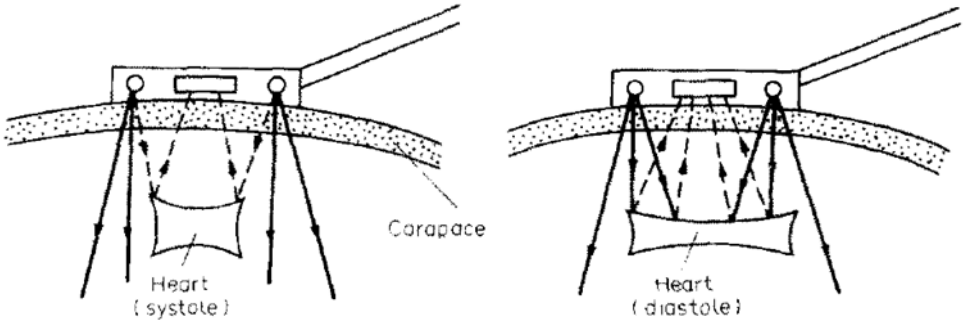

Fig. 13: Principle of infrared photo plethysmography. The heart reflects different amounts of emitted light depending on its shape. The shape differs with the stages of the heart cycle. Solid lines indicate emitted light, dashed lines indicate reflected light. Taken from Depledge (1984).

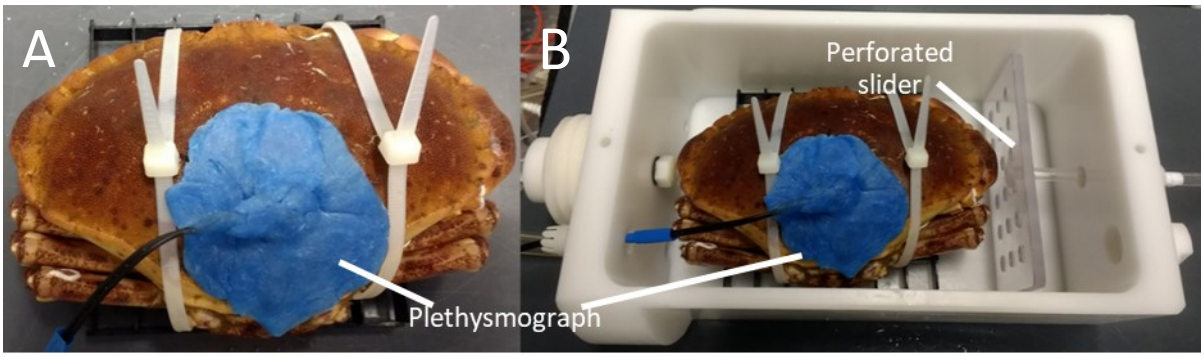

Fig. 14: Positioning of the plethysmograph. After fixation of the animal, the plethysmograph, covered with dental wax, was positioned over the cardiac area and was fixed and sealed using superglue (A). Finally, the animal was placed in the respiratory chamber, which was subsequently flooded with sea water (B).

2.2.6 Respirometry

Several methods for measuring oxygen consumption rates are currently available, quantifying the decline of oxygen due to aerobic metabolism in a known volume of water over time (for reviews see (Steffensen 1989; Svendsen *et al.* 2016).

In this setup, the oxygen consumption is calculated from the difference in gas content before and after the animal chamber and the rate of water flow (**Fig. 9**, **Fig. 10**; Ege and Krogh 1914).

Fiber-optic oxygen microoptodes, which determine the oxygen concentration by the amount of oxygen molecules colliding with a luminescent sensor tip (**Fig. 15**, NTH-Pst-L5-TF-NS40x0,80-PC3,1-YOP; PreSens Precision Sensing GmbH, Regensburg, Germany) were used for oxygen consumption measurements. More colliding molecules result in quenching of luminescence, causing declining emission signals and therefore represent changes in concentration (Kautsky 1939).

One optode each was placed before (inlet) and after (outlet) the respiratory chamber and were each connected to individual oxygen meters (Microx TX3; PreSens, Germany). The emission signals were measured continuously by recording one value per minute and visualized by the associated software (OxyView TX3-v6.02; PreSens, Germany) on a computer (HP EliteBook 8470p; HP Inc, USA).
Before every experiment, the optodes were calibrated. The 100% O_2-saturation calibration was done using the sea water equilibrated to the respective gas composition for the experiment prior to insertion of the animal. The 0% O_2-saturation calibration was done using streaming N_2-equilibrated water vapor flowing around the optodes. Adjustment of calibrations and measurements to changing temperatures throughout the course of the experiment were accounted for using a built-in temperature sensor and the atmospheric pressure at the beginning of the calibration. Furthermore, at 16°C a recalibration of the 100% oxygen saturation value was conducted to compensate for potential inaccuracies of the built-in temperature correction of the sensors.

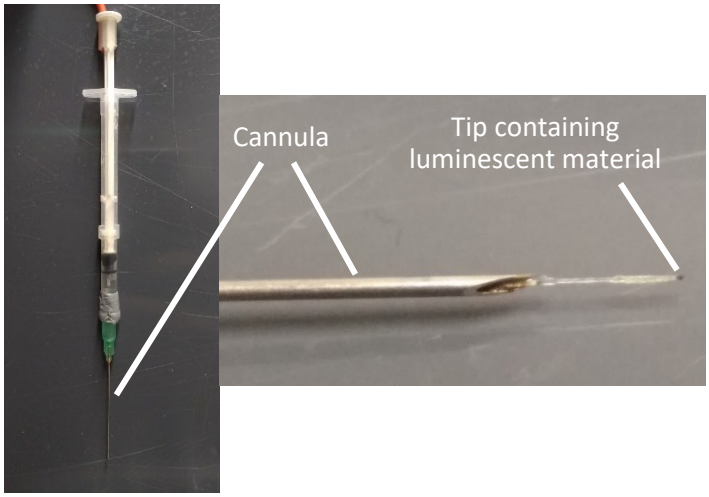

Fig. 15: Fiber-optic oxygen microoptodes. On the left, the complete optode is shown. The connection between the syringe and the cannula is sealed to prevent leakage. On the right, the luminescent tip is extended from the cannula, as it was used during the experiments.

To measure the oxygen consumption of the animal, the microoptodes were placed in the water stream before and after the chamber. These optodes had to be easily accessible and an undisturbed flow of water needed to be ensured to prevent headspaces at the optodes. The use of T-shaped connectors as the basis of specific optode-parts not only helped to prevent headspaces, it also protected the sensitive tips of the optodes. The design allowed for water to get pumped through the T-shaped inlet-optode-part, through the animal chamber, and out again to pass the T-shaped hold for the outlet optode (**Fig. 9**, **Fig. 10**).

Respiratory measurements were conducted over the whole course of the experiment, with sampling one value per minute.

To obtain the oxygen consumption in nmol O_2/min/g the values for oxygen consumption in percent of air saturation had to be converted into absolute concentration of oxygen at 100% saturation first. This was done using the formula:

$$c_{O_2}(100\%) = \alpha_{O_2} \cdot [(P_{air} - P_{wv}) \cdot 0.2095] \quad [3]$$

With $c_{O_2}(100\%)$ = absolute concentration of oxygen at 100% saturation in torr,

α_{O_2} = Bunsen solubility coefficient of oxygen in µmol/L/torr (from Boutilier et al. 1984),

P_{wv} = Vapor pressure of water in torr (from Dejours 1975),

P_{air} = air pressure in torr,

0.2095 = Volume percentage of oxygen in air.

These values were then multiplied with the difference between inlet- and outlet-optodes in percent oxygen saturation giving the difference in oxygen partial pressure $\Delta P(O_2)$ in torr:

$$\Delta P(O_2) = \frac{\text{difference}}{100} \cdot c_{O_2}(100\%) \quad [4]$$

Finally, the mass specific oxygen consumption is calculated by:

$$\dot{M}O_2 = \frac{\Delta PO_2 \cdot \alpha_{O_2} \cdot \dot{V}w}{w_f} \quad [5]$$

With $\dot{M}O_2$ = mass specific oxygen consumption rate in nmol/min/g,

$\Delta P(O_2)$ = difference in oxygen partial pressure $P(O_2)$ in torr,

α_{O_2} = Bunsen solubility coefficient of oxygen in µmol/L/torr (from Boutilier et al. 1984),

$\dot{V}w$ = water flow in L/min,

w_f = fresh weight of the crab in g.

To obtain correctly paired values of mass specific oxygen consumption rates time lags between the time of oxygen consumption within and the detection outside of the chamber in dependency to water flow velocity had to be considered. These lags occur, because the water between the site of consumption and detection functions as a reservoir (Steffensen 1989). Indeed, crustaceans show strongly correlated patterns of oxygen consumption and cardiac activity (Bradford and Taylor 1982; Burnett and Bridges 1981; Taylor 1982). Therefore, the detection points of the heart rate measurements, which showed no lag, due to their elicitation directly onto the carapace (**Fig. 14**) were used for correction since they indicated the exact time of activity. The corrected time for the lag under control conditions was maintained for all other temperature ramps.

2.2.7 Data analysis

Recording and analysis of heart rates were performed using LabChart 7.3.8 software (AD Instuments, Australia). To detect single heart beats, a computational fit within LabChart based on human finger pulse was used (**Fig. 16**). This basic fit was further customized (**Tab. 9**, see appendix) for every tested animal and checked manually for quality, confirming detection of all valid heart beat signals.

Oxygen consumption rates were simultaneously obtained with one value per minute. After the previously described time correction of the oxygen consumption rate signal, paired values of oxygen consumption- and heart rate for every time point of the measurement time were received. The time correction was performed using Microsoft Excel 2013 (Microsoft Corporation, Redmont, WA, USA).

All data points for each temperature step were checked for equal variance (Levene´s test) and normal distribution (Shapiro-Wilk test). Since normal distribution and equal variances were not constantly found across the datasets, differences between CO_2-treatments and temperatures within one animal were assessed by Wilcoxon signed-rank-tests for every combination. This resulted in 45 tests per parameter. To address multiple comparison problems, p-values were adjusted controlling the false discovery rate (Benjamini and Hochberg 1995). The confidence interval amounted to 95%. After applying the false discovery rate adjustments, this reduces the amount of false positives to 5% of significant results instead of 5% false positives of all tests (Benjamini and Hochberg 1995).

To detect underlying frequencies in the heart rate patterns, fast Fourier Transforms were conducted and visualizations were modified after Wearing (2010). Therefore, integrals of the spectral densities are displayed in variance of the time course and frequencies resulted in cycles per unit time.

All statistical analyses and graphs were conducted and created using RStudio (Version 1.1.453; R Development Core Team (2008), Vienna, Austria). Results are given in means ± standard deviation, if not stated otherwise.

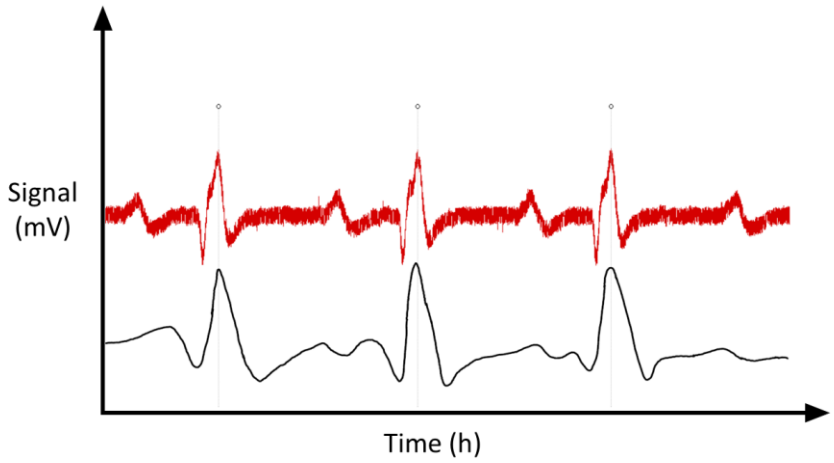

Fig. 16: Heart rate detection. Heart rate signals (red curve) were detected using a finger-pulse-based fit with individual customization (black curve). The detected peaks for heart rate measurements are marked with dots. Note, that preceding, smaller peaks are not recognized as full heart beats by the peak detection routine.

2.3 *In vivo* Magnetic Resonance Imaging (MRI)

2.3.1 Experimental setup

To study the motion of the ventricle of *C. pagurus* via *in vivo* MRI, animals were placed in a 9.4 T MR scanner with a 30 cm bore (BioSpec 94/30 US/R; Bruker BioSpin MRI GmbH, Ettlingen, Germany) equipped with a 127 kHz/cm gradient system (300 A; maximum slew rate = 1220 T/m/s; BGA20S; Bruker BioSpin MRI, Germany). One experimental animal was placed in a chamber with an approximate volume of 1 L, but analogous in design to the respirometry chamber. The position of the animal was checked using three perpendicular fast overview image scans (tripilot) in ParaVision 6.0.1 software (Bruker BioSpin MRI, Germany). To improve the signal-to-noise ratio in the cardiac region, a volume resonator with an inner diameter of 154 mm was used for resonance frequency (RF) excitation, coupled with a receive-only surface coil (40 mm diameter; Bruker BioSpin MRI, Germany). The coil was placed on the lid above the cardiac region of the animal (**Fig. 18**).

The animal was fixed under the chamber lid using hook and loop fasteners to prevent movement and ensure the position of the surface coil relative to the cardiac region. The chamber was constantly supplied with sea water equilibrated to normocapnic conditions concerning pH_w and $P(CO_2)_w$ (**Fig. 17**). Temperature was held constant at 12°C (**Fig. 17**).

Before starting the experiment, the animal was given at least one hour to recover from handling stress. Automatized protocols were used to adjust magnetic field homogeneity, basic frequency, and reference pulse power after insertion of the prepared experimental chamber into the magnet

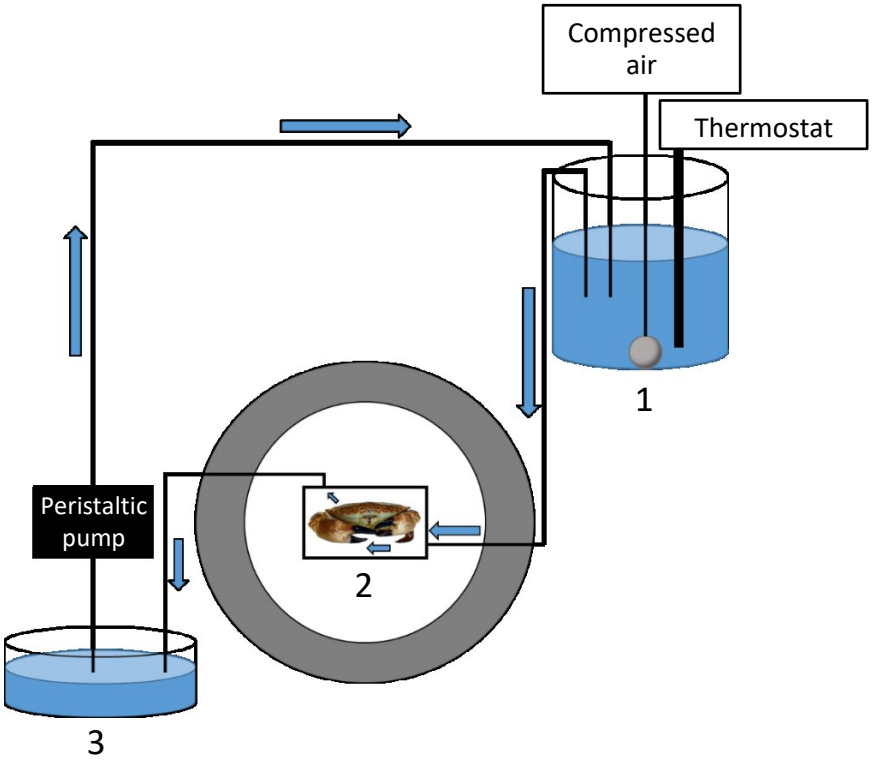

Fig. 17: Schematic design of the *in vivo* MRI setup. Water supply circulation started at the elevated placed water tank (1) where temperature is controlled via a thermostat (Lauda Eco RE 630; LAUDA DR. R. WOBSER GmbH & Co. KG, Germany) and normocapnic conditions were ensured using a membrane pump (Schego MK2K3 220-240V ~ 50 Hz 5W; SCHEGO Schemel & Goetz GmbH & Co KG, Germany) via an aeration stone. The water got transferred to the experimental chamber inside the magnet (2, grey) via hydrostatic pressure. After passing the chamber, the water flowed into an overflow basin (3) and got pumped back to the elevated water tank via a peristaltic pump (Masterflex I/P easy-load model 7529-10; Cole-Parmer Instrument Company, LLC., Vernon Hills, IL, USA). Blue arrows indicate the flow direction of the water.

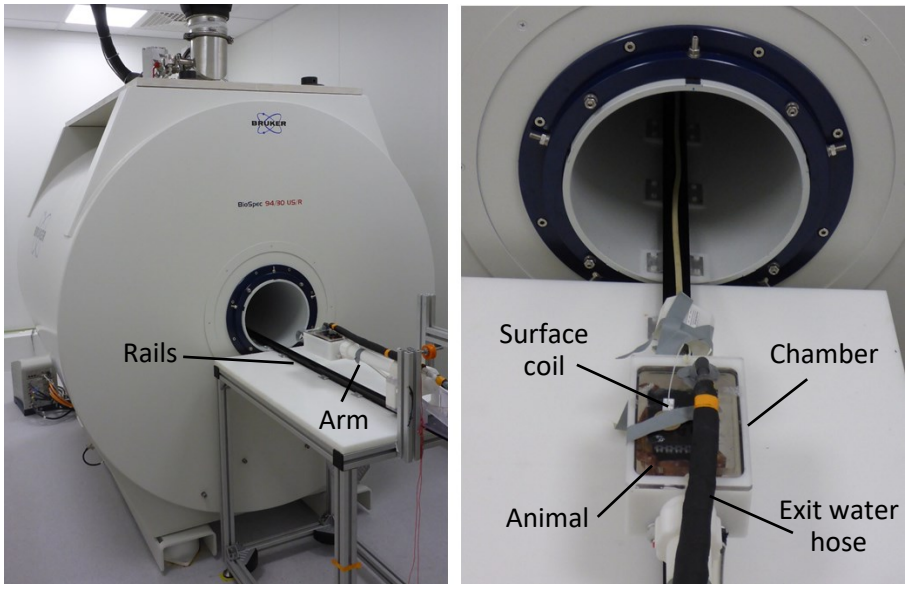

Fig. 18: Used MRI scanner. On the left, the complete scanner is shown. The experimental chamber is attached to an arm on rails which is used to position the chamber in the magnet. On the right, a close view on the experimental chamber including position of the surface coil is shown.

2.3.2 Determination of stroke volume using cine MRI

Stroke volume was determined from cardiac cine movies taken on Cancer 4 as an example. For orientation, coronal anatomical scans were created using T_1 weighted flow compensated fast low angle shot MRI (T_1-Fc FLASH MRI) to reveal the inner structure of the heart (**Fig. 19**). This method was used since it reduces the measurement time and provides sufficient tissue contrast.

To fully cover the heart, 20 individual scans with a slice thickness of 1 mm were conducted with no gaps between them (**Tab. 4**). The scans were visualized and parameters were adjusted in ParaVision 6.0.1 software (Bruker BioSpin MRI, Germany). The heart muscle, as well as the pericard were then reconstructed as a 3D model and their average volumes were determined using Amira 5.6.0 (Thermo Fisher Scientific Inc., Waltham, MA, USA).

To quantify the stroke volume, coronal *in vivo* cine MRI scans were conducted. This was done using the self-gated stationary cardiac imaging package IntraGate© (Bruker BioSpin MRI, Germany) in combination with FLASH MRI, to reconstruct a cardiac cycle as a movie using ten frames. Since these scans only represent the cardiac cycle at the specific position, scans were repeated to cover the total dorso-ventral extent of the heart.

This required 13 scans with a slice thickness of 1.2 mm without gaps between the slices or scans (**Tab. 4**). Using these movies, the systolic and diastolic frames were selected in each layer, resulting in two datasets, one representing the heart at systole and one representing the heart at diastole. These datasets were then reconstructed as 3D models using Amira 5.6.0 (Thermo Fisher Scientific Inc., USA). The changes in muscle volume were estimated by subtracting the diastolic volume from the systolic volume. For better visualization of the two states, an animation showing an artificial heartbeat through conviction of the models of systole into diastole was created. Therefore, pictures of the two states were morphed in Adobe After effects CS6 (Version 11.0.0.378; Adobe Systems Inc., San Jose, CA, USA), exported as a png-sequence and transferred into a movie in Adobe Premiere Pro CS6 (Version 6.6.0; Adobe Systems Inc., USA). 3D reconstructions were performed at the working group for Ecological Networks at TU Darmstadt.

Tab. 4: Parameters for visualization using MRI. The table shows the adjusted parameters for the anatomical scans and the IntraGate movies used for reconstruction.

Parameter	Anatomical	Movies
Method	T_1-Fc FLASH	IntraGate FLASH
Repetition time (ms)	306.5	7.647
Echo time (ms)	7.93	3.952
Number of averages/oversampling	5	100
Flip angle	80°	70°
Slice thickness (mm)	1	1.2
Slice gap (mm)	0	0
Field of view (mm)	99 x 100	100 x 100
Matrix size	256 x 256	256 x 256

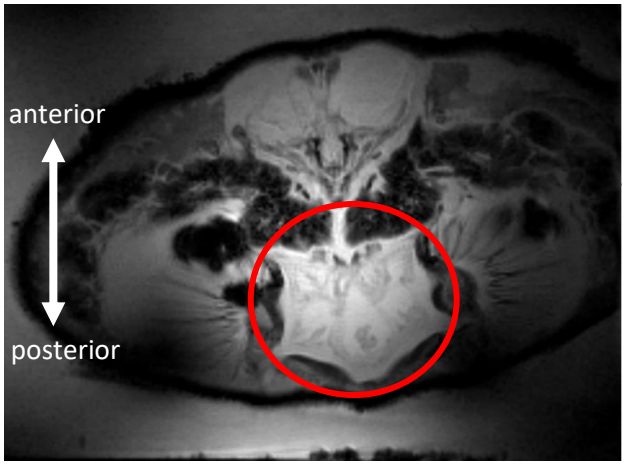

Fig. 19: Exemplary MRI scan using T_1-Fc FLASH. The scan shows a dorsal view onto the heart resulting from scans conducted in a coronal slice orientation. Red circle highlights the heart. The gills are visible laterally of the heart. The stomach can be seen with bright contrast anteriorly of the heart. Extending left and right of the animal between gill chambers and stomach is the hepatopancreas, the main digestive gland of crustacea.

3. Results

3.1 Oxygen consumption rates and cardiovascular performance

To investigate the effect of rising temperatures and $P(CO_2)_w$ levels on the cardiovascular performance of the edible crab, *C. pagurus,* two major performance parameters oxygen consumption rate and heart rate were simultaneously measured. After applying an operator mediated time correction for the oxygen consumption, data pairs of these parameters were obtained for every minute over the five hour measurement time. An exemplary time course after correction is shown in **Fig. 20** for Cancer 1 at 12°C under normocapnic conditions displaying the high temporal coupling of oxygen consumption rate and heart rate.

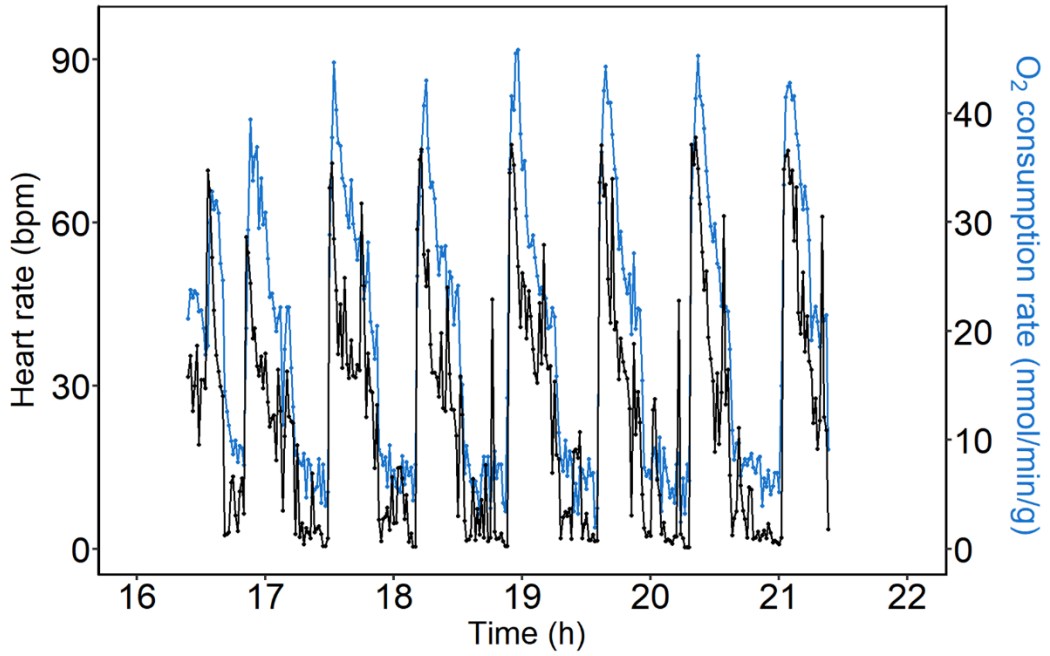

Fig. 20: Exemplary time course of cardiovascular parameters of Cancer 1 at 12°C under normocapnic conditions. Heart rate (black line) as well as oxygen consumption (blue line) change simultaneously in time and pattern. Rapid increases in both parameters are followed by steady declines. The pattern of both parameters fluctuates harmoniously over the measurement time. The left y-axis displays the heart rate in bpm. The right y-axis displays the oxygen consumption rate in nmol/min/g.

At 12°C, the heart rate fluctuated between 0-75 bpm representing a high amplitude of the occurring fluctuations. The oxygen consumption rates showed a high amplitude as well, ranging between 0-45 nmol/min/g. Changes, especially from low to high values appeared sudden within 2 minutes (**Fig. 20**).

The distinct peaks in heart rates and oxygen consumption rates are followed by a steady decline to minimum values, which seem to prevail over longer times than the maximum values. In summary, at 12°C heart rates and oxygen consumption rates in Cancer 1 show brief maxima but prolonged minima. These fluctuations in performance over time were also found for the integral of the heart rate signal, which was used as a proxy of the stroke volume and the approximated cardiac output (Giomi and Pörtner 2013). Bringing all these parameters together resulted in a broad coverage of the cardiovascular and metabolic performance of the edible crab at the apparent temperature (**Fig. 21**). These recordings were obtained for every crab under both conditions and all temperature steps (see appendix, **Fig. 39**-**Fig. 66**).

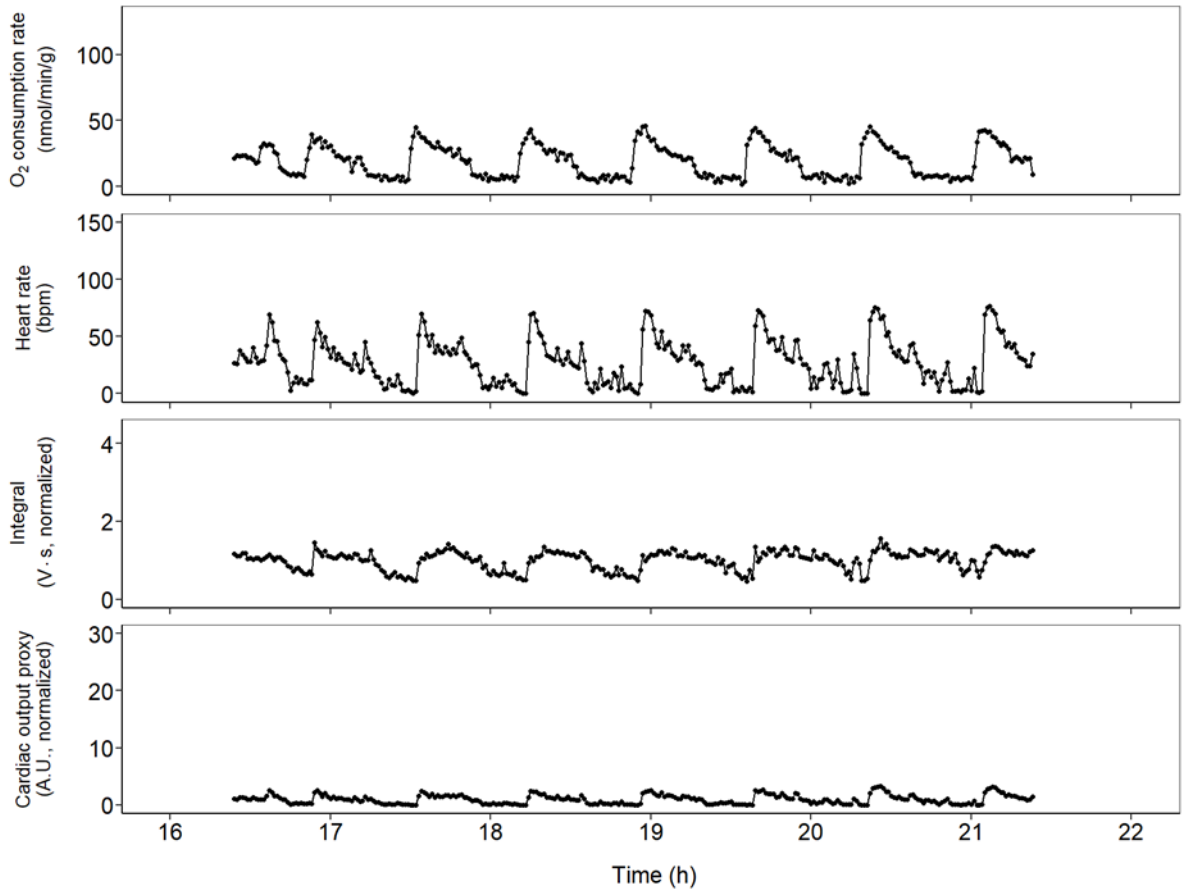

Fig. 21: Exemplary time courses of all obtained cardiovascular parameters of Cancer 1 at 12°C under normocapnic conditions. The y-axis indicates the displayed parameter in the particular graph. All graphs share the same x-axis. The integral (stroke volume proxy) is displayed in V·s and the cardiac output proxy is displayed in arbitrary units (A.U.) and are normalized to the mean of the signal at 12°C.

Over the course of the measurement time, all parameters show fluctuations between low values and high values. This pattern is conserved not only within one course, but was observed throughout all animals (see appendix, **Fig. 39**-**Fig. 66**). Time points of high values in oxygen consumption rates, coincide with local maxima in hearts rate, integrals and cardiac output proxies.

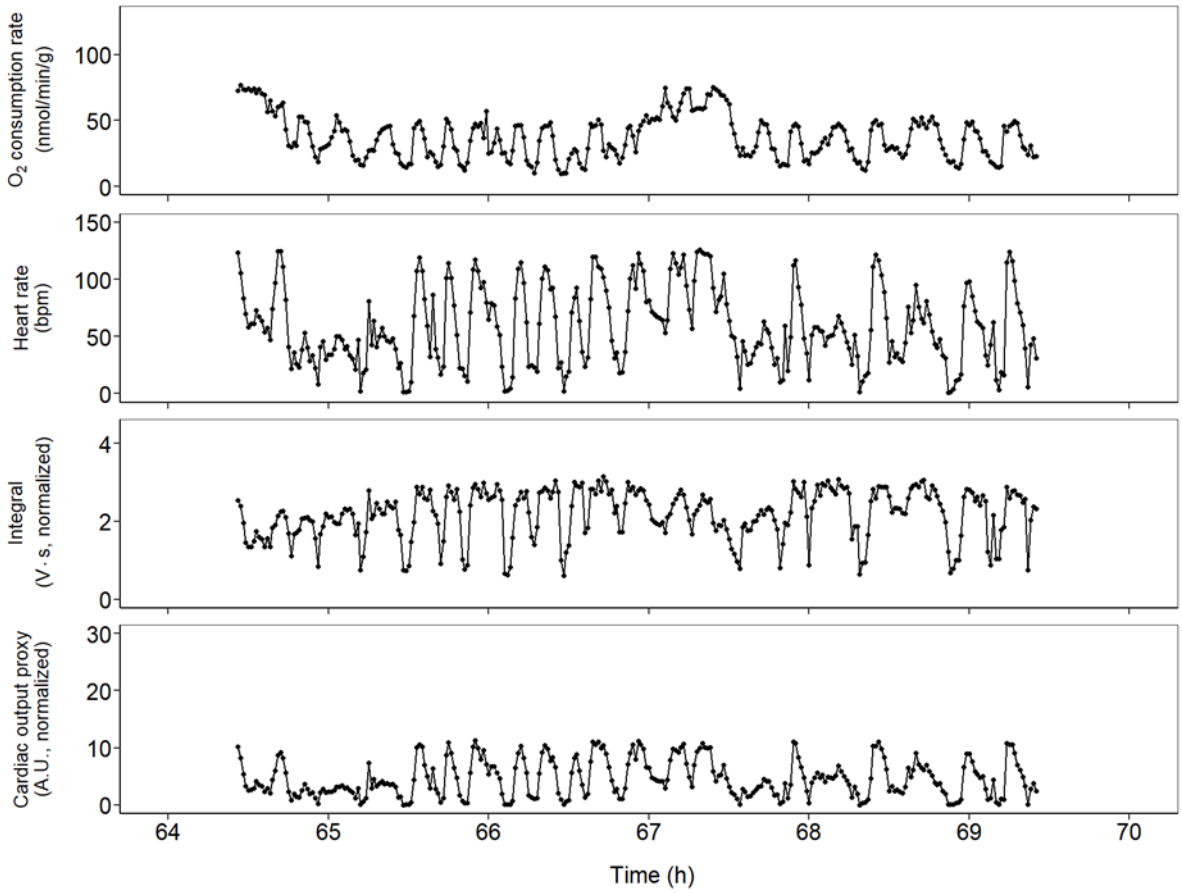

Fig. 22: Exemplary time courses of all obtained cardiovascular parameters of Cancer 1 at 20°C under normocapnic conditions. Thy y-axis indicates the displayed parameter in the particular graph. All graphs share the same x-axis. The integral (stroke volume proxy) is displayed in V·s and the cardiac output proxy is displayed in arbitrary units (A.U.) and are normalized to the mean of the signal at 12°C.

Increasing temperatures to 20°C, the animals still display fluctuating patterns (**Fig. 22**). In contrast to the measurements at 12°C however, the amplitudes (i.e. difference between minimum and maximum values) increased for all parameters. This becomes especially visible when looking at the values for the signal integral (representative of stroke volume) and the cardiac output proxy, where the values are three times and ten times higher than under control conditions, respectively.

At approximately 80 bpm however, the signal integrals reach plateau levels at three-fold increases, whereas as heart rate levels are still increasing towards ca. 130 bpm during the same time frame. The integral signals only decrease again, once heart rates drop below 80 bpm. This results in a cutoff-like shape of the integral signals exemplarily illustrated in **Fig. 23**. This could be observed across all animals.

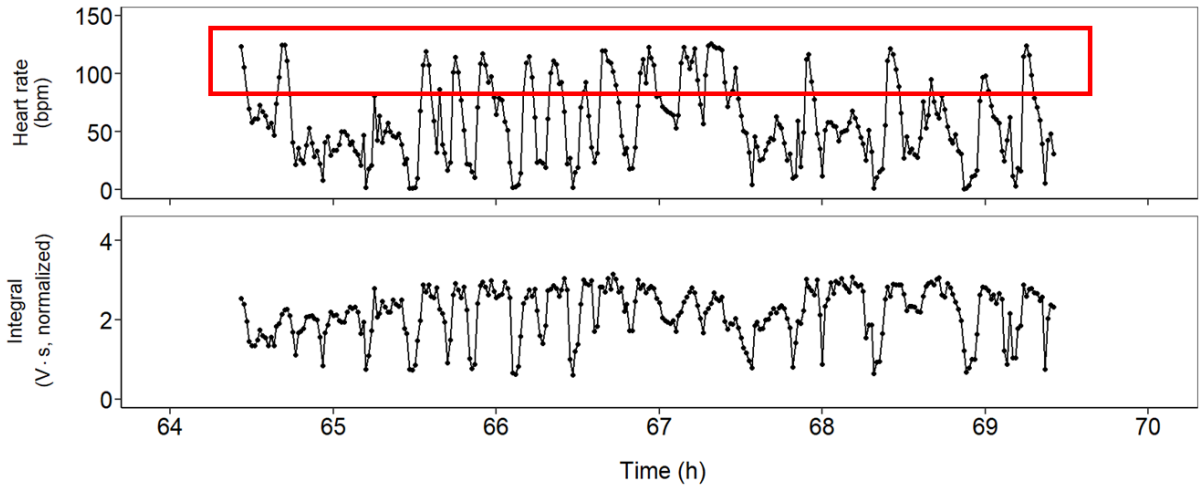

Fig. 23: Exemplary comparison of heart rates and integral signals of Cancer 1 at 20°C under normocapnic conditions. The red box indicates the heart rate values, which do not correlate with a rise in in integral levels. For these heart rates, steady values of integrals were detected, resulting in a cutoff-like shape of peaks in the integral time course.

To detect differences between normocapnic and hypercapnic conditions, comparisons between distributions of values in the time course were conducted (**Fig. 24**).The boxplots only contain phases of quiescent state, rhythmic performance patterns, as shown in **Fig. 21** and **Fig. 22**. Excluding phases of non-fluctuating, constantly high values results in at least 90 data points (i.e. 1.5 h of measurement) and a maximum of 300 data points (i.e. 5 h of measurement) per temperature step and condition for each animal (**Fig. 24**-**Fig. 27**, **B**-**D**). The boxplots containing values of all animals (**Fig. 24**-**Fig. 27**, **A**) therefore contain a maximum of 900 data points each.

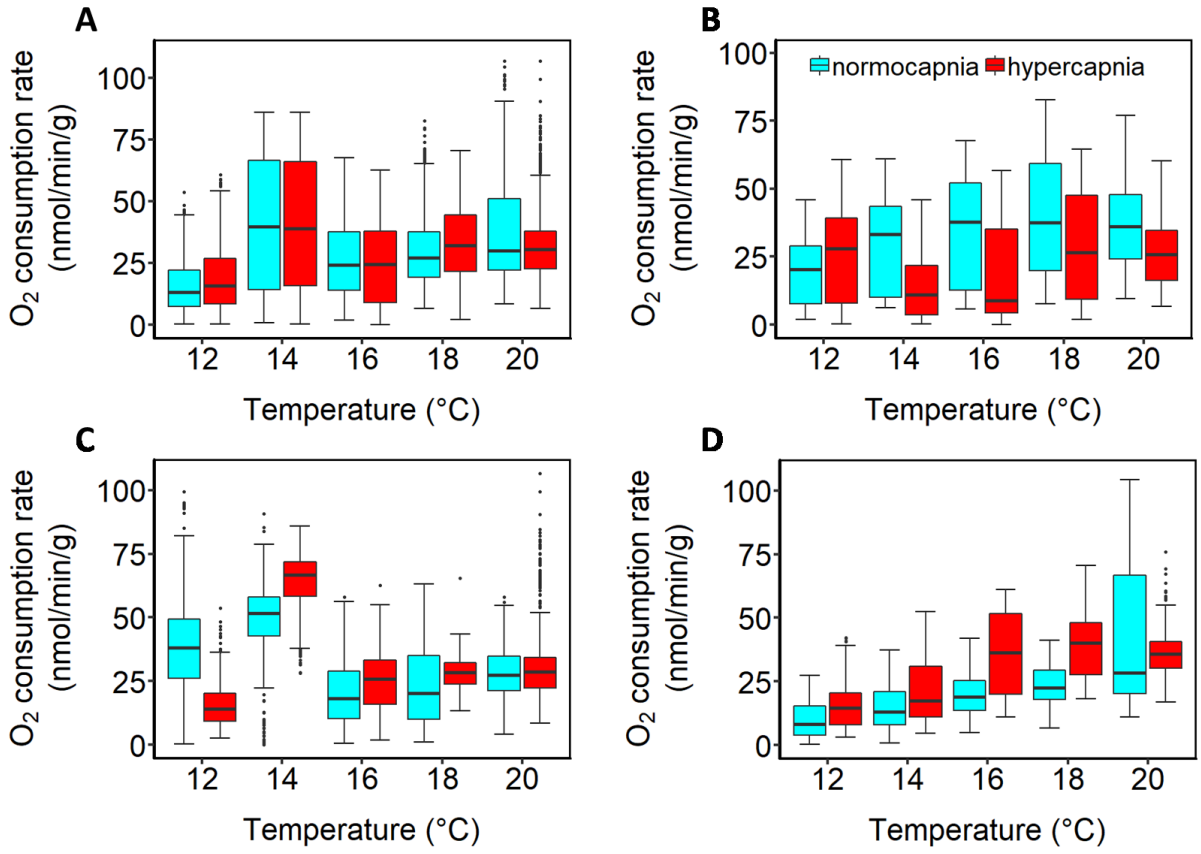

Fig. 24: Distribution of oxygen consumption rates for all investigated individuals. All graphs show the distributions for the oxygen consumption rates at every temperature step. (A) Oxygen consumption rates of all animals in nmol/min/g (n=3). (B) Oxygen consumption rates for Cancer 1 in nmol/min/g. (C) Oxygen consumption rates for Cancer 4 in nmol/min/g. (D) Oxygen consumption rates for Cancer 5 in nmol/min/g.

The boxplots in **Fig. 24**-**Fig. 27** describe the distributions of the temperature- and condition-dependent time courses of oxygen consumption rates and cardiovascular performance of all tested animals as exemplarily shown in **Fig. 21** and **Fig. 22**. Outliers were detected as points outside of 1.5 times the interquartile range.

For the majority of the datasets, non-normal distribution was found, as well as non-equal variances (see appendix, **Tab. 10**-**Tab. 15**).

As general results obtained for every animal and parameter, especially for those of cardiovascular performance, median level rises depended strongly on maximum level rises, whereas minimum levels remained stable (**Fig. 25**-**Fig. 27**, **A**). Additionally, heart rate and oxygen consumption rate signals reach performance maxima at 16°C-18°C, indicated by similar levels in medians of their distributions.

For combined oxygen consumption rates of all three animals, median levels rise with rising temperatures under both conditions (**Fig. 24 A**).

Especially at temperatures ranging from 16°C-20°C, oxygen consumption rate distributions do not differ between normocapnic and hypercapnic conditions at the specific temperature steps (see appendix, **Tab. 30**).

For oxygen consumption rates of Cancer 1, 12 out of 45 combinations show FDR-adjusted *p*-values being non-significant (since the majority of the results are significant, the non-significant are marked as bold in **Tab. 18**, see appendix). The levels of oxygen consumption rates under normocapnia are generally higher than under hypercapnia, especially when comparing higher (16°C-20°C) temperatures (**Fig. 24 B**). Thereby, the oxygen consumption rates rise with rising temperatures until 16°C, where they reach a plateau. The rise in consumption rate levels can be quantified by detecting differences when comparing high (16°C, 18°C, 20°C) to low temperatures (12°C-14°C). The reach of the plateau is described by same levels of medians between high temperatures under normocapnic conditions (16°C, 18°C, 20°C). Comparing within hypercapnic measurements and excluding 12°C, a similar rise could be observed. (**Fig. 24 B**; see appendix, **Tab. 18**).

When looking at the oxygen consumption rate boxplots of Cancer 4, distributions for 14°C under both conditions distinguish significantly from every other distribution (see appendix, **Tab. 22**). Generally for oxygen consumption rate measurements, similarities could be found when comparing temperatures of at least 16°C under both conditions to each other (**Fig. 24 C**). Similarities were also found when comparing control conditions (12°C normocapnia) to high temperatures under hypercapnia (see appendix, **Tab. 22**).

The oxygen consumption rates of Cancer 5 rise in maximum levels with increasing temperature. Furthermore, in contrast to the first two animals, the minimum rates clearly rise too, even though the slope appears not as steep as for the maximum levels (**Fig. 24 D**). Additionally, the width and position of the interquartile range under hypercapnic conditions seems to level off at 16°C, whereas this cannot be observed for interquartile ranges under normocapnic conditions (**Fig. 24 D**). This plateau can be further quantified by detecting similarities between the distributions of 16°C to 18°C and 20°C under hypercapnic conditions (**Fig. 24 D**; see appendix, **Tab. 26**).

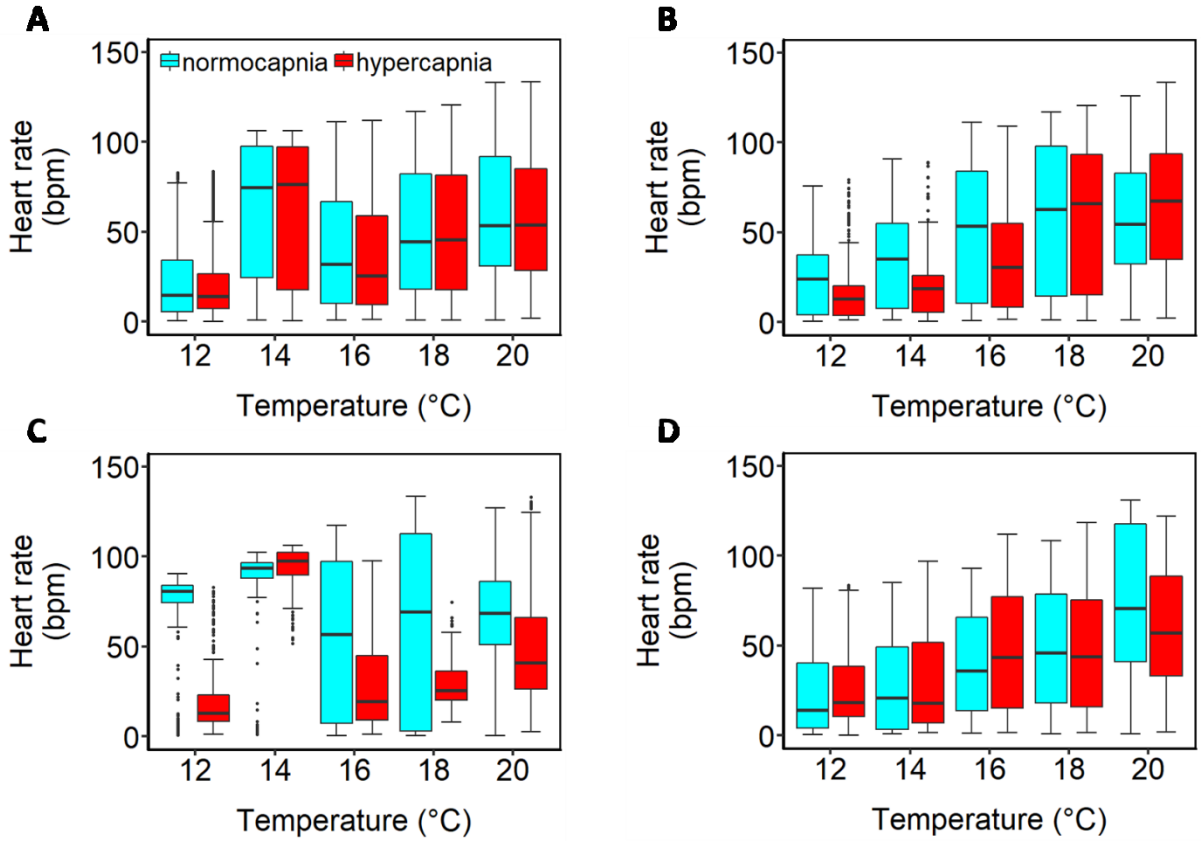

Fig. 25: Distribution of heart rates for all investigated individuals. All graphs show the distributions for the heart rates at every temperature step. (A) Heart rates of all animals in bpm (n=3). (B) Heart rates for Cancer 1 in bpm. (C) Heart rates for Cancer 4 in bpm. (D) Heart rates for Cancer 5 in bpm.

Generally, all three cardiac parameters (without oxygen consumption rates) show simultaneous rises in amplitudes towards higher temperatures under both conditions. There, the rise of amplitudes depend on a rise of maximum performance levels while maintaining constant minimum performance levels over all steps of the temperature ramp. Furthermore, the interquartile range, representing 50% of the values incorporated in the boxplot, shift upwards with rising temperatures. No distinct pattern in reaction to elevated CO_2 could be observed when comparing central tendencies of combined distributions (**Fig. 25**-**Fig. 27**, **A**).

Beside these general trends observed from the combined distributions of all animals, for heart rates of Cancer 1 under normocapnic conditions, the temperature-dependent rise continues until 16°C, where the heart rate levels reach a plateau analogous to the one found for the oxygen consumption rates.

The rise under normocapnic conditions until 16°C is quantified by detecting differences in distributions between 12°C, 14°C and 16°C (see appendix, **Tab. 19**). The plateau is described by similarities between temperatures from 16°C to 20°C (**Fig. 25 B**; see appendix **Tab. 19**).

Under hypercapnic conditions, a similar shift towards higher heart rates in maximum levels and interquartile range position under rising temperatures could be observed (**Fig. 25 B**). At 18°C, the heart rates reach a plateau. This could also be described statistically, since no similarities could be observed when comparing temperatures from 12°C-18°C to one another. The only similarities were found between 18°C and 20°C (**Fig. 25 B**; see appendix, **Tab. 19**).

When comparing the temperature courses of both conditions, the heart rates under normocapnic conditions reach the plateau phase at lower temperatures (16°C) than under hypercapnic conditions (18°). Additionally, the heart rate interquartile ranges and medians are found to be approximately half the size and height at temperatures from 12°C-16°C under hypercapnic conditions than under normocapnic conditions. This finding is supported by similarities detected between 12°C under normocapnic conditions and 14°C under hypercapnic conditions and 14°C under normocapnic conditions and 16°C under hypercapnic conditions (see appendix, **Tab. 19**). However, distributions under both conditions seem to approach to similar maximum levels, since no differences could be observed when comparing high temperatures (16°C-20°C) under normocapnic conditions to high temperatures (16°C-20°C) under hypercapnic conditions (**Fig. 25 B**; see appendix, **Tab. 19**). In summary, the heart rate levels under normocapnic conditions rise continuously with rising temperatures until they reach a performance plateau at 16°C. Under hypercapnic conditions, this rise in performance levels is offset towards higher temperatures, resulting in reaching the plateau at 18°C. However, the performance levels reached at the plateau are the same under both conditions.

For Cancer 4, individual trends in the heart rate measurements follow the same mechanism as observed in Cancer 1, with rising temperatures, the amplitude of the fluctuations increases due to rising maximum levels of heart rate. Minimum heart rate levels remain on the same level throughout the temperature ramps, except for 14°C under hypercapnic conditions. During this measurement time, the animal showed hardly any levels of fluctuations (**Fig. 25 C**; see appendix, **Fig. 53**). Additionally, the distribution obtained during this temperature step shows significant differences to all other distributions (see appendix, **Tab. 23**).

Furthermore, after 14°C, the interquartile ranges grow, except for 18°C hypercapnia, indicating more dispersion of the values in the mid 50% of the distributions (**Fig. 25 C**). This can also be seen when looking at the particular time courses (see appendix, **Fig. 49**-**Fig. 51**, **Fig. 54**-**Fig. 56**).

Under normocapnic conditions, no increase in performance levels from 16°C-20°C could be observed. As seen for the other two animals, the rise in amplitude of the heart rates of Cancer 5 depends on the rise of the maximum levels. The interquartile ranges increase slightly with rising temperatures under both conditions and migrate towards higher heart rates (**Fig. 25 D**).

When only comparing normocapnic conditions, a steady rise of the course over the temperatures could be observed (**Fig. 25 D**, see appendix, **Tab. 27**). Under hypercapnic conditions, there is also a rise in heart rate levels observable. At 16°C, heart rate levels under both conditions align and this alignment also maintains for 18°C and 20°C (**Fig. 25 D**; see appendix, **Tab. 27**).

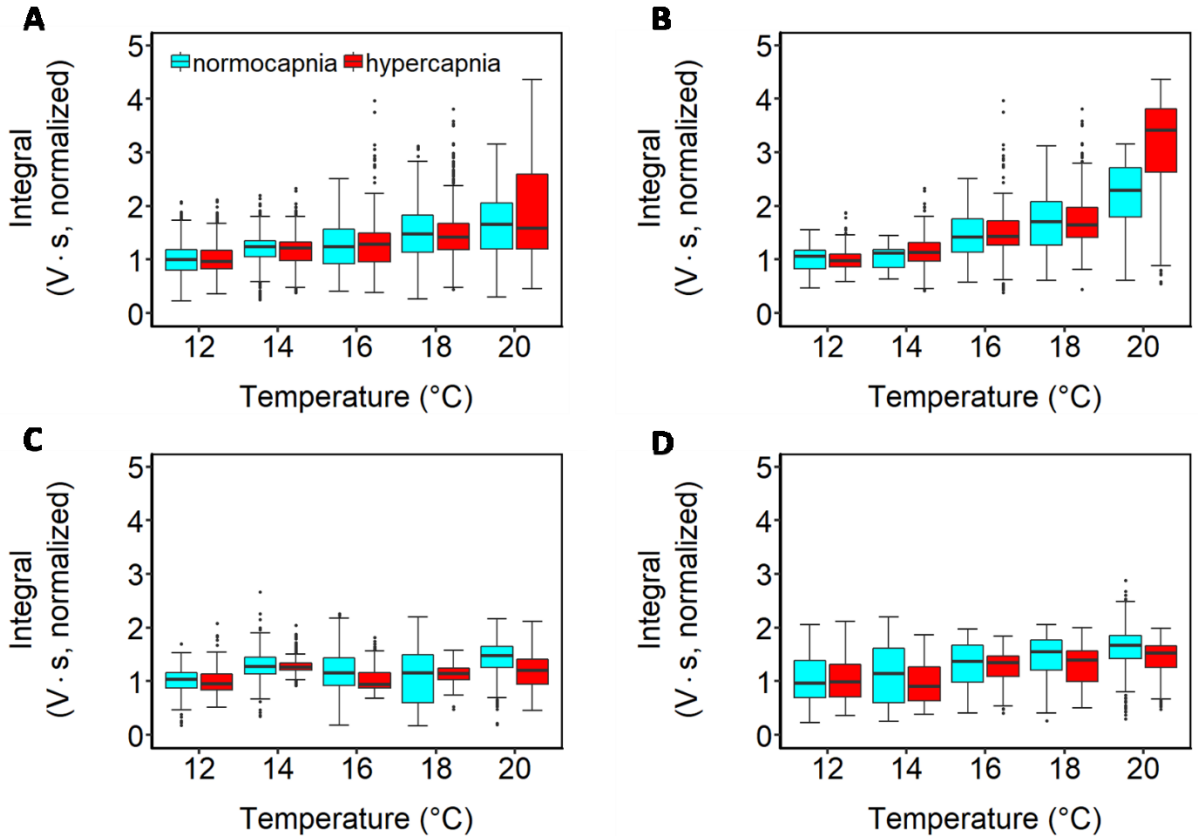

Fig. 26: Distribution of signal integrals for all investigated individuals. All graphs show the distributions for the signal integrals at every temperature step. Signals are normalized to 12°C normocapnia means. (A) Signal integrals of all animals in V·s (n=3). (B) Signal integrals for Cancer 1 in V·s. (C) Signal integrals for Cancer 4 in V·s. (D) Signal integrals for Cancer 5 in V·s.

The signal integral of Cancer 1 rises towards higher maximum levels and higher positions of the interquartile range with rising temperatures. Minimum levels remain stable over all temperatures. Furthermore, no plateau phases as present in oxygen consumption rates and heart rates could be observed (**Fig. 26 B**; see appendix, **Tab. 20**). The signal integral rises simultaneously under both conditions from 12°C-18°C. At 20°C the distribution under hypercapnic conditions shift towards higher levels than under normocapnic conditions, as indicated by significant differences in comparison (**Fig. 26 B**; see appendix, **Tab. 20**).

The range of the signal integral of Cancer 4 extends evenly with rising temperatures. However, the central tendencies of the signal integrals remain stable over the course of the temperature ramp and different conditions, unlike the measurements obtained for Cancer 1 (**Fig. 26 C**). Similar distributions could be found across all temperatures and conditions (see appendix, **Tab. 24**).

The signal integral does not show an increase in maximum levels over 2.5 times the control mean (outliers excluded) and only a slight increase in minimum levels. However, the interquartile range shifts upwards towards 1.5 times the control mean with simultaneous narrowing of its range (**Fig. 26 D**). Thereby, the range stays on the same level for 12°C and 14°C and the upshift takes place at temperatures from 16°C-20°C (see appendix, **Tab. 28**).

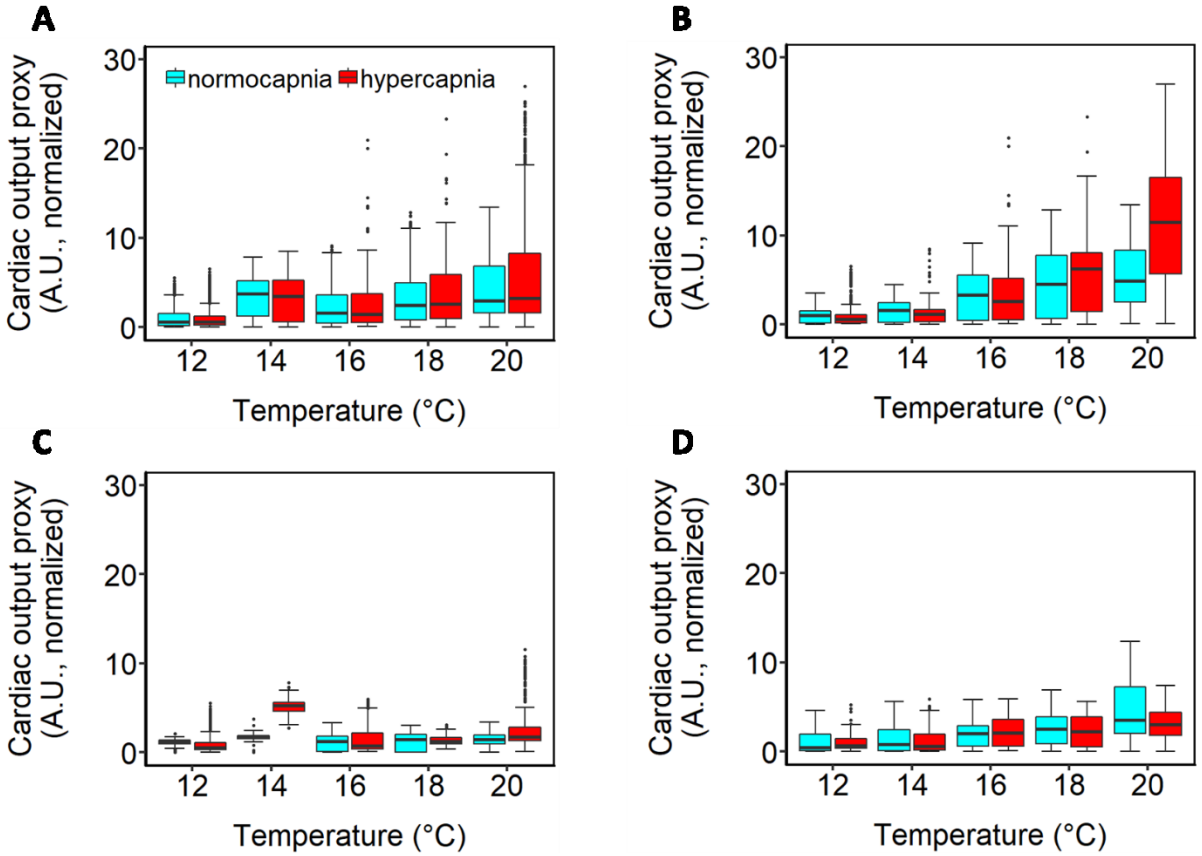

Fig. 27: Distribution of cardiac output proxy calculations for all investigated individuals. All graphs show the distributions for the calculations at every temperature step. Signals are normalized to 12°C normocapnia means. (A) Cardiac output proxy calculations of all animals in arbitrary units (n=3). (B) Cardiac output proxy calculations for Cancer 1 in arbitrary units. (C) Cardiac output proxy calculations for Cancer 4 in arbitrary units. (D) Cardiac output proxy calculations for Cancer 5 in arbitrary units.

Concerning the cardiac output proxy of Cancer 1 under normocapnic conditions, a rise in performance levels from 12°C-18°C could be observed, indicated by finding differences between these temperatures. However at 18°C, the cardiac output proxy reaches a plateau (**Fig. 27 B**; see appendix, **Tab. 21**). Under hypercapnic conditions, a steady rise in central tendencies of the cardiac output proxy over the whole temperature range could be observed (**Fig. 27 B**; see appendix, **Tab. 21**).

Nevertheless, cardiac output levels under both conditions rise simultaneously from 12°C-18°C, since no differences were found when comparing the conditions for one temperature step (**Fig. 27 C**; see appendix, **Tab. 21**).

Compared to the cardiac output obtained by Cancer 1, cardiac output levels of Cancer 4 are matched at 12°C and 14°C (**Fig. 27 B**, **C**). Whereas top levels in Cancer 1 rise between 16°C to 20°C up to levels five times higher than under control conditions, cardiac output in Cancer 4 stays on a comparable level (**Fig. 27 C**).

Therefore, the cardiac output proxy of Cancer 4 does not rise with rising temperatures under both conditions. As with the signal integral, similarities in distributions were found across comparisons between all temperatures and conditions (**Fig. 27 C**; see appendix, **Tab. 25**).

Concerning Cancer 5, the interquartile ranges shift slightly upwards, and increase their range (**Fig. 27 D**), even though the signal in general does not reach values as observed in Cancer 1 (for comparison, see **Fig. 27 B**). Analogous to the signal integral, the cardiac output proxy distributions can be divided in two parts, describing an upwards shift in cardiac output levels with rising temperatures (see appendix, **Tab. 29**).

3.2 Pattern analysis of heart activity over time

3.2.1 Time spent on highest and lowest heart rates

Since measurements over time in heart rates showed fluctuating, rhythmic patterns, possible changes in the shape of fluctuations needed to be quantified. The changes in amplitude have been presented in the previous section. The amount of time spent in the uppermost and the lowest 25% of the total range of values of one performance parameter under one specific treatment can reveal performance-dependent shifts over temperatures and conditions which cannot be directly covered by boxplots. In the following, this method was exemplarily applied to heart rate data obtained for the three tested experimental animals. The uppermost 25% of the value range are stated as top 25%, whereas the lowest 25% of the value range are stated as the bottom 25%.

At low temperatures, all animals spent between 5 and 14-fold more time in the bottom 25% of the heart rate range when exhibiting rhythmic patterns than in the top 25% (**Fig. 28**). With rising temperatures, this amount of time in the bottom 25% declines, whereas the time spent in the top 25% of the heart rate range rises simultaneously. Thereby, the times spent in top and bottom ranges of the heart rate follow a general trend to approach an even ratio, even though the achievement of this ratio could not be observed for all animals.

Furthermore, this approach of exemplary pattern analysis reveals, that all animals across the temperature ramp under hypercapnic conditions spent either more or same amounts of time in the bottom 25% of the total range than under normocapnic conditions (**Fig. 28**).

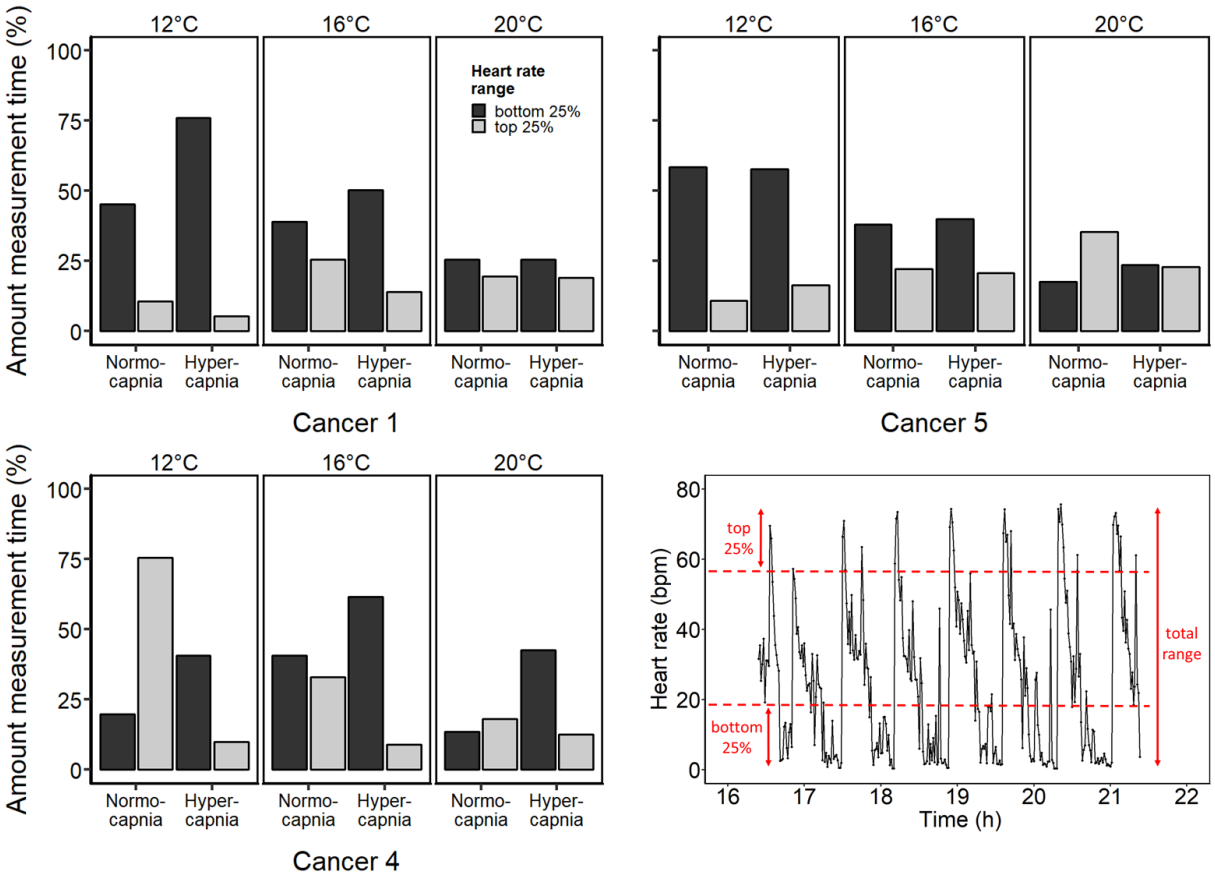

Fig. 28: Amounts of measurement time located in either the bottom 25% of the heart rate range, or the top 25% of the heart rate range for all three experimental animals. Exemplary time course of the heart rate in the bottom right corner (Cancer 1, 12°C, normocapnia) illustrates the chosen top and bottom ranges of the total range of the heart rate and the time points included in the barplots. For every animal, three temperature steps are shown, 12°C, 16°C and 20°C. Bars in dark grey represent bottom 25% of the heart rate range, light grey bars represent top 25% of the heart rate range. For every step, amounts of considered measurement times are displayed for both conditions (Normocapnia, Hypercapnia). Only rhythmic heart rate patterns were considered.

3.2.2 Exemplary fast Fourier Transforms of the heart rate

To detect underlying frequencies characterizing the rhythmic patterns of cardiovascular performance parameters, Fast Fourier Transforms (FFT) were conducted. These transforms are shown exemplarily for two temperatures (12°C and 20°C) of the heart rates of the experimental animals for both conditions. Since the integral under the spectral density plots equals the variance of the time series, higher integrals for specific frequencies display their increased contribution to the overall variance. All other transforms for every temperature step are given in the appendix (**Fig. 67**-**Fig. 84**).

As a general finding across all animals, the frequencies describing the heart rate signal shift from low frequencies between 0.5-4 cycles per hour towards higher frequencies ranging from 3-10 cycles per hour (**Fig. 29**-**Fig. 34**).

Furthermore, under hypercapnic conditions, the impact of single low frequencies found at 12°C under normocapnic conditions decreases (e.g. **Fig. 29**, **Fig. 30**).

Individual results for the experimental animals are described below.

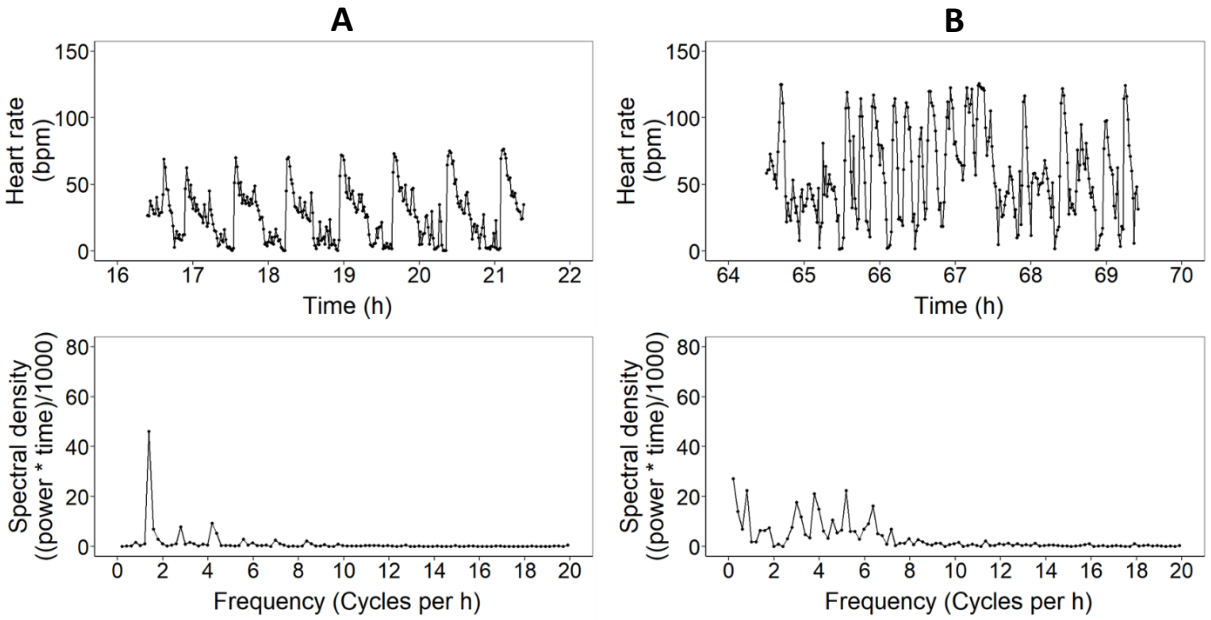

Fig. 29: Fast Fourier Transforms for the heart rates at 12°C (A) and 20°C (B) of Cancer 1 under normocapnic conditions. (A) Upper graph: Time series of the heart rate. Lower graph: Results of the FFT visualized as a spectral density plot of the underlying frequencies of the heart rate pattern. The x-axis displays the frequency in cycles per hour. The integral under the graph equals the variance of the time course in the upper graph. Higher peaks show more contribution to the variance. (B) Upper graph: Time series of the heart rate. Lower graph: Results of the FFT visualized as a spectral density plot of the underlying frequencies of the heart rate pattern.

For Cancer 1 at 12°C under normocapnic conditions, the fluctuating heart rate signal is shaped primarily by a frequency of 1.5 cycles per hour, indicated by representing the highest spectral density values with further contribution of frequencies of 2.5 and 4-4.5 cycles per hour (**Fig. 29**).

At 20°C, a shift towards higher frequencies could be observed. Whereas lower frequencies from 0.5 to 1 cycle per hour are still present, the majority of the heart rate pattern is made up of frequencies ranging from 3 to 7 cycles per hour. In contrast to 12°C, these frequencies contribute approximately equally to the variance of the time series.

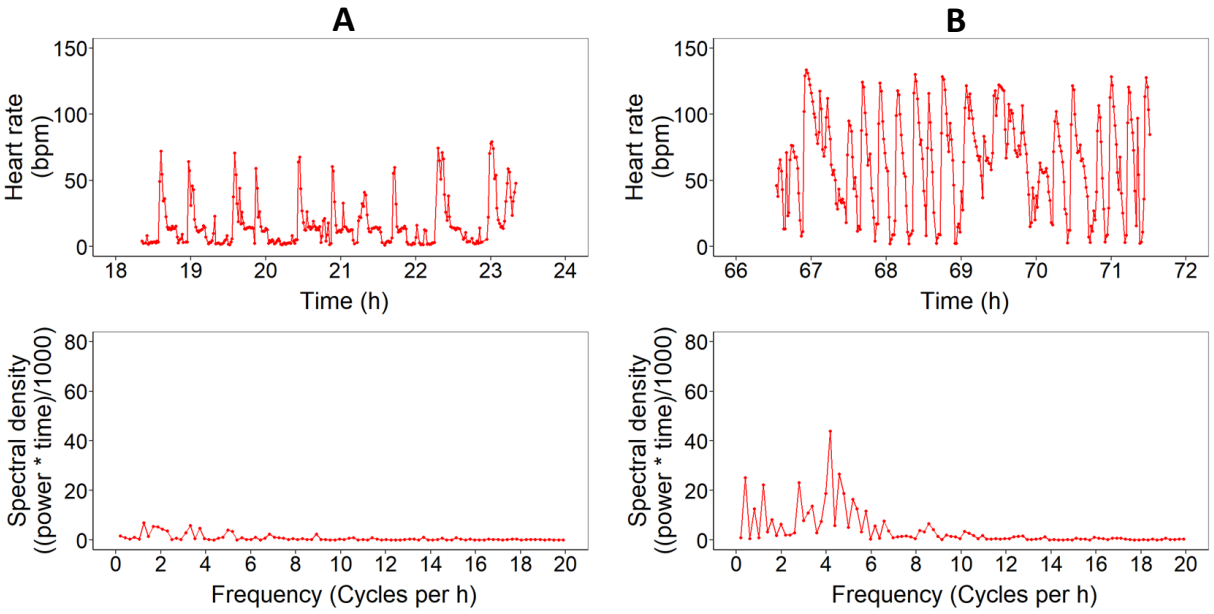

Fig. 30: Fast Fourier Transforms for the heart rates at 12°C (A) and 20°C (B) of Cancer 1 under hypercapnic conditions. (A) Upper graph: Time series of the heart rate. Lower graph: Results of the FFT visualized as a spectral density plot of the underlying frequencies of the heart rate pattern. The x-axis displays the frequency in cycles per hour. The integral under the graph equals the variance of the time course in the upper graph. Higher peaks show more contribution to the variance. (B) Upper graph: Time series of the heart rate. Lower graph: Results of the FFT visualized as a spectral density plot of the underlying frequencies of the heart rate pattern.

Under hypercapnic conditions at 12°C, the heart rate signal pattern cannot be described by one dominating frequency. Even though low frequencies from 1-2.5 cycles per hour are present, they are not as dominant as seen for 12°C under normocapnic conditions. Furthermore, they contribute equally to variance of the time series with higher frequencies between 3 and 5 cycles per hour (**Fig. 30**).

At 20°C, the importance of frequencies between 4 and 7 cycles per hour increases. The highest contribution to the variance of the time series is given by frequencies around 4-5 cycles per hour. Under hypercapnic conditions and high temperatures, the frequencies underlying the patterns are located in ranges between 3 and 7 cycles per hour with approximately even contribution to the variance of the time series (**Fig. 30**).

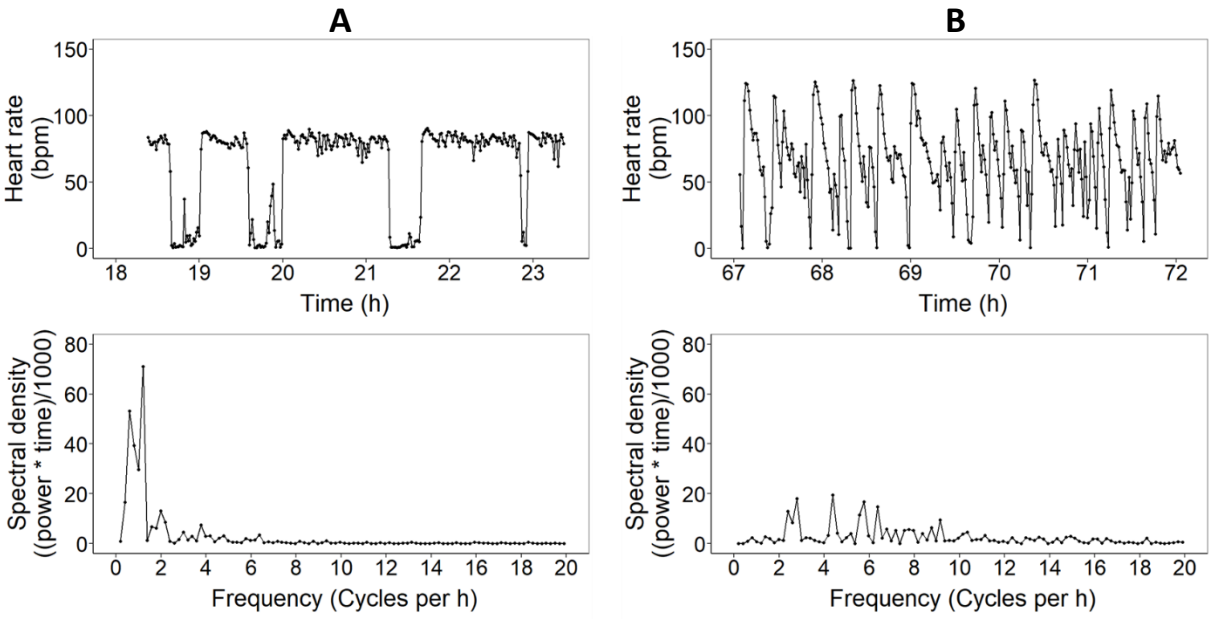

Fig. 31: Fast Fourier Transforms for the heart rates at 12°C (A) and 20°C (B) of Cancer 4 under normocapnic conditions. (A) Upper graph: Time series of the heart rate. Lower graph: Results of the FFT visualized as a spectral density plot of the underlying frequencies of the heart rate pattern. The x-axis displays the frequency in cycles per hour. The integral under the graph equals the variance of the time course in the upper graph. Higher peaks show more contribution to the variance. (B) Upper graph: Time series of the heart rate. Lower graph: Results of the FFT visualized as a spectral density plot of the underlying frequencies of the heart rate pattern.

For Cancer 4 at 12°C under normocapnic conditions, the heart rate pattern has a different shape than seen for Cancer 1. However, the predominant frequencies underlying this pattern are found between 0.5-2 cycles per hour. At 20°C, the pattern shaping frequencies shift upwards towards higher frequencies between 2-7 cycles per hour. Similar to Cancer 1, no predominating frequency was found, they all contribute approximately equal to the variance of the time course (**Fig. 31**).

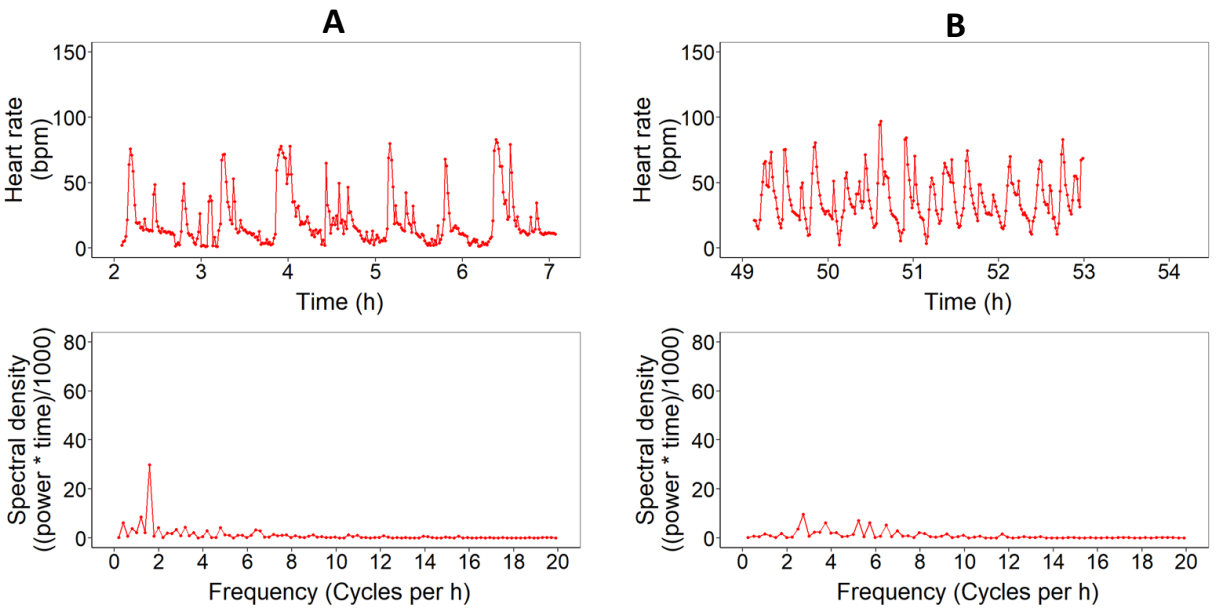

Fig. 32: Fast Fourier Transforms for the heart rates at 12°C (A) and 20°C (B) of Cancer 4 under hypercapnic conditions. Non-fluctuating patterns were excluded. (A) Upper graph: Time series of the heart rate. Lower graph: Results of the FFT visualized as a spectral density plot of the underlying frequencies of the heart rate pattern. The x-axis displays the frequency in cycles per hour. The integral under the graph equals the variance of the time course in the upper graph. Higher peaks show more contribution to the variance. (B) Upper graph: Time series of the heart rate. Lower graph: Results of the FFT visualized as a spectral density plot of the underlying frequencies of the heart rate pattern.

Under hypercapnic conditions at 12°C, the fluctuating pattern of the heart rate is predominately described by frequencies around 1.5 cycles per hour. At 20°C, the heart rate pattern shifts towards higher frequencies, indicated by shifts observed in the spectral density plot. There, the predominant frequencies are located between 3-7 cycles per hour, with their contribution to the variance spread evenly over this frequency range (**Fig. 32**).

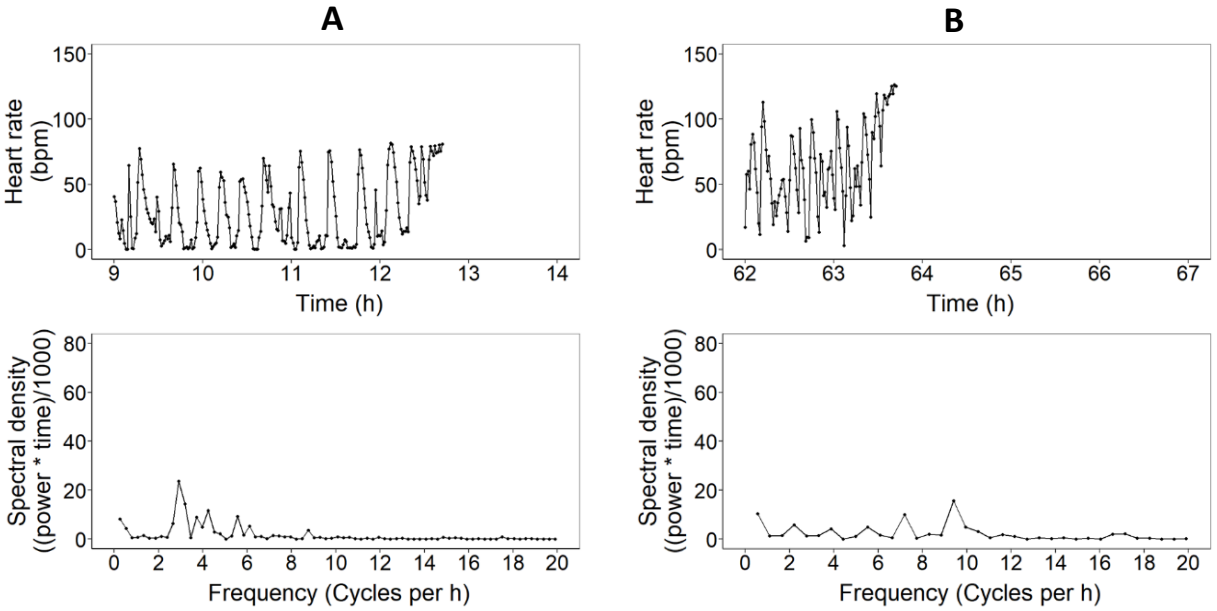

Fig. 33: Fast Fourier Transforms for the heart rates at 12°C (A) and 20°C (B) of Cancer 5 under normocapnic conditions. Non-fluctuating patterns were excluded. (A) Upper graph: Time series of the heart rate. Lower graph: Results of the FFT visualized as a spectral density plot of the underlying frequencies of the heart rate pattern. The x-axis displays the frequency in cycles per hour. The integral under the graph equals the variance of the time course in the upper graph. Higher peaks show more contribution to the variance. (B) Upper graph: Time series of the heart rate. Lower graph: Results of the FFT visualized as a spectral density plot of the underlying frequencies of the heart rate pattern.

For Cancer 5 under normocapnic conditions at 12°C the fluctuating heart rate pattern is predominantly shaped by a frequency of 3 cycles per hour. Frequencies around 4 and 6 cycles per hour contribute to overall shape of the pattern as well, even though their amount is about 50% smaller. At 20°C, the dominant frequencies shift upwards towards higher frequencies ranging from 4 to 10 cycles per hour. The two frequencies contributing most to the variance of the course are found at 7 and 9 cycles per hour (**Fig. 33**).

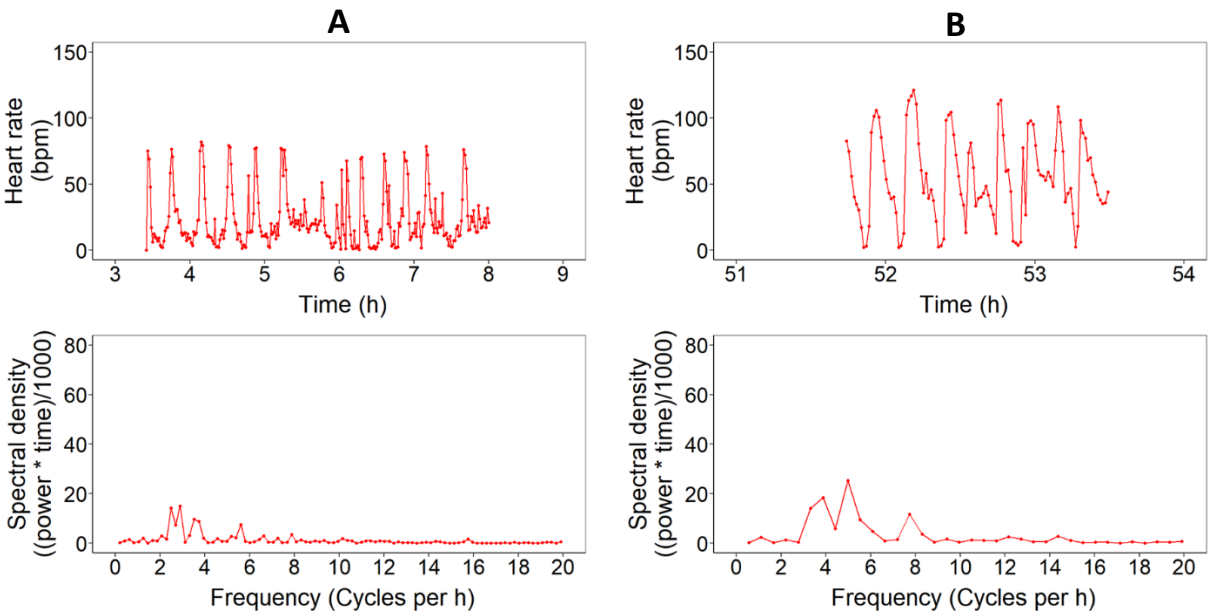

Fig. 34: Fast Fourier Transforms for the heart rates at 12°C (A) and 20°C (B) of Cancer 5 under hypercapnic conditions. (A) Upper graph: Time series of the heart rate. Lower graph: Results of the FFT visualized as a spectral density plot of the underlying frequencies of the heart rate pattern. The x-axis displays the frequency in cycles per hour. The integral under the graph equals the variance of the time course in the upper graph. Higher peaks show more contribution to the variance. Non-fluctuating patterns were excluded. (B) Upper graph: Time series of the heart rate. Lower graph: Results of the FFT visualized as a spectral density plot of the underlying frequencies of the heart rate pattern.

Under hypercapnic conditions at 12°C, the predominant frequencies shaping the heart rate pattern are found between 2 and 4 cycles per hour. At 20°C, the set of frequencies shifts upwards towards frequencies between 3 and 9 cycles per hour. Frequencies contributing the most are found at 4 and 5 cycles per hour (**Fig. 34**).

3.3 *In vivo* MRI

3.3.1 Anatomic reconstruction of the heart

To create the anatomic model of the heart for Cancer 4, 20 individual scans using T_1-Fc FLASH MRI were conducted. For reconstruction, only the tissue belonging to either the pericard or the ventricle were considered.

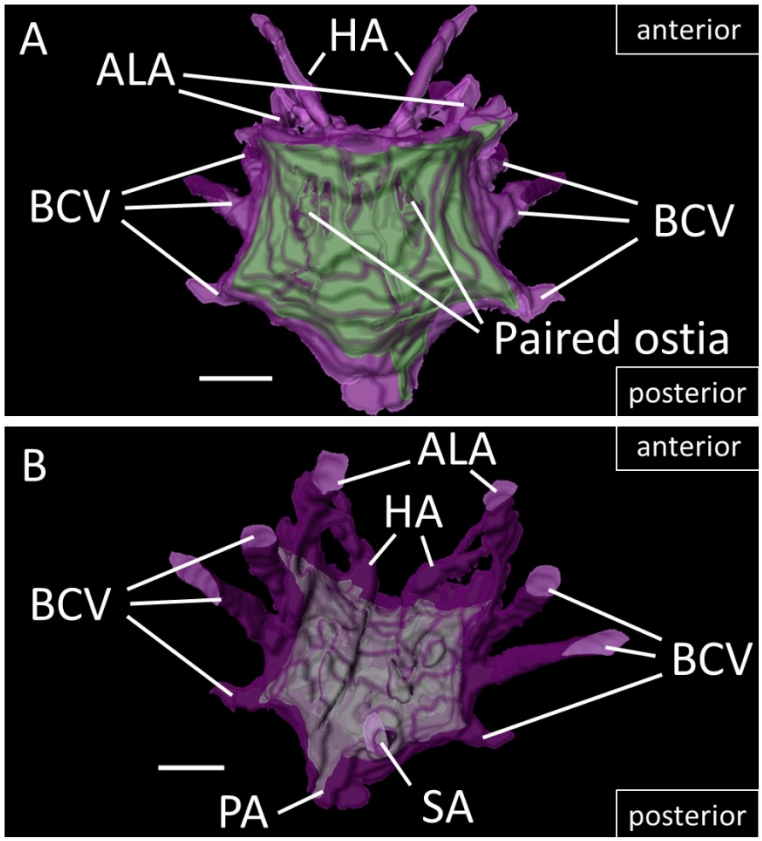

Fig. 35: Anatomical 3D reconstruction of the cardiac region of Cancer 4. Pericard and parts of adjacent venous arterial strucutres are shown in purple and transparent, ventricle is shown in green. (A) Dorsal view on the cardiac region including the pericard and the ventricle. (B) Ventral view on the cardiac region including the pericard and the ventricle. **ALA**, anterolateral arteries; **HA**, hepatic arteries; **BCV**, branchiocardiac veins; **PA**, posterior aorta; **SA**, sternal artery. Scale bars = 5 mm.

The cardiac region of *C. pagurus* lies slightly posterior to the middle of the body, directly under the carapace and above the pericardial alary muscles and the midgut region/gonads. The heart muscle (ventricle; green structure in **Fig. 35**) has a lateral diameter of 18 mm on average, an average height of approximately 7.5 mm and is suspended inside the pericardial sinus (pericard; purple structure in **Fig. 35**) by elastic alary ligaments (Maynard 1960). In a dorso-ventral view, both structures are approximately pentagonally shaped.

In total, five arterial systems comprising seven arteries arise from the heart supplying different regions of the body (McGaw and Reiber 2002). From the anatomical reconstruction, the following of these arteries could be described.

The anterolateral arteries (ALA, **Fig. 35**) originate dorsally at the anterior edge of the pericard with an angle of around 40° relative to the anterior aorta and supply the stomach, parts of the gonads, mandibles and antenna (McGaw and Reiber 2002). The hepatic arteries (HA, **Fig. 35**) also originate anteriorly of the heart, but with a smaller angle (approximately 10°) than the anterolateral arteries.

The branchiocardiac veins (BCV, **Fig. 35**) collect oxygenated blood from the branchial veins and transport it from their ventral origin to the dorsal heart (McGaw and Reiber 2002). The sternal artery (SA, **Fig. 35**) exits the heart ventrally and is the largest artery in the circulatory system. It passes the midgut, turns anteriorly and then again ventrally to supply the leg muscles (McGaw and Reiber 2002).

The posterior aorta (PA, **Fig. 35**) has a small diameter diameter and exits the heart posteriorly. After exit, it divides into two arteries dipping ventrally. These supply hemolymph to the posterior edge of the gonads, the midguts and possibly promotor muscles of pereiopods (McGaw and Reiber 2002).

The ventricle is the contractile organ of the heart. At diastole, the ventricle expands passively through the tension of the ligaments and hemolymph fills it through three paired ostia, placed dorsally, laterally and ventrally (**Fig. 36**; Maynard 1960). The hemolymph filling the heart congregates in cavities seen in reconstructions of the ventricle and MRI scans (**Fig. 36**).

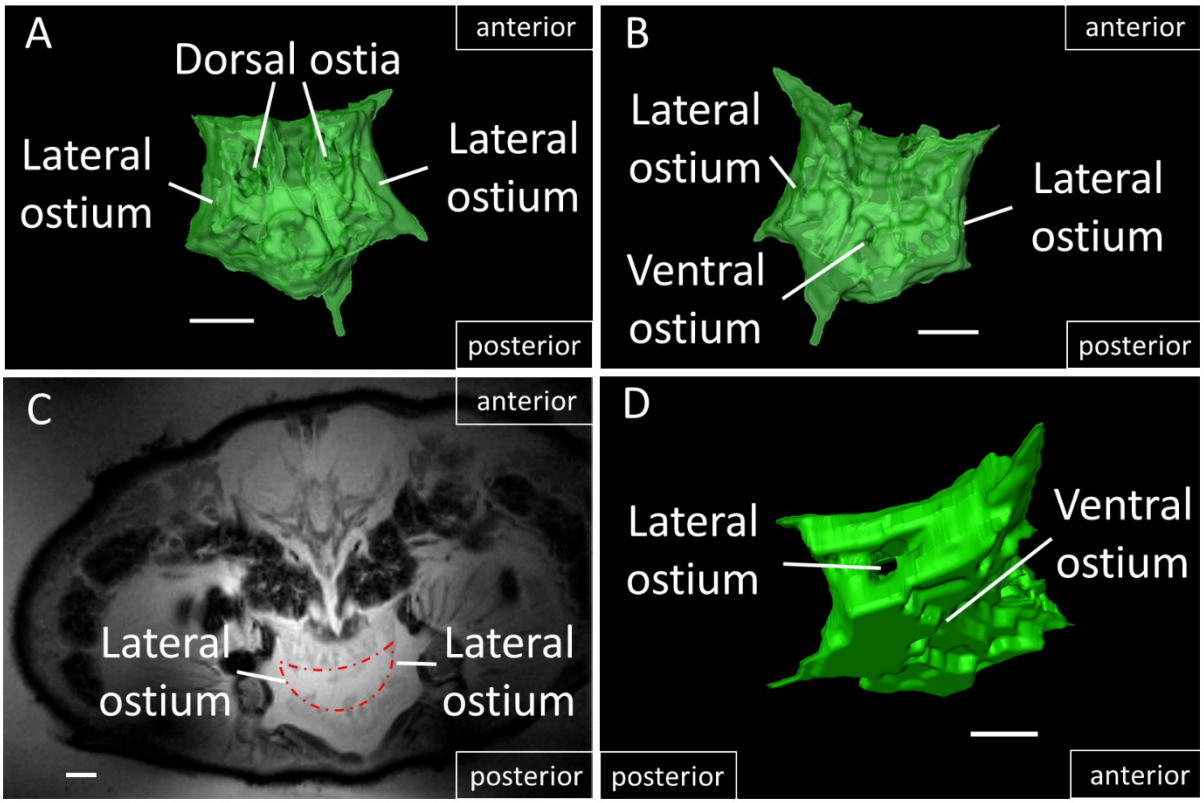

Fig. 36: Structure of the ventricle. (A) Dorsal view on the ventricle. Transparence reveals the inner structure with cavities starting from the lateral ostia. (B) Ventral view on the ventricle. Transparence reveals the inner structure with cavities starting from the lateral and ventral ostia. (C) T_1-Fc FLASH MRI scan showing the inner structure of the ventricle and revealing the cavities seen in A and B (inside red dashed line). (D) Lateral view on the ventricle. Scale bars = 5 mm.

3.3.2 Determination of stroke volume using cine MRI

Two 3D reconstructions of the heart of Cancer 4 were created, one in the systolic and one in the diastolic state. Therefore 13 IntraGate FLASH scans in coronal orientation were created to fully cover the heart. To determine the stroke volume, differences in muscle volume and cavity volume were calculated.

At systole, the middle of the ventricle contracts laterally (**Fig. 37**). In the posterior region, the contraction proceeds in anterolateral direction while maintaining those positions attached to the elastic ligaments. The anterior region contracts in posterior direction, however, this contraction is less intense than in the posterior region. Combining of these simultaneous contractile patterns creates a pumping mechanism supplying the arterial systems for systemic circulation (**Fig. 37**, **Fig. 38**).

At diastole, and thus relaxation, the heart fills with hemolymph. Relaxation in the lateral region proceeds laterally to the outside, contrary to the contraction direction at systole.

At the posterior end, relaxation proceeds posterolaterally from the contracted state and at the anterior end in anterior direction (**Fig. 37**, **Fig. 38**).

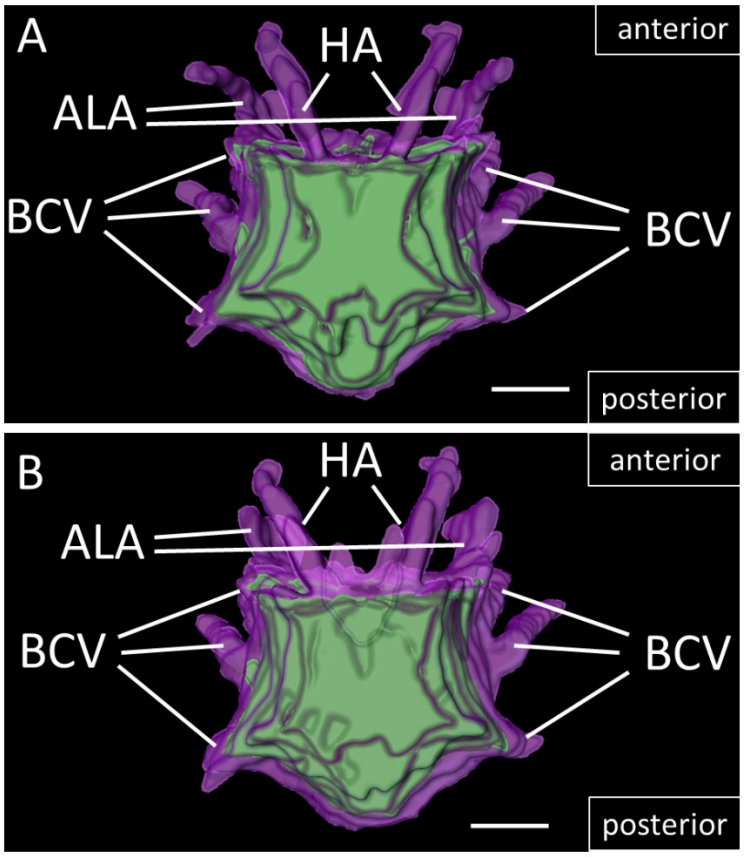

Fig. 37: 3D reconstruction of the cardiac region at systole (A) and diastole (B). The ventricle is shown in green, the pericard in purple. (A) At systole, contraction proceeds laterally in the lateral region, anterolaterally from the posterior end and posterior from the anterior end. (B) At diastole, relaxation proceeds laterally to the outside in the lateral region, posterolaterally towards the posterior end and anterior towards the anterior end. **ALA**, anterolateral arteries; **HA**, hepatic arteries; **BCV**, branchiocardiac veins. Scale bars = 5 mm.

Between the two states of the heart cycle, not only the outer shape of the ventricle changes, the inner structure changes as well. At diastole, the ostia open and the inner cavities of the ventricle fill with hemolymph (**Fig. 38**). During this state, the ventricle reveals atrium-like cavities with connections to the primarily observed ostia (**Fig. 35**, **Fig. 36**) and proximity to arterial systems being supplied with hemolymph (**Fig. 37**, **Fig. 38**).

At systole, during contraction, these cavities shrink, especially in the areas near to the ostia (**Fig. 38**). The ventricle reduces its muscle volume between systole and diastole by around 115 mm^3. Nearly the same values around 100 mm^3 were obtained when only considering the changes in cavity volume between the two states. Therefore, a volume around 0.1 mL will be considered as the determined stroke volume of Cancer 4 using MRI.

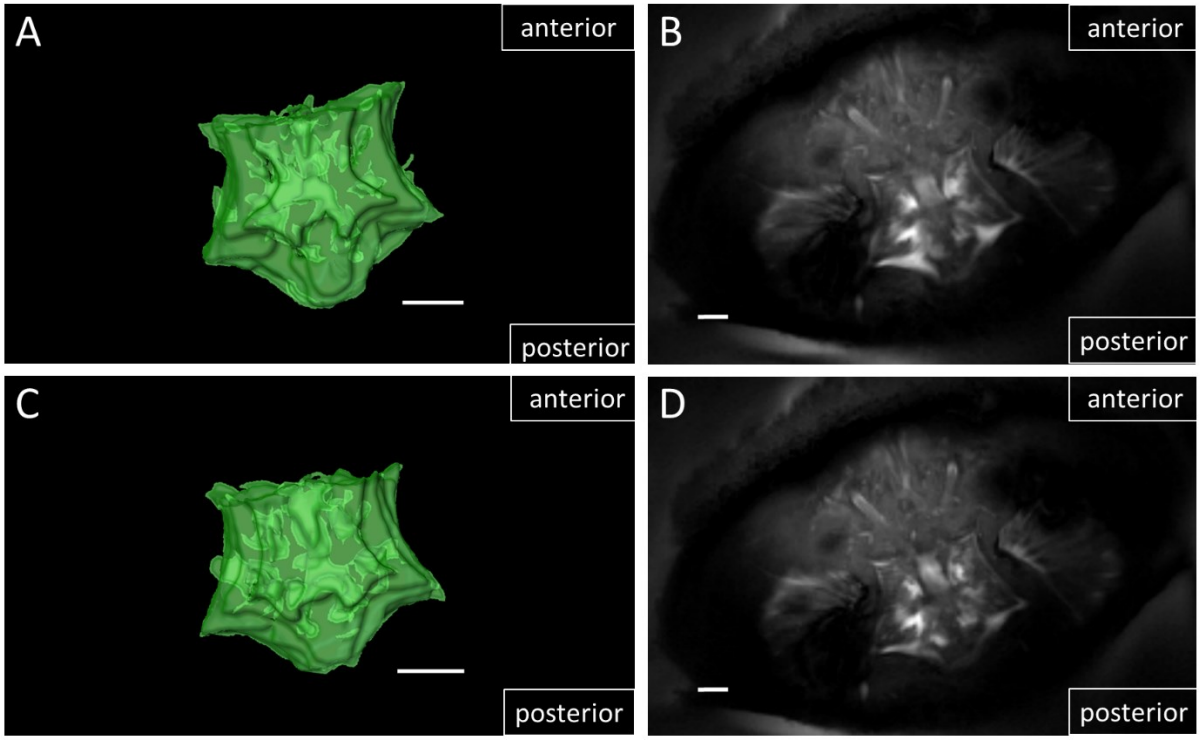

Fig. 38: Differences in inner structure of the ventricle during systole (A, B) and diastole (C, D). (A) 3D reconstruction of the ventricle at systole. Cavities are small due to muscular pressure, especially in the lateral regions. (B) Exemplary IntraGate FLASH scan frame at systole as basis of the 3D model in (A). Anterolateral contraction of the posterior region of the ventricle relative to (D) can be seen. (C) 3D reconstruction of the ventricle at diastole. Cavities expand during relaxation, especially in the lateral areas. (D) Exemplary IntraGate FLASH scan frame at diastole as basis of the 3D model in (C). Relaxation of the ventricle is shown by the relative position of the posterior region to that in (B). Scale bars = 5 mm.

4. Discussion

4.1 Evaluation of the setup

One intention of this study was to simultaneously measure multiple cardiovascular parameters with oxygen consumption rates under changing environmental conditions. To measure oxygen consumption rates, flow-through respirometry was chosen, which is suitable for long-term measurements and pattern identification due to its high temporal resolution. Since water in the experimental chamber is permanently replaced in this method, any local hypoxia, hypercapnia or accumulation of nitrogenous waste as sophisticators known from closed respirometry could mostly be excluded (Svendsen *et al.* 2016). Oxygen levels at the outlet were always above 37% air saturation, and thus above the reported hypoxia tolerance threshold for *C. pagurus* (Bradford and Taylor 1982). On the other hand, flow-through respirometry can introduce mixing and washout problems. An induced change in conditions at the inlet will be adapted exponentially by the outlet signal dependent on the dilution and mixing characteristics of the respiration chamber, and theoretically on water flow velocity and chamber volume (which were constant in the present setup; see equation [7]; Steffensen 1989). The transformation of the water volume depends largely on the dilution factor Ḋ. The higher Ḋ, the faster a certain percentage of volume transformation is reached (Steffensen 1989). Therefore, to reduce time lags due to lagging volume transformation of the water in the respiratory chamber, higher Ḋ were desirable (see appendix, **Tab. 5**). This was achieved by using a respiration chamber only slightly larger than the experimental animal, thus minimizing the water volume around (**Fig. 8**, **Fig. 14**). The 70% volume transformation times are shown in **Tab. 5** in the appendix. The given theoretical approaches do not implement the shape of the respiration chamber. However, to sufficiently correct for the lags, dead volumes and turbulences occurring when choosing rectangular chambers would have to be considered as well. Therefore, oxygen consumption rates were adjusted using quantitative comparison with the heart rates.

Heart rates were measured directly on the cardiac region and therefore showed no time lags. Since strong correlations in time and shape of oxygen consumption rate and cardiac activity patterns have been frequently described (Bradford and Taylor 1982; Burnett and Bridges 1981; Taylor 1982), the time correction for the oxygen consumption signals were done operator mediated by aligning oxygen consumption rates to heart rates under control conditions (see appendix, **Tab. 5**). Differences between calculated values and the applied time correction therefore display inaccuracies due to the shape of the chamber and its hydrodynamic characteristics. Another factor contributing to differences would be the shape of the crab and its ventilation activity, inducing further inaccuracies to theoretical calculations.

Other pitfalls for metabolic rate measurements can result from (potentially diverging) drifts in oxygen reading devices at in- and outlet or undiscovered changes in water flow rates. Both oxygen sensors were subjected to a second calibration at 16°C to reduce the risk of drifts due to miscalculations in temperature compensation and detection errors between two sensors. The water flow through the system remained stable for most of the experiments, due to specific combinations of hose and connector diameters and pump performance. Confirmed by measurements during the experiments, this made it unnecessary to further introduce flow reducing elements as possible factors of flow instability.

The implementation of heart rate measurements in the respiration chamber was achieved through a water tight inlet and the use of dental wax and super-glue to create a water free environment above the cardiac region (**Fig. 14**). Thereby, fixation of the animal not only ensures measurement of quiescent state metabolic rates but also prevented the plethysmograph from being pulled off by the animal (**Fig. 7**). Measurements of heart rates were obtained continuously over the whole period of the experiments. For all animals, the recorded signals showed sufficient quality to reliably detect heart beats and determine their signal integral for stroke volume estimation (Suitability is discussed in 4.3.2). Confirmed by visual control, nearly every heart beat over the course of the experiments was successfully detected by the automatic routine. The routine thus reliably and quickly yielded values in bpm at high temporal resolution over an extended measurement time with minimal error rates in detection.

The implementation of the temperature ramp was ensured by using a thermostat and thermic hoses distributed at the floor of the basin (**Fig. 10**). To minimize the time needed for induction of temperature changes, and ensure homogeneity, the water volume was supposed to be relatively small. The experimental chamber was just submerged in seawater in the basin to ensure similar temperatures in chamber and basin. Hypercapnic conditions in the setup were created using a gas mixing device. An important requirement thereby was stability of the conditions over the whole course of the temperature ramp. Therefore, several water parameters were measured prior to animal experiments and checked for significant differences (**Tab. 3**; see appendix, **Tab. 7**, **Tab. 8**).

The setup used in this study fulfilled all the criteria mentioned above and managed to deal sufficiently with arising method specific problems. The circulation within the setup was kept as simple as possible to reduce error sources to a minimum. Since the setup could provide stable conditions at the given set points for all animals, it was deemed suitable for repeated measurements and comparable results among treatments. No animals died during experimentation or 48 h afterwards.

4.2 Sea water carbonate parameters

Even though the values for $P(CO_2)_w$ differed slightly between 30-50 µatm, the global carbon parameters bicarbonate concentration and dissolved inorganic carbon levels remained stable indicating an overall stable system. The measurements of $P(CO_2)_w$ can differ due to inaccuracies of the measurement system, requiring to involve other parameters to accurately describe water chemistry.

Stability of intended normocapnic and hypercapnic conditions across the temperature ramps was shown by similar values for bicarbonate concentrations and dissolved inorganic carbon (DIC) levels between 12°C and 20°C (see appendix, **Tab. 7**-**Tab. 8**). Stable values of DIC and $[HCO_3^-]_w$ show that the additional carbon added through the gas mix only elevated $P(CO_2)$ and reduced water pH, while not affecting the carbonate buffer system of the setup, which was shown to exert its own effect on crustacean physiology (Maus *et al.* 2018).

4.3 Oxygen consumption rates and cardiovascular performance

4.3.1 Relevance of rhythmic patterns

During experiments, all animals of the Main-group displayed rhythmic patterns of respiration rates and cardiac activity. Previous studies showed these rhythmic patterns are matched by ventilatory activity in undisturbed, resting animals. Phases of elevated activity are interrupted by apnoea and bradycardia, or cardiac arrest (acardia; Bradford and Taylor 1982). This behavior has been reported for several decapod crustaceans (Bradford and Taylor 1982; McMahon and Wilkens 1977) and showed high inter- and intraspecific variability (i.e. Bradford and Taylor 1982; Burnett and Bridges 1981; McMahon and Wilkens 1977). However, the present study is the first to show the persistence of these patterns over several days and to analyze their changes under the influence of ocean warming and acidification.

Generally, differences in durations of pauses are likely dependent on the amount of oxygen stored in the hemolymph and its utilization rate. During pauses, reduction in metabolic energy demands could extend them whereby contribution of anaerobic metabolism can be mostly excluded, as no lactate accumulates in the hemolymph (Bradford and Taylor 1982).

The combination of the described properties of the rhythmic patterns and their common occurrence considered them to represent normal quiescent state activity patterns of *C. pagurus* and other decapod crustaceans (Bradford and Taylor 1982). Quiescent states are irregularly interrupted by phases of elevated activity, prominently displayed by Cancer 4 at 12°C and 14°C (**Fig. 47**, **Fig. 48**).

To allow for comparisons between metabolic rates and cardiovascular performance, all measurements should arise from the same physiological state. For all animals, rhythmic patterns could be observed across almost all temperature steps and conditions for at least 90 min during the measurement time steps (see **Fig. 39**-**Fig. 66**). Comparing these rhythmic patterns across animals, the subsequent analysis shall focus on the physiology of the quiescent state of the animals.

4.3.2 Temperature-dependent changes in rhythmic patterns

All tested individuals displayed a high accordance in shape of respiration rate and heart rate over the measurement times (see **Fig. 39**-**Fig. 66**). The presence of central pattern generators in decapod crustaceans is supported by findings on neural links between the cardioregulatory centers in the central nervous system and the ventilator oscillators (Bradford and Taylor 1982; Burnett and Bridges 1981; Taylor 1982).

For the first time, a temperature-dependent effect on these patterns was analyzed. This was reflected by a rise in median levels of heart rates, oxygen consumption rates and cardiac output (see **Fig. 24**-**Fig. 27**), probably driven by a temperature-dependent rise in oxygen demand (De Wachter and McMahon 1996; Frederich and Pörtner 2000).

For *C. pagurus* acclimated to 10°C, 16°C has been reported to be the upper pejus temperature, indicating the upper border of the species active thermal tolerance range (Metzger *et al.* 2007).

Besides hemolymph partial pressure as used for the detection of breakpoints in thermal tolerance by Metzger *et al.* (2007), Pörtner *et al.* (2017) suggest that breakpoints in general performance parameters such as heart rates and respiration rates provide suitable indicators for reaching pejus temperatures.

Considering this, the observed plateau in heart rates and oxygen consumption rates at 16°C-18°C may indicate, that the animals reached their upper active thermal tolerance limit at these temperatures and would be in line with previously described findings by Metzger *et al.* (2007). However, in the present study, the median provided better reflection of the central tendencies of the considered parameters than the mean, as parameters´ rhythmic patterns were mostly non-normally distributed.

The present study reveals, that the observed temperature-dependent rise in median levels relies on rises of maximum performance levels for heart rate, cardiac output and oxygen consumption rates (at least for Cancer 1 and Cancer 4, partially for Cancer 5), whereas minimum levels remained stable across all temperatures (**Fig. 24**-**Fig. 27**).

With regards to the present findings and analyses, temperature-dependent changes in e.g. heart rate as reported in other studies could theoretically also reflect an increase in maximum performance capacities at stable minimum performance levels (De Wachter and McMahon 1996; Frederich and Pörtner 2000; Metzger *et al.* 2007; Walther *et al.* 2009).

Since only quiescent state rhythmic patterns were considered, these findings represent a temperature-dependent rise in amplitude of the rhythmic patterns of these performance parameters. Distributions obtained for Cancer 4 at 12°C and 14°C however have to be treated with some caution, since the animal showed hardly any rhythmic patterns at these temperatures and instead displayed increased activity for approximately 70% of the measurement time. This may be due to the feeding process, since animals were fed two days before experimentation. Delayed consumption of the offered food may have led to still ongoing digestive activities at the start of experiments. Possible changes of quiescent state metabolic activities in this context have already been described (Ansell 1973).

Animals are able to maintain their energy saving mode involving activity pauses at variable length (translating into reduced aerobic metabolism; Bradford and Taylor 1982) even at high temperatures and should be able to still rely on excess oxygen stored in the hemolymph.

Furthermore, since *C. pagurus* mostly rely on aerobic metabolism during exhibition of rhythmic patterns, it seems that even at 20°C, they are not in the range of anaerobic metabolism and therefore should not have crossed their critical temperature (Pörtner *et al.* 2017; Pörtner and Knust 2007).

However, rising frequencies in activity changes with rising temperatures do not fully compensate for the shortening of pauses in metabolic- and cardiac activity since the overall time spent in the bottom 25% declines (compare **Fig. 28**- e.g. **Fig. 29** for Cancer 1). Consequently, for the heart rate signals, it could be shown, that even though the frequencies of rhythmic patterns rise with rising temperatures, the amount of overall time spent in bradycardia declines (compare e.g. **Fig. 28**- **Fig. 29** for Cancer 1).

A shortening of time spent on low metabolic and cardiac activity has already been reported for *C. pagurus* under hypoxic conditions (Burnett and Bridges 1981). Additionally, Metzger *et al.* (2007) reported declining hemolymph oxygen partial pressures with rising temperatures for *C. pagurus*. The combination of less oxygen stored in the hemolymph and a higher rate of utilization may shorten the time the animal is able to maintain its aerobic metabolism from stored oxygen and therefore shorten the amount of time spent in the minimum levels of the heart rate range (**Fig. 28**).

According to this apparent mismatch of oxygen supply and demand at higher temperatures reducing the times spent in bradycardia, the times spent at maximum heart rates do not increase much: At both, low and high temperatures, top levels of heart rates are distinct peaks, usually constituting less than a third of the measurement time (**Fig. 28**).

It seems like in the quiescent state, short phases of top performance are sufficient to cover acute metabolic needs and still enable (shorter) pauses with rising temperatures. This may represent a more economical use of energy than steadily performing at medium activities (Burnett and Bridges 1981). Nevertheless, the amount of time *C. pagurus* displayed high, non-fluctuating heart- and oxygen consumption rates also increased with higher temperatures (personal observations, data not shown), signifying a generally positive correlation between activity and temperature.

During pauses, the signal integrals, presumed to represent the cardiac stroke volume, show minimum levels as seen for the heart rates and oxygen consumption rates (e.g. **Fig. 21**). Previous studies propose a negative correlation between stroke volumes and heart rates due to increased hydrodynamic resistance, resulting in insufficient filling of the ventricle at high heart rates (De Wachter and McMahon 1996; Wilkens 1981). Concerning the applicability of the signal integral as a stroke volume proxy, in this study both integral signals and heart rates increase with increasing temperature (**Fig. 24**-**Fig. 27**).

The absolute values of the obtained integrals of the heart beat signals as possible proxies of the stroke volume strongly depend on the position of the plethysmograph on the carapace of the animal and their anatomy. Some animals displayed very strong signals (high signal-to-noise-ratio) which may be due to bigger hearts or less signal absorbing tissue between the heart and the detecting sensor of the plethysmograph. The integral signals therefore varied highly between the animals and to enable comparability, the signals of every animal were normalized to their average signal at 12°C (control conditions). However, the temperature-dependent trends of the normalized integral signals are highly influenced by the signal under control conditions, limiting their comparability to quantitative studies.

At higher heart rates, the cutoff-like shape of the signal integrals (**Fig. 23**) on the other hand may be indicative for a decline in stroke volume due to previously described physical limitations (De Wachter and McMahon 1996; Wilkens 1981). An additional explanation would be, that the animal has simply approached the volume limits of the ventricle. So far, as a qualitative, albeit non-invasive technique, IR-PPG does not support clear conclusions on the causes.

However, since integral signals follow the same patterns as the heart rate signals during a given time frame, and display the existence of upper limits as described for the stroke volume in the literature, this study provides further evidence, that the integral signal of IR-PPG can be used as a valid proxy for relative changes in stroke volume of brachyuran crabs (first use by Giomi and Pörtner 2013).

The cardiac output proxy was calculated by multiplication of the heart rate with the integral signal as proxy of the stroke volume. Observed increases in cardiac output levels are in line with previous findings, which also reported an increase in cardiac output with rising temperature for *Metacarcinus magister* (De Wachter and McMahon 1996).

In the present study, the cardiac output shows no limitation as observed for the signal integrals, since heart rates represent much higher multipliers than given by the normalized values for the integral signal, limiting the validity of the cardiac output proxy.

4.3.3 CO_2-dependent changes in rhythmic patterns

Previous studies provide evidence that high concentrations of CO_2 cause a narrowing of the thermal window of *C. pagurus* described by reduced arterial oxygen levels (Metzger *et al.* 2007). Narcotic effects of CO_2, reducing general activity and oxygen uptake rates were already seen for other marine invertebrates (Michaelidis *et al.* 2005; Pörtner *et al.* 1998; Pörtner *et al.* 2005; Pörtner *et al.* 2004). For the spider crab *H. araneus*, elevated CO_2 concentrations cause decreased arterial oxygen tensions and a narrowed thermal window as well. There however, CO_2 had a dose-dependent positive chronotropic effect on heart rates with rising temperatures (Walther *et al.* 2009). It appears, that different strategies on how to deal with ocean warming and acidification exist across marine invertebrates and even within the order of decapod crustaceans.

In the present study on *C. pagurus*, the variable distributions of the measured performance parameters did not indicate the occurrence of one distinct reaction as described above. This is likely due to the high interindividual variation as Cancer 1 displayed depression of heart rates and oxygen consumption under CO_2 and Cancer 5 elevation of these parameters. These effects are further aggravated by the small sample size of three animals. The chosen CO_2 concentrations and temperature changes do not trigger consistent reactions in *C. pagurus* already obvious when comparing central tendencies of distributions. Signal integrals and cardiac do not show any CO_2-dependent changes in distributions.

Therefore, it may be more appropriate to focus on changes in activity over time, as demonstrated for the heart activity. The results of the pattern analysis of cardiovascular performance revealed a consistent pattern of decreased heart activity for all tested animals, indicating narcotic effects of elevated CO_2 levels on the heart activity of *C. pagurus*. Prolonged reduction of heart activity of the animals may indirectly lead to reduced oxygen uptake, due to neuronal coupling of cardioregulation and ventilation (Bradford and Taylor 1982; Burnett and Bridges 1981; Taylor 1982) and would further provide possible explanations for reduced oxygen tensions observed by Metzger *et al.* (2007). On the other hand, this coupling indicates, that animals in the present study may also show a drop in arterial oxygen tension. In combination, the results of the present study and those by Metzger *et al.* (2007) imply that narcotic effects on the heart activity by CO_2 may also cause reduced oxygen uptake via reduced ventilation, which subsequently causes reduction in arterial oxygen tensions.

This is in contrast to findings in *H. araneus,* where reduced oxygen tensions were presented to be caused by higher oxygen demands due to a CO_2-dependent stimulation of the heart activity (Walther *et al.* 2009).

Both reactions however lead to reduced thermal tolerances in the particular organism (Metzger *et al.* 2007; Walther *et al.* 2009). Possible reductions of thermal tolerance for *C. pagurus* in the present study with regard to the OCLTT concept could have been detected by observing CO_2-dependent shifts in breakpoints of the performance parameters (Frederich and Pörtner 2000). However, the previously described temperature-dependent performance breakpoints (16°C-18°C) and maintained aerobic metabolism (rhythmic patterns) at 20°C do not shift under elevated CO_2 concentrations and therefore imply, that the upper pejus- and critical temperatures and the thermal tolerance window do not differ from that under normocapnic conditions.

The non-affection of the thermal window of *C. pagurus* by CO_2 concentrations beyond the year 2100 used in this study suggests that the narcotic effects on the heart activity over time can be considered to be light in comparison to the effects shown by Metzger *et al.* (2007) clearly narrowing the thermal window. This discrepancy may be due to the dose-dependent CO_2 effects already seen for *H. araneus* (Walther et al. 2009).

In an ecological context, these results indicate, that *C. pagurus* in the North Sea may not be as critically affected as other decapod crustaceans (*H. araneus*) by CO_2 concentrations expected beyond the year 2100. While possible implications for the general fitness by light narcotic effects on the animals´ heart activity over time were not investigated in the present study, they cannot be excluded.

4.4 *In vivo* MRI

4.4.1 Anatomic reconstruction of the heart

In vivo MRI has already been used in previous studies on crustaceans to detect reactions to elevated CO_2 or changing temperatures using velocity mapping of blood flow and real time cardiac images (Bock *et al.* 2012; Bock *et al.* 2001). However, these studies focused more on functional properties than on anatomical aspects. This study provides the first non-invasive *in vivo* study on the anatomy of the decapod crustacean heart.

The hardware setup was optimized to provide sufficient tissue contrast of the scans, even though the animals were surrounded by seawater. This was achieved by the combined use of volume resonator for signal excitation and receive-only surface coil for signal reception (see **Fig. 19**).

To cover the entire heart, 20 coronal scans with a thickness of 1 mm were conducted. This thickness proved to be the best compromise for imaging time and image resolution. The 3D model resulted from reconstruction could then be used to study anatomical structures, that have already been described using conventional terminal methods.

From the 3D reconstructions, vessels of 4 of the 5 arterial systems originating at the heart could be displayed (**Fig. 35**). The only artery missing is the anterior aorta, which should be located between the hepatic arteries at the medial dorsal anterior aspect of the heart (McGaw and Reiber 2002). However, the anterior aorta is very small in diameter and apparently had a similar image contrast to parts of the digestive tracks located anteriorly to the heart. Further adjustments to the imaging parameters, with regards to image contrast (echo- and recovery time, flip angle) or resolution may be necessary to decisively visualize the anterior aorta. Still, scan parameters allowed for motion-artefact-free images.

In the reconstructions of the ventricle, three pairs of ostia, located dorsally, ventrally and laterally could be identified (**Fig. 36**). At diastole, hemolymph enters the heart through these ostia. Their observed locations are in line with previous findings (Maynard 1960). Furthermore, in single-slice-images (**Fig. 19**), the ventricle appears to have a sponge-like structure. The underlying trabecular networks have already been described on microscopic levels and are thought to facilitate coordinated contraction (Howse *et al.* 1971).

The 3D reconstructions also revealed (potentially functional) cavities inside the ventricle. These cavities originate near the ostia and lead to the origins of the arteries of the arterial system (**Fig. 36**). These structures may channel hemolymph towards the arteries, possibly enhancing the pumping efficiency of the decapod crustacean heart.

The complex structure of the ventricle and proposed enhanced efficiency of pumping related to the relatively complex structure of the remaining vascular system in decapod crustaceans may help redirect hemolymph through its different arterial systems. Even though the heart is single-chambered, these findings corroborate the high complexity of the circulatory system of decapod crustaceans at ventricular levels.

4.4.2 Determination of stroke volume using cine MRI

As for the anatomical reconstructions, the exemplary determination of stroke volume was done using *in vivo* MRI, namely 13 IntraGate FLASH scans covering the entire heart.When comparing systolic and diastolic states, it was found that contractions in anterolateral direction in the posterior region of the heart and lateral contractions in its lateral regions were dominant. Contraction of the anterior region was rather poor, even though it could be observed. Due to the coronal direction of the scans, no statements could be made about the albeit small dorsoventral movements observed in separate experiments (B. Maus, personal communication).

Volume changes of the inner cavities of the ventricle may be directly linked to the directions of contraction. This may be due to the previously described contraction directions synergistically minimizing cavity volume in these areas. Since it has already been shown, that ostia close with the onset of contraction (Maynard 1960), the hemolymph in the lateral areas may be directed towards the cavities near the entries to the arteries. This supports the previous assumptions based on the stationary anatomical scans, that the cavities enable directed flow of hemolymph into different vessels.

To finally determine the stroke volume changes in muscle volume and cavity volume were calculated. Both cavity volume changes were approximately 0.1 mL. Apparently, changes in ventricle volume as translators of muscle contraction nearly fully transfer into minimizing the cavity volume.

Thermodilution methods for *C. pagurus* and pulse Doppler flowmeter measurements for *M. magister* displayed values for the stroke volume ranging from 0.12-0.75 mL/kg (Burnett and Bridges 1981; De Wachter and McMahon 1996). The fact that the value from one *C. pagurus* in this study is a little smaller may be due to the different sizes and weights of the animals. The individual used in this study weighted 308 g, whereas *C. pagurus* used by Burnett and Bridges (1981) weighted between 400-750 g and *M. magister* in the study of De Wachter and McMahon (1996) weighted between 500-765 g. Despite these differences in sizes of the animals, ratios of stroke volume to body weight obtained in this study are only 5% smaller than the ones obtained by De Wachter and McMahon (1996).

A possible reason for these small volume differences might be the exclusion of hemolymph collecting in the trabecular structure of the ventricle during reconstructions. Therefore, the actual stroke volume might be little higher than the calculations in the present study. Furthermore, since reconstructions and choosing of reconstructed frames are fully operator mediated, mistakes in selecting of reconstructed tissues cannot be fully excluded.

Considering this, the approach presented in this study is a first step for the non-invasive quantification of stroke volume by direct measurement of ventricular contraction applied to an aquatic invertebrate. Moreover, the use of MRI reveals further details of the pumping mechanism and acknowledges the complexity of the cardiac activity of decapod crustaceans.

4.5 Perspectives

The present data derived from the temperature ramp experiments provide room for even further analysis due to their high resolution and continuity. This would include the assignment of methods used for exemplary pattern analysis of heart activity on the other parameters. This may offer interesting results, for example towards the oxygen consumption rates. The stroke volume is known to change in response to decreasing heart rates under hypoxia to maintain same levels of cardiac output (Guadagnoli *et al.* 2007; Reiber and McMahon 1998; Reiber *et al.* 1997; Wheatly and Taylor 1981; Wilkes and McMahon 1982). Deeper analysis of correlations to heart rates and cardiac output may reveal effects not obvious at first sight. Correlations between heart rates and integral offer potential to reveal a CO_2-dependent shift of the observed and discussed maximum performance levels of the integral signal (**Fig. 23**). This would also apply for correlation analyses between the integral signal and the oxygen consumption rates.

As it is proposed that narcotic effects on heart activity indirectly cause decreased oxygen uptake via reduced ventilation, simultaneous measurements of oxygen hemolymph partial pressure and ventilation rate would provide possible evidence for this assumption.

For the possible detection of CO_2-dependent changes in breakpoints of the heart rates, their implementation into an Arrhenius plot may provide another option. Additionally, changes in integrals of the heart rate rhythmic patterns may provide information about changes in performance over time. Together, these approaches would generate additional information about minute changes in thermal tolerance windows. Generally, further experiments under the same conditions may be necessary to achieve better representation of the population and obtain general response patterns by minimizing effects of interindividual variability.

Beyond that, possible affection of the long-term performance by the observed narcotic effects on *C. pagurus* requires further investigation. Additionally, the use of higher CO_2-concentrations in the experiments may trigger more distinct dose-dependent effects.

The first determination of the stroke volume using MRI requires further validation before any future applications. Comparability to previously established (invasive) methods still needs to be confirmed. Optimal scan parameters would help to streamline the measurement and reconstruction process. At approximately 1 h, the scan time is still relatively high and definitely too high to detect changes at the temporal resolution provided by the IR-PPG measurements. The aim would be, not having to consider all layers of the heart, but only a few, which are representative of the complete ventricular contraction and its changes.

4.6 Conclusions

The employed setup enabled simultaneous, non-invasive measurements of heart rates (and associated cardiac parameters derived from these signals) and oxygen consumption rates in response to reliable manipulations of temperatures and $P(CO_2)_w$.

The increasing amplitude of rhythmic patterns in response to rising temperatures mostly depended on increases at the maximum level, whereas minimum levels remained stable. Temperature-dependent changes in frequency and shape of these fluctuations suggest that the energetic costs for maintaining longer phases of metabolic and cardiac inactivity might be higher than their benefits.

Beside these temperature-dependent effects, it could be shown, that CO_2-concentrations around 1400 µatm can have light narcotic effects on the heart activity over time of *C. pagurus*. However, the diverse responses of the other parameters and no observed shifts in performance breakpoints imply, that the thermal tolerance window under global change conditions beyond the year 2100 is not narrowed under OCLTT criteria. Possible implications for long-term performance require further investigation.

IR-PPG provided valid proxies for the relative changes in stroke volume, and signals showed previously described limitations at higher heart rates. However, this method is still not suitable for detection of quantitative changes. Therefore, it was aimed to develop a non-invasive approach to quantify the stroke volume. Absolute values for the particular animals could then be used as references for relative changes obtained by IR-PPG in future studies.

In the course of this study, MRI could be validated as a powerful tool to enable anatomical studies on the heart of *C. pagurus*, despite the presence of seawater around the animal. Complex inner structures of the ventricle could be revealed, likely enhancing the pumping mechanism.

The non-invasive measurement of stroke volume using MRI provided realistic values in comparison to established references. Additionally, it allowed for observations on the details of the pumping mechanism. Adaptation and simplification of this still time-consuming method to research questions involving time series coverage of the stroke volume provides demanding challenges for the future.

References

NOAA´s Climate Change Web Portal. Physical Sciences Division, Earth System Research Laboratory. 2018

Alexandrowicz J, Carlisle D (1953) Some experiments on the function of the pericardial organs in Crustacea. Journal of the Marine Biological Association of the United Kingdom 32: 175-192

Ansell A (1973) Changes in oxygen consumption, heart rate and ventilation accompanying starvation in the decapod crustacean Cancer pagurus. Netherlands Journal of Sea Research 7: 455-475

Benjamini Y, Hochberg Y (1995) Controlling the false discovery rate: a practical and powerful approach to multiple testing. Journal of the royal statistical society Series B (Methodological): 289-300

Bock C, Dogan F, Poertner HO (2012) Coping with a changing ocean: Real-time cardiac MRI on an animal model with a natural cardiovascular disorder. In: Research A-W-IfPaM (ed). Bermerhaven, Germany

Bock C, Frederich M, Wittig R-M, Pörtner H-O (2001) Simultaneous observations of haemolymph flow and ventilation in marine spider crabs at different temperatures: a flow weighted MRI study. Magnetic resonance imaging 19: 1113-1124

Boutilier RG, Heming TA, Iwama GK (1984) Physicochemical parameters for use in fish respiratory physiology. Fish physiology. Elsevier, pp. 403-430

Bradford S, Taylor A (1982) The respiration of Cancer pagurus under normoxic and hypoxic conditions. Journal of Experimental Biology 97: 273-288

Brand MD (1990) The contribution of the leak of protons across the mitochondrial inner membrane to standard metabolic rate. Journal of Theoretical Biology 145: 267-286

Breteler WK (1975) Oxygen consumption and respiratory levels of juvenile shore crabs, Carcinus maenas, in relation to weight and temperature. Netherlands Journal of Sea Research 9: 243-254

Burnett LE, Bridges CR (1981) The physiological properties and function of ventilatory pauses in the crabCancer pagurus. Journal of Comparative Physiology B: Biochemical, Systemic, and Environmental Physiology 145: 81-88

Ciais P, Sabine C, Bala G, Bopp L, Brovkin V, Canadell J, Chhabra A, DeFries R, Galloway J, Heimann M, Jones C, Le Quéré C, Myneni RB, Piao S, Thornton P (2013) Carbon and Other Biogeochemical Cycles. In: Stocker TF, Qin D, Plattner G-K, Tignor M, Allen SK, Boschung J, Nauels A, Xia Y, Bex V, Midgley PM (eds) Climate Change 2013: The Physical Science Basis Contribution of Working Group I to the Fifth Assessment Report of the Intergovernmental Panel on Climate Change. Cambridge University Press, Cambridge, United Kingdom and New York, NY, USA, pp. 465–570

COSYNA (2018) COSYNA data web portal, parameter: water temperature. Helmholtz-Centre Geesthacht, Centre for Materials and Coastal Research

Cuculescu M, Hyde D, Bowler K (1998) Thermal tolerance of two species of marine crab, Cancer pagurus and Carcinus maenas. Journal of Thermal Biology 23: 107-110

De Wachter B, McMahon BR (1996) Temperature effects on heart performance and regional hemolymph flow in the crab Cancer magister. Comparative Biochemistry and Physiology Part A: Physiology 114: 27-33

Dejours P (1975) Principles of Comparative Respiratory Physiology. New York: American Elsevier Publishing Co

Depledge M (1984) Photoplethysmography—a non-invasive technique for monitoring heart beat and ventilation rate in decapod crustaceans. Comparative Biochemistry and Physiology Part A: Physiology 77: 369-371

Depledge M, Andersen B (1990) A computer-aided physiological monitoring system for continuous, long-term recording of cardiac activity in selected invertebrates. Comparative Biochemistry and Physiology Part A: Physiology 96: 473-477

Dickson A (2010) The carbon dioxide system in seawater: equilibrium chemistry and measurements. In: Riebesell U, Fabry VJ, Hansson L, J-P G (eds) Guide to best practices in ocean acidification research and data reporting. European Comission, Directorate-General for Research, Brussels, pp. 17-40

Doney SC, Fabry VJ, Feely RA, Kleypas JA (2009) Ocean acidification: the other CO2 problem.
Ege R, Krogh A (1914) On the relation between the temperature and the respiratory exchange in fishes. Internationale Revue der gesamten Hydrobiologie und Hydrographie 7: 48-55

Fatt P, Katz B (1953) The electrical properties of crustacean muscle fibres. The Journal of physiology 120: 171-204

Frederich M, Pörtner HO (2000) Oxygen limitation of thermal tolerance defined by cardiac and ventilatory performance in spider crab, Maja squinado. American Journal of Physiology-Regulatory, Integrative and Comparative Physiology 279: R1531-R1538

Fry F (1971) The effect of environmental factors on the physiology of fish. Fish physiology: 1-98
Giomi F, Fusi M, Barausse A, Mostert B, Pörtner H-O, Cannicci S (2014) Improved heat tolerance in air drives the recurrent evolution of air-breathing. Proceedings of the Royal Society of London B: Biological Sciences 281: 20132927

Giomi F, Pörtner HO (2013) A role for haemolymph oxygen capacity in heat tolerance of eurythermal crabs. Frontiers in physiology 4: 110

Guadagnoli J, Tobita K, Reiber C (2007) Assessment of the pressure–volume relationship of the single ventricle of the grass shrimp, Palaemonetes pugio. Journal of Experimental Biology 210: 2192-2198

Gutowska MA, Pörtner HO, Melzner F (2008) Growth and calcification in the cephalopod Sepia officinalis under elevated seawater pCO2. Marine Ecology Progress Series 373: 303-309

Hartmann DL, Klein Tank AMG, Rusticucci M, Alexander LV, Brönnimann S, Charabi Y, Dentener FJ, Dlugokencky EJ, Easterling DR, Kaplan A, Soden BJ, Thorne PW, Wild M, Zhai PM (2013) Observations: Atmosphere and Surface. In: Stocker TF, Qin D, Plattner G-K, Tignor M, Allen SK, Boschung J, Nauels A, Xia Y, Bex V, Midgley PM (eds) Climate Change 2013: The Physical Science Basis Contribution of Working Group I to the Fifth Assessment Report of the Intergovernmental Panel on Climate Change. Cambridge University Press, Cambridge, United Kingdom and New York, NY, USA, pp. 159–254

Hochachka P, Somero G (2002) Biochemical Adaptation, Mechanism and Process in Physiological Evolution Oxford University Press. USA, New York

Hoegh-Guldberg O (2005) Low coral cover in a high-CO2 world. Journal of Geophysical Research: Oceans 110

Howse HD, Ferrans VJ, Hibbs RG (1971) A light and electron microscopic study of the heart of a crayfish, Procambarus clarkii (Giraud). II. Fine structure. Journal of morphology 133: 353-373
Hoyle G, Wiersma C (1958) Coupling of membrane potential to contraction in crustacean muscles. The Journal of physiology 143: 441-453

IPCC (2007) Climate Change 2007, Fourth Assessment Report of the Intergovernmental Panel on Climate Change. Cambridge University Press, Cambridge

Joyce W, Egginton S, Farrell AP, Crockett EL, O'Brien KM, Axelsson M (2018) Exploring nature's natural knockouts: In vivo cardiorespiratory performance of Antarctic fishes during acute warming. Journal of Experimental Biology 221: jeb183160

Kaestner A, Levi HW, Levi LR (1970) Invertebrate zoology. Interscience Publishers,
Kautsky H (1939) Quenching of luminescence by oxygen. Transactions of the Faraday Society 35: 216-219

Lannig G, Eilers S, Pörtner HO, Sokolova IM, Bock C (2010) Impact of ocean acidification on energy metabolism of oyster, Crassostrea gigas—changes in metabolic pathways and thermal response. Marine drugs 8: 2318-2339

Levitus S, Antonov J, Boyer T (2005) Warming of the world ocean, 1955–2003. Geophysical Research Letters 32

Madeira D, Vinagre C, Diniz MS (2016) Are fish in hot water? Effects of warming on oxidative stress metabolism in the commercial species Sparus aurata. Ecological indicators 63: 324-331

Maus B, Bock C, Pörtner H-O (2018) Water bicarbonate modulates the response of the shore crab Carcinus maenas to ocean acidification. Journal of Comparative Physiology B: 1-16

Maynard DM (1960) Circulation and heart function. The Physiology of Crustaceans 1: 161-226

McDonald D, McMahon B, Wood C (1977) Patterns of heart and scaphognathite activity in the crab Cancer magister. Journal of Experimental Zoology Part A: Ecological Genetics and Physiology 202: 33-43

McGaw IJ (2005) The decapod crustacean circulatory system: a case that is neither open nor closed. Microscopy and Microanalysis 11: 18-36

McGaw IJ, Reiber CL (2002) Cardiovascular system of the blue crab Callinectes sapidus. Journal of morphology 251: 1-21

McMahon B, Wilkens J (1977) Periodic respiratory and circulatory performance in the red rock crab Cancer productus. Journal of Experimental Zoology Part A: Ecological Genetics and Physiology 202: 363-374

McMahon BR, Burnett LE (1990) The crustacean open circulatory system: a reexamination. Physiological Zoology 63: 35-71

McMahon BR, Wilkens JL (1972) Simultaneous apnoea and bradycardia in the lobster Homarus americanus. Canadian Journal of Zoology 50: 165-170

Melzner F, Gutowska M, Langenbuch M, Dupont S, Lucassen M, Thorndyke M, Bleich M, Pörtner H-O (2009) Physiological basis for high CO 2 tolerance in marine ectothermic animals: pre-adaptation through lifestyle and ontogeny? Biogeosciences 6: 2313-2331
Metzger R, Sartoris FJ, Langenbuch M, Pörtner HO (2007) Influence of elevated CO 2 concentrations on thermal tolerance of the edible crab Cancer pagurus. Journal of Thermal Biology 32: 144-151

Meurant G (2012) The Biology of Crustacea: Volume 3: Neurobiology, Structure and Function. Elsevier Science

Michaelidis B, Ouzounis C, Paleras A, Pörtner HO (2005) Effects of long-term moderate hypercapnia on acid–base balance and growth rate in marine mussels Mytilus galloprovincialis. Marine Ecology Progress Series 293: 109-118

Neal K, Wilson E (2008) Edible crab-*Cancer Pagurus*. Marine Life Information Network.

Nobes C, Brown GC, Olive PN, Brand MD (1990) Non-ohmic proton conductance of the mitochondrial inner membrane in hepatocytes. Journal of Biological Chemistry 265: 12903-12909

Orr JC, Maier-Reimer E, Mikolajewicz U, Monfray P, Sarmiento JL, Toggweiler J, Taylor NK, Palmer J, Gruber N, Sabine CL (2001) Estimates of anthropogenic carbon uptake from four three-dimensional global ocean models. Global Biogeochemical Cycles 15: 43-60

Parmesan C, Yohe G (2003) A globally coherent fingerprint of climate change impacts across natural systems. Nature 421: 37

Perry AL, Low PJ, Ellis JR, Reynolds JD (2005) Climate change and distribution shifts in marine fishes. science 308: 1912-1915

Pierrot DEL, Wallace DWR (2006) MS Excel Program Developed for CO2 System Calculations. ORNL/CDIAC-105a. Carbon Dioxide Information Analysis Center, Oak Ridge National Laboratory, U.S. Department of Energy.

Pörtner H-O, Bock C, Mark FC (2017) Oxygen-and capacity-limited thermal tolerance: bridging ecology and physiology. Journal of Experimental Biology 220: 2685-2696

Pörtner H-O, Giomi F (2013) Nothing in experimental biology makes sense except in the light of ecology and evolution–correspondence on J. Exp. Biol. 216, 2771-2782. Journal of Experimental Biology 216: 4494-4495

Pörtner H-O, Reipschläger A, Heisler N (1998) Acid-base regulation, metabolism and energetics in Sipunculus nudus as a function of ambient carbon dioxide level. Journal of Experimental Biology 201: 43-55

Pörtner HO, Knust R (2007) Climate change affects marine fishes through the oxygen limitation of thermal tolerance. science 315: 95-97

Pörtner HO, Langenbuch M, Michaelidis B (2005) Synergistic effects of temperature extremes, hypoxia, and increases in CO2 on marine animals: From Earth history to global change. Journal of Geophysical Research: Oceans 110

Pörtner HO, Langenbuch M, Reipschläger A (2004) Biological impact of elevated ocean CO 2 concentrations: lessons from animal physiology and earth history. Journal of Oceanography 60: 705-718

Reiber C, McMahon B (1998) The effects of progressive hypoxia on the crustacean cardiovascular system: a comparison of the freshwater crayfish,(Procambarus clarkii), and the lobster (Homarus americanus). Journal of Comparative Physiology B 168: 168-176

Reiber C, McMahon B, Burggren W (1997) Cardiovascular functions in two macruran decapod crustaceans (Procambarus clarkii and Homarus americanus) during periods of inactivity, tail flexion and cardiorespiratory pauses. Journal of Experimental Biology 200: 1103-1113

Roule L (1898) L'anatomie comparée des animaux basée sur l'embryologie, ornée de 1202 figures. Masson

Sabine CL, Feely RA (2007) The oceanic sink for carbon dioxide. Greenhouse gas sinks 31

Sandeman D (1967) The vascular circulation in the brain, optic lobes and thoracic ganglia of the crab Carcinus. Proceedings of the Royal Society of London B: Biological Sciences 168: 82-90

Spoor W (1946) A quantitative study of the relationship between the activity and oxygen consumption of the goldfish, and its application to the measurement of respiratory metabolism in fishes. The Biological Bulletin 91: 312-325

Steffensen JF (1989) Some errors in respirometry of aquatic breathers: how to avoid and correct for them. Fish Physiology and Biochemistry 6: 49-59

Svendsen MBS, Bushnell P, Steffensen JF (2016) Design and setup of intermittent-flow respirometry system for aquatic organisms. Journal of Fish Biology 88: 26-50

Taylor E (1982) Control and co-ordination of ventilation and circulation in crustaceans: responses to hypoxia and exercise. Journal of Experimental Biology 100: 289-319

Taylor E, Butler P, Sherlock P (1973) The respiratory and cardiovascular changes associated with the emersion response ofCarcinus maenas (L.) during environmental hypoxia, at three different temperatures. Journal of Comparative Physiology A: Neuroethology, Sensory, Neural, and Behavioral Physiology 86: 95-115

Taylor E, Wheatly MG (1980) Ventilation, heart rate and respiratory gas exchange in the crayfishAustropotamobius pallipes (Lereboullet) submerged in normoxic water and following 3 h exposure in air at 15° C. Journal of Comparative Physiology B: Biochemical, Systemic, and Environmental Physiology 138: 67-78

Taylor EW, Wheatly MG (1982) The effects of dehydration during aerial exposure on the distribution of water and ions in the freshwater crayfish Austropotamobius pallipes (Lereboulle). Journal of comparative Physiology

Team RDC (2008) R: A language and environment for statistical computing. R Foundation for Statistical Computing, Vienna, Austria

Thomsen J, Melzner F (2010) Moderate seawater acidification does not elicit long-term metabolic depression in the blue mussel Mytilus edulis. Marine Biology 157: 2667-2676

Uppström LR (1974) The boron/chlorinity ratio of deep-sea water from the Pacific Ocean. Deep Sea Research and Oceanographic Abstracts 21: 161-162

Van Der Kloot W (1970) The electrophysiology of muscle fibers in the hearts of decapod crustaceans. Journal of Experimental Zoology Part A: Ecological Genetics and Physiology 174: 367-380

Walther K, Sartoris FJ, Bock C, Pörtner H-O (2009) Impact of anthropogenic ocean acidification on thermal tolerance of the spider crab Hyas araneus. Biogeosciences 6: 2207-2215

Waters JF, Millero FJ (2013) The free proton concentration scale for seawater pH. Marine Chemistry 149: 8-22

Wearing HJ (2010) Spectral Analysis in R. In: University M (ed). Hamilton, Canada

Wheatly MG, Taylor E (1981) The effect of progressive hypoxia on heart rate, ventilation, respiratory gas exchange and acid-base status in the crayfish Austropotamobius pallipes. Journal of Experimental Biology 92: 125-141

Whiteley N (2011) Physiological and ecological responses of crustaceans to ocean acidification. Marine Ecology Progress Series 430: 257-271

Wilkens J, Wilkens L, McMahon B (1974) Central control of cardiac and scaphognathite pacemakers in the crab, Cancer magister. Journal of Comparative Physiology A: Neuroethology, Sensory, Neural, and Behavioral Physiology 90: 89-104

Wilkens JL (1981) Respiratory and circulatory coordination in decapod crustaceans. Locomotion and energetics in arthropods. Springer, pp. 277-298

Wilkes P, McMahon B (1982) Effect of maintained hypoxic exposure on the crayfish Orconectes rusticus: I. Ventilatory, acid-base and cardiovascular adjustments. Journal of Experimental Biology 98: 119-137

Young RE (1975) Neuromuscular control of ventilation in the crabCarcinus maenas. Journal of comparative physiology 101: 1-37

Appendix

Calculations

Dilution factors

Cancer 1 normocapnia: $\dot{D} = \frac{400\,\frac{mL}{min}}{1520\,mL} = 0.263\,\frac{1}{min}$

Cancer 1 hypercapnia: $\dot{D} = \frac{400\,\frac{mL}{min}}{1520\,mL} = 0.263\,\frac{1}{min}$

Cancer 4 normocapnia: $\dot{D} = \frac{460\,\frac{mL}{min}}{1520\,mL} = 0.303\,\frac{1}{min}$

Cancer 4 hypercapnia: $\dot{D} = \frac{400\,\frac{mL}{min}}{1520\,mL} = 0.263\,\frac{1}{min}$

Cancer 5 normocapnia: $\dot{D} = \frac{400\,\frac{mL}{min}}{1520\,mL} = 0.263\,\frac{1}{min}$

Cancer 5 hypercapnia: $\dot{D} = \frac{414\,\frac{mL}{min}}{1520\,mL} = 0.270\,\frac{1}{min}$

Calulations of time points of 70% volume transformation

Transformation (%) = $100*(1-e^{-\dot{D}*t})$

$70 = 100*(1-e^{-\dot{D}*t})$

$\frac{\ln(0.3)}{-\dot{D}} = t$

Cancer 1 normocapnia: $t = \frac{\ln(0.3)}{-0.263\,\frac{1}{min}} = 4.58$ min

Cancer 1 hypercapnia: $t = \frac{\ln(0.3)}{-0.263\,\frac{1}{min}} = 4.58$ min

Cancer 4 normocapnia: $t = \frac{\ln(0.3)}{-0.303\,\frac{1}{min}} = 3.97$ min

Cancer 4 hypercapnia: $t = \frac{\ln(0.3)}{-0.263\,\frac{1}{min}} = 4.58$ min

Cancer 5 normocapnia: $t = \frac{\ln(0.3)}{-0.299\,\frac{1}{min}} = 4.58$ min

Cancer 5 hypercapnia: $t = \frac{\ln(0.3)}{-0.270\,\frac{1}{min}} = 4.46$ min

Calculations of time lags

Calculation of the time lags for comparison depend on the dilution factor Ḋ (Spoor 1946; Steffensen 1989):

$$\dot{D} = \frac{\dot{V}_w}{Vr} \quad [6]$$

Where V̇w = water flow in L/min and

Vr = Volume of the animal chamber minus animal volume in l.

In this case, the dilution factor describes how effective the volume gets exchanged by the water flow. It can then be embedded into a formula for transformation of the volume:

$$\text{Transformation}\ (\%) \ = \ 100 \cdot (1 - e^{-\dot{D} * t}) \quad [7]$$

High dilution factors between 1 $\frac{1}{\text{min}}$ and 0.25 $\frac{1}{\text{min}}$ reach 99% of volume therefore exchange within 4.7 minutes and 18 minutes. 70% of volume exchange are reached within 1.25 minutes (for 1 $\frac{1}{\text{min}}$) and 4.9 minutes (for 0.25 $\frac{1}{\text{min}}$) (see calculations in the appendix) (Steffensen 1989). These calculations were then applied to the parameters of the experiments, resulting in theoretical values used as orientation for the correction of the oxygen consumption time lag in relation to the heart rate (**Tab. 5**). Finally, time corrections were done operator mediated by matching maxima and minima of oxygen consumption to those of heart rates for each experiment at 12°C, representing control conditions.

Tables

Tab. 5: Respirometry parameters. The table includes the calculated respirometry parameters dilution factor Ḋ, the theoretical time point of 70% volume transformation and the effectively applied correction for the time lag of the oxygen consumption signal as related to the heart rate signal at 12°C.

Animal and condition	Dilution factor Ḋ ($\frac{1}{\text{min}}$)	Time point of 70% volume transformation (min)	Subtracted time lag (min)
Cancer 1 normocapnia	0.263	4.58	2
Cancer1 hypercapnia	0.263	4.58	2
Cancer 4 normocapnia	0.303	3.97	2
Cancer 4 hypercapnia	0.263	4.58	3
Cancer 5 normocapnia	0.263	4.58	2
Cancer 5 hypercapnia	0.270	4.46	3

Tab. 6: Parameters for transformations of pH measured in NBS scale to pH in free scale. The transformation was conducted using corrections for temperature, ion strength and a reference buffer-pH in artificial sea water after Waters and Millero (2013) and Dickson (2010).

Treatment	Temperature (°C)	Temperature (K)	Salinity (PSU)	pH (NBS scale)	pH Dickson buffer (NBS scale)
Normocapnia	11.6 ± 0.16	284.75 ± 0.16	33.33 ± 0.17	8.16 ± 0.04	8.67 ± 0.04
Hypercapnia	11.57 ± 0.52	284.72 ± 0.52	33.7 ± 0.14	7.68 ± 0.01	8.63 ± 0.02

Tab. 7: Sea water parameters resulted from checking prior to experiments before and after test runs of the temperature ramp under normocapnic conditions (n=3).

Temperature ramp	Temperature (°C)	Salinity (PSU)	pH (free scale)	$P(CO_2)_w$ (µatm)	$[HCO_3^-]_w$ (µmol/kg SW)	DIC (µmol/kg SW)
Start	12.066 ± 0.12	33.5 ± 0.08	8.1 ± 0.02	483.33 ± 17	2233.17 ± 146	2407.52 ± 163
Finish	20.03 ± 0.05	33.57 ± 0.09	8.17 ± 0.03	458.33 ± 27.18	2262.8 ± 109.16	2515.21 ± 128

Tab. 8: Sea water parameters resulted from checking prior to experiments before and after test runs of the temperature ramp under hypercapnic conditions (n=3).

Temperature ramp	Temperature (°C)	Salinity (PSU)	pH (free scale)	$P(CO_2)_w$ (µatm)	$[HCO_3^-]_w$ (µmol/kg SW)	DIC (µmol/kg SW)
Start	12.066 ± 0.17	33.7 ± 0.14	7.64 ± 0.02	1375 ± 10.8	2205.56 ± 80.25	2315 ± 34
Finish	19.97 ± 0.12	33.78 ± 0.12	7.71 ± 0.02	1324 ± 11.78	2276.22 ± 111.57	2402.55 ± 120

Tab. 9: Customized parameters of heart rate detection within LabChart added to the finger pulse basic fit.

Animal	Smoothing (ms)	Noise (V)	Minimum peak height (S.D)	Trigger
Cancer 1	-	0.015	3.43	Maximum
Cancer 4	100	0.026	2.6	Maximum
Cancer 5	100	0.018	1.503	Maximum

Tab. 10: Results of Levene´s Test for equal variances conducted for each parameter in Cancer 1 for each temperature step under both conditions. FDR-adjusted *p*-values (Benjamini and Hochberg 1995) are shown. Confidence interval was accounted for 95%. Significance declines the null hypothesis of equal variances. Non-significant combinations are marked as bold.

Parameter	12°C	14°C	16°C	18°C	20°C
Oxygen consumption	1.01E-09	1.42E-07	2.71E-02	2.71E-02	3.20E-09
Heart rate	5.70E-06	3.86E-03	2.16E-04	**6.59E-02**	**1.40E-01**
Integral proxy	1.43E-04	3.22E-05	**5.84E-01**	4.54E-03	2.44E-06
Cardiac output proxy	1.77E-02	**4.22E-01**	**4.22E-01**	**4.22E-01**	1.90E-21

Tab. 11: Results of Shapiro-Wilk-Test for normal distribution conducted for each parameter in Cancer 1 for each temperature step under both conditions. FDR-adjusted *p*-values (Benjamini and Hochberg 1995) are shown. Confidence interval was accounted for 95%. Significance declines the null hypothesis of normal distribution. Non-significant combinations are marked as bold.

Parameter	12°C	14°C	16°C	18°C	20°C
Oxygen consumption	3.23E-14	2.08E-08	1.12E-17	3.20E-12	6.13E-12
Heart rate	1.28E-21	3.95E-10	2.87E-18	2.64E-16	1.64E-10
Integral proxy	1.45E-04	4.64E-07	1.89E-10	4.27E-05	8.90E-09
Cardiac output proxy	2.93E-25	3.05E-15	1.37E-20	1.97E-14	2.12E-14

Tab. 12: Results of Levene´s Test for equal variances conducted for each parameter in Cancer 4 for each temperature step under both conditions. FDR-adjusted *p*-values (Benjamini and Hochberg 1995) are shown. Confidence interval was accounted for 95%. Significance declines the null hypothesis of equal variances. Non-significant combinations are marked as bold.

Parameter	12°C	14°C	16°C	18°C	20°C
Oxygen consumption	4.69E-25	5.23E-03	**1.08E-01**	8.25E-21	5.38E-11
Heart rate	4.07E-10	5.48E-17	5.25E-42	6.84E-82	**2.11E-01**
Integral proxy	**4.61E-01**	1.15E-13	3.29E-18	7.98E-41	**5.21E-01**
Cardiac output proxy	4.51E-23	3.26E-08	8.79E-13	3.31E-35	3.31E-35

Tab. 13: Results of Shapiro-Wilk-Test for normal distribution conducted for each parameter in Cancer 4 for each temperature step under both conditions. FDR-adjusted *p*-values (Benjamini and Hochberg 1995) are shown. Confidence interval was accounted for 95%. Significance declines the null hypothesis of normal distribution. Non-significant combinations are marked as bold.

Parameter	12°C	14°C	16°C	18°C	20°C
Oxygen consumption	1.61E-17	1.61E-17	8.41E-08	1.49E-04	8.23E-23
Heart rate	2.55E-26	5.13E-35	1.13E-19	2.50E-17	9.46E-10
Integral proxy	7.46E-05	8.48E-16	5.20E-11	6.71E-10	1.62E-04
Cardiac output proxy	2.43E-25	9.16E-20	9.16E-20	6.54E-10	5.86E-32

Tab. 14: Results of Levene´s Test for equal variances conducted for each parameter in Cancer 5 for each temperature step under both conditions. FDR-adjusted *p*-values (Benjamini and Hochberg 1995) are shown. Confidence interval was accounted for 95%. Significance declines the null hypothesis of equal variances. Non-significant combinations are marked as bold.

Parameter	12°C	14°C	16°C	18°C	20°C
Oxygen consumption	4.35E-07	1.36E-10	5.41E-30	6.65E-12	3.67E-81
Heart rate	**8.78E-01**	**2.16E-01**	4.62E-02	**2.16E-01**	3.89E-02
Integral proxy	9.33E-04	1.53E-17	3.69E-07	9.41E-05	3.14E-03
Cardiac output proxy	1.16E-05	9.22E-04	1.77E-02	**7.75E-01**	1.05E-25

Tab. 15: Results of Shapiro-Wilk-Test for normal distribution conducted for each parameter in Cancer 5 for each temperature step under both conditions. FDR-adjusted *p*-values (Benjamini and Hochberg 1995) are shown. Confidence interval was accounted for 95%. Significance declines the null hypothesis of normal distribution. Non-significant combinations are marked as bold.

Parameter	12°C	14°C	16°C	18°C	20°C
Oxygen consumption	4.96E-15	2.18E-14	1.54E-13	9.82E-10	2.09E-17
Heart rate	2.65E-18	1.02E-18	1.08E-09	4.92E-11	8.86E-13
Integral proxy	7.49E-05	5.47E-09	6.99E-07	1.43E-11	1.43E-11
Cardiac output proxy	1.89E-17	8.73E-19	1.32E-08	6.89E-10	6.77E-14

Tab. 16: Results of Levene´s Test for equal variances conducted for each parameter including values of all animals for each temperature step under both conditions (n=3). FDR-adjusted *p*-values (Benjamini and Hochberg 1995) are shown. Confidence interval was accounted for 95%. Significance declines the null hypothesis of equal variances. Non-significant combinations are marked as bold.

Parameter	12°C	14°C	16°C	18°C	20°C
Oxygen consumption	3.63E-26	2.49E-08	5.03E-03	**1.00E+00**	**1.00E+00**
Heart rate	1.01E-88	1.57E-02	2.97E-18	4.38E-13	**3.48E-01**
Integral proxy	**1.57E-01**	7.55E-07	5.85E-04	2.14E-09	3.73E-59
Cardiac output proxy	1.40E-08	2.03E-132	2.59E-05	3.95E-05	1.50E-39

Tab. 17: Results of Shapiro-Wilk-Test for normal distribution conducted for each parameter including values of all animals for each temperature step under both conditions (n=3). FDR-adjusted *p*-values (Benjamini and Hochberg 1995) are shown. Confidence interval was accounted for 95%. Significance declines the null hypothesis of normal distribution. Non-significant combinations are marked as bold.

Parameter	12°C	14°C	16°C	18°C	20°C
Oxygen consumption	1.54E-30	7.88E-23	1.13E-21	1.41E-15	5.21E-31
Heart rate	1.86E-36	6.93E-33	4.53E-28	9.95E-23	2.32E-20
Integral proxy	3.10E-05	8.83E-14	3.79E-14	8.49E-11	2.08E-29
Cardiac output proxy	3.96E-38	1.29E-27	3.08E-34	2.03E-28	1.98E-41

Tab. 18: Results of the Wilcoxon-signed-rank tests for the oxygen consumption measurements of Cancer 1 between different temperatures and treatments. FDR-adjusted *p*-values (Benjamini and Hochberg 1995) are shown. "N" indicates measurement under normocapnic conditions, whereas "H" indicates measurement under hypercapnic conditions. Confidence interval accounted for 95%. Non-significant combinations are marked as bold.

	N 14°C	N 16°C	N 18°C	N 20°C	H 12°C	H 14°C	H 16°C	H 18°C	H 20°C
N 12°C	7.52E-03	1.50E-15	2.02E-20	2.05E-30	1.25E-04	2.74E-02	**1.00E+00**	5.16E-06	8.95E-10
N 14°C	0	1.43E-02	1.68E-11	8.62E-03	**6.08E-01**	2.03E-10	**4.13E-01**	**8.92E-01**	**1.00E+00**
N 16°C	0	0	**8.96E-01**	**5.57E-01**	1.70E-05	4.19E-12	1.60E-14	2.81E-03	8.27E-05
N 18°C	0	0	0	**1.00E+00**	2.33E-15	3.26E-19	2.46E-16	2.63E-06	1.31E-08
N 20°C	0	0	0	0	4.78E-13	2.06E-17	8.84E-24	3.89E-07	5.08E-15
H 12°C	0	0	0	0	0	5.11E-03	1.07E-02	**1.16E-01**	**1.00E+00**
H 14°C	0	0	0	0	0	0	**6.31E-02**	9.87E-05	1.78E-07
H 16°C	0	0	0	0	0	0	0	3.70E-04	3.71E-06
H 18°C	0	0	0	0	0	0	0	0	**1.00E+00**

Tab. 19: Results of the Wilcoxon-signed-rank tests for the heart rate measurements of Cancer 1 between different temperatures and treatments. FDR-adjusted *p*-values (Benjamini and Hochberg 1995) are shown. "N" indicates measurement under normocapnic conditions, whereas "H" indicates measurement under hypercapnic conditions. Confidence interval accounted for 95%. Non-significant combinations are marked as bold.

	N 14°C	N 16°C	N 18°C	N 20°C	H 12°C	H 14°C	H 16°C	H 18°C	H 20°C
N 12°C	**3.59E-01**	3.40E-15	2.95E-17	2.00E-29	9.69E-05	**1.00E+00**	1.97E-04	3.97E-20	7.24E-35
N 14°C	0	2.45E-04	5.60E-11	6.27E-04	2.66E-06	3.44E-04	**1.00E+00**	**7.11E-02**	6.91E-07
N 16°C	0	0	**9.78E-01**	**1.18E-01**	2.44E-21	4.44E-09	1.46E-03	**7.51E-02**	3.34E-04
N 18°C	0	0	0	**1.00E+00**	1.30E-27	3.48E-17	5.24E-07	**1.00E+00**	**1.00E+00**
N 20°C	0	0	0	0	7.44E-40	7.95E-14	3.25E-11	**1.00E+00**	**1.00E+00**
H 12°C	0	0	0	0	0	7.36E-03	7.80E-12	1.21E-28	1.13E-40
H 14°C	0	0	0	0	0	0	1.75E-03	2.27E-07	1.98E-12
H 16°C	0	0	0	0	0	0	0	4.20E-07	2.17E-14
H 18°C	0	0	0	0	0	0	0	0	**1.00E+00**

Tab. 20: Results of the Wilcoxon-signed-rank tests for the integral proxy measurements of Cancer 1 between different temperatures and treatments. FDR-adjusted *p*-values (Benjamini and Hochberg 1995) are shown. "N" indicates measurement under normocapnic conditions, whereas "H" indicates measurement under hypercapnic conditions. Confidence interval accounted for 95%. Non-significant combinations are marked as bold.

	N 14°C	N 16°C	N 18°C	N 20°C	H 12°C	H 14°C	H 16°C	H 18°C	H 20°C
N 12°C	3.88E-02	1.48E-29	4.56E-33	1.05E-46	**1.00E+00**	6.48E-03	3.46E-36	6.30E-39	1.12E-48
N 14°C	0	1.57E-15	4.68E-16	8.66E-18	9.64E-04	**1.00E+00**	1.44E-11	1.60E-18	2.47E-19
N 16°C	0	0	1.03E-03	2.55E-28	2.81E-29	4.69E-10	**1.00E+00**	5.86E-08	3.86E-43
N 18°C	0	0	0	2.03E-13	3.52E-33	8.74E-13	1.01E-02	**1.00E+00**	4.48E-35
N 20°C	0	0	0	0	6.52E-47	3.02E-16	1.33E-27	2.84E-11	4.13E-28
H 12°C	0	0	0	0	0	7.88E-04	1.39E-34	1.22E-39	1.01E-48
H 14°C	0	0	0	0	0	0	7.49E-06	4.41E-13	1.19E-18
H 16°C	0	0	0	0	0	0	0	3.72E-06	1.79E-42
H 18°C	0	0	0	0	0	0	0	0	2.96E-33

Tab. 21: Results of the Wilcoxon-signed-rank tests for the cardiac output proxy calculations of Cancer 1 between different temperatures and treatments. FDR-adjusted *p*-values (Benjamini and Hochberg 1995) are shown. "N" indicates measurement under normocapnic conditions, whereas "H" indicates measurement under hypercapnic conditions. Confidence interval accounted for 95%. Non-significant combinations are marked as bold.

	N 14°C	**N 16°C**	**N 18°C**	**N 20°C**	**H 12°C**	**H 14°C**	**H 16°C**	**H 18°C**	**H 20°C**
N 12°C	1.70E-02	9.39E-24	5.13E-25	3.34E-43	**1.00E+00**	**1.00E+00**	7.09E-21	1.38E-33	4.77E-47
N 14°C	0	5.47E-09	5.17E-15	1.16E-11	2.11E-04	**1.00E+00**	1.00E-04	2.74E-10	2.32E-18
N 16°C	0	0	4.40E-03	7.51E-11	6.19E-21	8.33E-08	**1.00E+00**	5.61E-13	1.40E-33
N 18°C	0	0	0	**8.32E-01**	1.28E-26	5.14E-16	4.82E-04	**1.31E-01**	9.37E-23
N 20°C	0	0	0	0	4.82E-43	4.84E-15	1.16E-11	**1.00E+00**	1.19E-22
H 12°C	0	0	0	0	0	5.82E-03	7.11E-18	2.36E-34	4.32E-47
H 14°C	0	0	0	0	0	0	1.70E-05	1.07E-09	9.31E-18
H 16°C	0	0	0	0	0	0	0	7.29E-10	9.28E-34
H 18°C	0	0	0	0	0	0	0	0	1.52E-18

Tab. 22: Results of the Wilcoxon-signed-rank tests for the oxygen consumption measurements of Cancer 4 between different temperatures and treatments. FDR-adjusted *p*-values (Benjamini and Hochberg 1995) are shown. "N" indicates measurement under normocapnic conditions, whereas "H" indicates measurement under hypercapnic conditions. Confidence interval accounted for 95%. Non-significant combinations are marked as bold.

	N 14°C	**N 16°C**	**N 18°C**	**N 20°C**	**H 12°C**	**H 14°C**	**H 16°C**	**H 18°C**	**H 20°C**
N 12°C	5.46E-10	1.29E-20	9.05E-04	3.11E-05	2.10E-29	2.15E-35	1.36E-10	**1.00E+00**	**1.00E+00**
N 14°C	0	2.83E-39	1.59E-23	2.77E-30	8.96E-42	1.45E-21	3.27E-32	5.71E-23	1.34E-18
N 16°C	0	0	**1.00E+00**	3.45E-12	1.70E-05	1.52E-48	3.85E-04	6.32E-14	1.86E-17
N 18°C	0	0	0	5.34E-03	1.42E-06	1.06E-35	**1.00E+00**	1.96E-04	**1.00E+00**
N 20°C	0	0	0	0	5.15E-32	4.36E-49	4.52E-03	**1.00E+00**	9.38E-02
H 12°C	0	0	0	0	0	2.78E-49	7.90E-19	4.98E-24	2.42E-40
H 14°C	0	0	0	0	0	0	6.30E-49	1.06E-35	5.27E-32
H 16°C	0	0	0	0	0	0	0	3.51E-02	1.01E-05
H 18°C	0	0	0	0	0	0	0	0	1.12E-02

Tab. 23: Results of the Wilcoxon-signed-rank tests for the heart rate measurements of Cancer 4 between different temperatures and treatments. FDR-adjusted *p*-values (Benjamini and Hochberg 1995) are shown. "N" indicates measurement under normocapnic conditions, whereas "H" indicates measurement under hypercapnic conditions. Confidence interval accounted for 95%. Non-significant combinations are marked as bold.

	N 14°C	N 16°C	N 18°C	N 20°C	H 12°C	H 14°C	H 16°C	H 18°C	H 20°C
N 12°C	1.03E-16	3.80E-02	**1.00E+00**	**1.00E+00**	3.57E-36	2.56E-40	8.21E-30	4.22E-20	8.56E-09
N 14°C	0	1.67E-13	2.52E-04	1.47E-10	5.84E-44	1.83E-08	5.12E-39	4.13E-32	1.85E-24
N 16°C	0	0	**1.00E+00**	1.19E-02	3.26E-18	3.60E-29	1.23E-10	8.71E-11	**1.00E+00**
N 18°C	0	0	0	**1.00E+00**	1.71E-14	4.15E-12	2.45E-10	7.81E-11	2.30E-07
N 20°C	0	0	0	0	8.73E-41	9.42E-30	2.33E-36	2.80E-25	3.71E-08
H 12°C	0	0	0	0	0	2.92E-49	1.31E-03	4.43E-07	3.02E-31
H 14°C	0	0	0	0	0	0	4.52E-49	1.06E-35	1.27E-37
H 16°C	0	0	0	0	0	0	0	**1.00E+00**	1.67E-13
H 18°C	0	0	0	0	0	0	0	0	7.90E-03

Tab. 24: Results of the Wilcoxon-signed-rank tests for the integral measurements of Cancer 4 between different temperatures and treatments. FDR-adjusted *p*-values (Benjamini and Hochberg 1995) are shown. "N" indicates measurement under normocapnic conditions, whereas "H" indicates measurement under hypercapnic conditions. Confidence interval accounted for 95%. Non-significant combinations are marked as bold.

	N 14°C	N 16°C	N 18°C	N 20°C	H 12°C	H 14°C	H 16°C	H 18°C	H 20°C
N 12°C	2.53E-25	1.65E-05	**1.00E+00**	2.26E-30	**1.00E+00**	2.80E-38	**1.00E+00**	3.92E-07	8.82E-14
N 14°C	0	5.22E-03	3.08E-06	1.03E-06	1.61E-27	**1.00E+00**	8.98E-21	2.31E-09	**1.00E+00**
N 16°C	0	0	**1.00E+00**	1.43E-09	3.32E-06	1.16E-02	9.64E-04	**1.00E+00**	**1.00E+00**
N 18°C	0	0	0	3.58E-12	**1.00E+00**	1.65E-04	**1.00E+00**	**1.00E+00**	**1.00E+00**
N 20°C	0	0	0	0	6.32E-30	2.76E-09	3.65E-29	3.27E-14	2.04E-08
H 12°C	0	0	0	0	0	7.09E-35	**1.00E+00**	2.07E-08	9.01E-14
H 14°C	0	0	0	0	0	0	5.55E-29	9.69E-14	**7.41E-01**
H 16°C	0	0	0	0	0	0	0	2.88E-05	4.36E-11
H 18°C	0	0	0	0	0	0	0	0	**6.19E-01**

Tab. 25: Results of the Wilcoxon-signed-rank tests for the cardiac output calculations of Cancer 4 between different temperatures and treatments. FDR-adjusted *p*-values (Benjamini and Hochberg 1995) are shown. "N" indicates measurement under normocapnic conditions, whereas "H" indicates measurement under hypercapnic conditions. Confidence interval accounted for 95%. Non-significant combinations are marked as bold.

	N 14°C	N 16°C	N 18°C	N 20°C	H 12°C	H 14°C	H 16°C	H 18°C	H 20°C
N 12°C	7.73E-21	**1.00E+00**	**1.00E+00**	1.73E-10	1.92E-02	2.75E-49	1.37E-02	1.70E-07	7.83E-34
N 14°C	0	2.31E-11	3.54E-04	**2.18E-01**	1.16E-14	2.75E-49	**4.18E-01**	2.57E-04	8.58E-05
N 16°C	0	0	**1.00E+00**	1.88E-04	**1.00E+00**	4.01E-49	**8.73E-02**	6.82E-04	1.51E-23
N 18°C	0	0	0	**1.38E-01**	**5.02E-01**	1.06E-35	**1.00E+00**	**1.00E+00**	2.34E-03
N 20°C	0	0	0	0	5.76E-08	2.75E-49	**1.00E+00**	**1.00E+00**	8.05E-11
H 12°C	0	0	0	0	0	4.23E-49	1.16E-03	1.25E-05	5.09E-26
H 14°C	0	0	0	0	0	0	3.97E-48	1.06E-35	9.91E-21
H 16°C	0	0	0	0	0	0	0	**1.00E+00**	6.06E-11
H 18°C	0	0	0	0	0	0	0	0	3.18E-02

Tab. 26: Results of the Wilcoxon-signed-rank tests for the oxygen consumption measurements of Cancer 5 between different temperatures and treatments. FDR-adjusted *p*-values (Benjamini and Hochberg 1995) are shown. "N" indicates measurement under normocapnic conditions, whereas "H" indicates measurement under hypercapnic conditions. Confidence interval accounted for 95%. Non-significant combinations are marked as bold.

	N 14°C	N 16°C	N 18°C	N 20°C	H 12°C	H 14°C	H 16°C	H 18°C	H 20°C
N 12°C	7.24E-12	2.79E-23	6.09E-35	4.71E-48	6.83E-15	9.74E-21	8.73E-28	5.85E-39	3.26E-49
N 14°C	0	3.63E-11	4.18E-20	5.50E-29	**1.00E+00**	5.16E-08	7.53E-26	5.69E-35	9.20E-35
N 16°C	0	0	6.60E-04	1.81E-06	2.02E-08	**1.00E+00**	8.03E-18	9.84E-27	7.76E-26
N 18°C	0	0	0	5.09E-07	3.01E-21	**1.00E+00**	3.27E-13	4.27E-32	7.87E-29
N 20°C	0	0	0	0	1.03E-41	1.08E-06	1.14E-06	1.17E-02	2.14E-02
H 12°C	0	0	0	0	0	1.09E-07	2.63E-25	9.02E-38	7.77E-47
H 14°C	0	0	0	0	0	0	3.61E-14	4.50E-25	4.47E-21
H 16°C	0	0	0	0	0	0	0	**1.00E+00**	**1.00E+00**
H 18°C	0	0	0	0	0	0	0	0	2.06E-02

Tab. 27: Results of the Wilcoxon-signed-rank tests for the heart rate measurements of Cancer 5 between different temperatures and treatments. FDR-adjusted *p*-values (Benjamini and Hochberg 1995) are shown. "N" indicates measurement under normocapnic conditions, whereas "H" indicates measurement under hypercapnic conditions. Confidence interval accounted for 95%. Non-significant combinations are marked as bold.

	N 14°C	N 16°C	N 18°C	N 20°C	H 12°C	H 14°C	H 16°C	H 18°C	H 20°C
N 12°C	5.87E-06	8.51E-30	5.64E-39	2.75E-49	**1.00E+00**	**1.00E+00**	9.03E-13	4.76E-10	3.64E-27
N 14°C	0	8.51E-30	2.35E-36	2.35E-36	**1.00E+00**	**1.00E+00**	6.78E-12	1.53E-05	4.31E-16
N 16°C	0	0	6.08E-20	2.31E-16	3.47E-06	**1.46E-01**	**1.00E+00**	**1.00E+00**	2.28E-06
N 18°C	0	0	0	5.64E-39	6.03E-15	1.43E-04	**7.47E-02**	**1.00E+00**	1.81E-02
N 20°C	0	0	0	0	1.44E-38	1.01E-13	**1.00E+00**	5.02E-04	1.07E-04
H 12°C	0	0	0	0	0	**6.59E-01**	2.58E-09	8.46E-10	2.69E-26
H 14°C	0	0	0	0	0	0	9.00E-06	3.23E-05	9.00E-16
H 16°C	0	0	0	0	0	0	0	**1.00E+00**	2.24E-02
H 18°C	0	0	0	0	0	0	0	0	3.80E-03

Tab. 28: Results of the Wilcoxon-signed-rank tests for the integral measurements of Cancer 5 between different temperatures and treatments. FDR-adjusted *p*-values (Benjamini and Hochberg 1995) are shown. "N" indicates measurement under normocapnic conditions, whereas "H" indicates measurement under hypercapnic conditions. Confidence interval accounted for 95%. Non-significant combinations are marked as bold.

	N 14°C	N 16°C	N 18°C	N 20°C	H 12°C	H 14°C	H 16°C	H 18°C	H 20°C
N 12°C	**8.55E-01**	4.66E-12	6.92E-25	1.13E-32	**1.00E+00**	**1.00E+00**	2.48E-07	1.18E-11	3.14E-26
N 14°C	0	4.00E-06	8.47E-12	1.46E-12	**9.30E-01**	6.66E-03	1.13E-03	1.12E-03	1.33E-09
N 16°C	0	0	2.36E-02	**5.41E-02**	2.14E-11	2.94E-13	**1.00E+00**	**1.00E+00**	**1.51E-01**
N 18°C	0	0	0	**4.66E-01**	8.86E-22	2.46E-21	**5.09E-02**	5.46E-03	**1.00E+00**
N 20°C	0	0	0	0	3.43E-38	4.70E-24	4.63E-05	1.32E-09	4.05E-08
H 12°C	0	0	0	0	0	**1.00E+00**	3.46E-08	3.40E-12	2.13E-25
H 14°C	0	0	0	0	0	0	5.86E-14	2.03E-17	2.49E-24
H 16°C	0	0	0	0	0	0	0	**1.00E+00**	3.24E-06
H 18°C	0	0	0	0	0	0	0	0	4.31E-04

Tab. 29: Results of the Wilcoxon-signed-rank tests for the cardiac output proxy calculations of Cancer 5 between different temperatures and treatments. FDR-adjusted *p*-values (Benjamini and Hochberg 1995) are shown. "N" indicates measurement under normocapnic conditions, whereas "H" indicates measurement under hypercapnic conditions. Confidence interval accounted for 95%. Non-significant combinations are marked as bold.

	N 14°C	**N 16°C**	**N 18°C**	**N 20°C**	**H 12°C**	**H 14°C**	**H 16°C**	**H 18°C**	**H 20°C**
N 12°C	1.18E-03	3.06E-28	6.47E-36	3.36E-48	**1.00E+00**	**1.00E+00**	1.38E-11	6.60E-11	4.16E-31
N 14°C	0	9.62E-28	4.51E-28	1.43E-34	**9.35E-02**	**1.00E+00**	3.86E-10	3.67E-06	6.53E-17
N 16°C	0	0	**1.00E+00**	6.50E-10	1.14E-11	5.73E-07	**1.00E+00**	**1.00E+00**	2.67E-08
N 18°C	0	0	0	2.60E-18	9.20E-23	4.39E-13	**1.00E+00**	**1.00E+00**	**1.56E-01**
N 20°C	0	0	0	0	8.94E-44	5.58E-23	**1.00E+00**	9.94E-06	1.83E-07
H 12°C	0	0	0	0	0	**1.00E+00**	1.24E-12	1.84E-15	3.33E-36
H 14°C	0	0	0	0	0	0	2.65E-10	1.50E-10	4.11E-23
H 16°C	0	0	0	0	0	0	0	**1.00E+00**	1.68E-05
H 18°C	0	0	0	0	0	0	0	0	3.00E-05

Tab. 30: Results of the Wilcoxon-signed-rank tests for the combined oxygen consumption measurements of all animals between different temperatures and treatments (n=3). FDR-adjusted *p*-values (Benjamini and Hochberg 1995) are shown. "N" indicates measurement under normocapnic conditions, whereas "H" indicates measurement under hypercapnic conditions. Confidence interval accounted for 95%. Non-significant combinations are marked as bold.

	N 14°C	**N 16°C**	**N 18°C**	**N 20°C**	**H 12°C**	**H 14°C**	**H 16°C**	**H 18°C**	**H 20°C**
N 12°C	1.90E-02	**1.00E+00**	**1.17E-01**	3.65E-28	1.96E-06	4.14E-11	**1.00E+00**	9.01E-11	3.65E-28
N 14°C	0	1.55E-10	**2.74E-01**	**1.00E+00**	4.95E-28	2.12E-10	2.42E-06	**1.00E+00**	**1.00E+00**
N 16°C	0	0	1.46E-04	1.83E-16	7.25E-13	4.25E-27	**1.00E+00**	5.57E-17	1.83E-16
N 18°C	0	0	0	1.20E-02	1.41E-30	1.91E-11	**1.96E-01**	4.81E-05	1.20E-02
N 20°C	0	0	0	0	2.23E-79	7.78E-09	5.75E-09	**1.00E+00**	**1.00E+00**
H 12°C	0	0	0	0	0	4.06E-48	1.65E-11	3.58E-42	2.23E-79
H 14°C	0	0	0	0	0	0	7.27E-19	1.45E-06	7.78E-09
H 16°C	0	0	0	0	0	0	0	7.03E-15	5.75E-09
H 18°C	0	0	0	0	0	0	0	0	**1.00E+00**

Tab. 31: Results of the Wilcoxon-signed-rank tests for the combined heart rate measurements of all animals between different temperatures and treatments (n=3). FDR-adjusted *p*-values (Benjamini and Hochberg 1995) are shown. "N" indicates measurement under normocapnic conditions, whereas "H" indicates measurement under hypercapnic conditions. Confidence interval accounted for 95%. Non-significant combinations are marked as bold.

	N 14°C	N 16°C	N 18°C	N 20°C	H 12°C	H 14°C	H 16°C	H 18°C	H 20°C
N 12°C	1.66E-03	1.73E-02	5.63E-07	5.91E-45	6.15E-36	1.76E-06	**9.96E-01**	1.39E-02	2.84E-17
N 14°C	0	1.25E-04	4.73E-02	**1.00E+00**	8.61E-56	**1.00E+00**	5.51E-16	3.44E-02	**1.00E+00**
N 16°C	0	0	7.97E-04	2.19E-04	6.50E-44	1.19E-08	3.55E-08	**5.34E-01**	1.07E-03
N 18°C	0	0	0	**1.00E+00**	7.10E-58	**1.95E-01**	1.65E-15	**6.51E-01**	**1.00E+00**
N 20°C	0	0	0	0	3.88E-113	**1.00E+00**	1.72E-30	4.62E-04	1.95E-05
H 12°C	0	0	0	0	0	2.05E-63	7.78E-26	5.12E-55	1.17E-89
H 14°C	0	0	0	0	0	0	1.37E-21	1.10E-04	**1.00E+00**
H 16°C	0	0	0	0	0	0	0	8.19E-10	1.34E-30
H 18°C	0	0	0	0	0	0	0	0	7.50E-03

Tab. 32: Results of the Wilcoxon-signed-rank tests for the combined integral measurements of all animals between different temperatures and treatments (n=3). FDR-adjusted *p*-values (Benjamini and Hochberg 1995) are shown. "N" indicates measurement under normocapnic conditions, whereas "H" indicates measurement under hypercapnic conditions. Confidence interval accounted for 95%. Non-significant combinations are marked as bold.

	N 14°C	N 16°C	N 18°C	N 20°C	H 12°C	H 14°C	H 16°C	H 18°C	H 20°C
N 12°C	2.08E-18	1.30E-41	2.17E-50	3.21E-110	**1.00E+00**	4.19E-15	1.19E-50	3.01E-77	6.94E-96
N 14°C	0	**1.63E-01**	1.77E-11	3.91E-56	9.84E-22	**1.00E+00**	5.76E-03	6.03E-20	5.30E-54
N 16°C	0	0	4.04E-02	5.48E-43	3.62E-39	1.14E-06	**1.00E+00**	4.94E-09	1.96E-45
N 18°C	0	0	0	2.15E-23	1.11E-44	5.85E-16	8.93E-06	**1.00E+00**	1.87E-38
N 20°C	0	0	0	0	7.27E-115	9.72E-67	1.24E-55	6.92E-18	2.82E-02
H 12°C	0	0	0	0	0	3.87E-20	2.69E-44	3.68E-72	4.07E-100
H 14°C	0	0	0	0	0	0	1.08E-08	7.02E-34	7.69E-61
H 16°C	0	0	0	0	0	0	0	4.70E-15	2.26E-59
H 18°C	0	0	0	0	0	0	0	0	2.01E-24

Tab. 33: Results of the Wilcoxon-signed-rank tests for the combined cardiac output calculations of all animals between different temperatures and treatments (n=3). FDR-adjusted *p*-values (Benjamini and Hochberg 1995) are shown. "N" indicates measurement under normocapnic conditions, whereas "H" indicates measurement under hypercapnic conditions. Confidence interval accounted for 95%. Non-significant combinations are marked as bold.

	N 14°C	N 16°C	N 18°C	N 20°C	H 12°C	H 14°C	H 16°C	H 18°C	H 20°C
N 12°C	9.06E-17	5.52E-27	8.02E-44	5.98E-104	**1.56E-01**	5.29E-55	1.65E-38	2.98E-63	1.31E-112
N 14°C	0	**7.14E-01**	2.14E-06	2.19E-27	1.92E-18	5.45E-36	1.18E-08	9.13E-35	1.34E-73
N 16°C	0	0	1.61E-13	5.01E-16	1.68E-23	3.24E-19	**2.82E-01**	9.92E-32	9.18E-59
N 18°C	0	0	0	**1.00E+00**	1.22E-40	3.47E-02	3.67E-02	1.63E-06	1.00E-37
N 20°C	0	0	0	0	1.59E-97	**1.00E+00**	3.56E-04	**6.36E-02**	1.08E-12
H 12°C	0	0	0	0	0	6.95E-57	3.04E-34	2.63E-57	8.89E-109
H 14°C	0	0	0	0	0	0	8.53E-07	**1.00E+00**	1.91E-26
H 16°C	0	0	0	0	0	0	0	8.74E-12	2.04E-47
H 18°C	0	0	0	0	0	0	0	0	2.92E-15

Figures

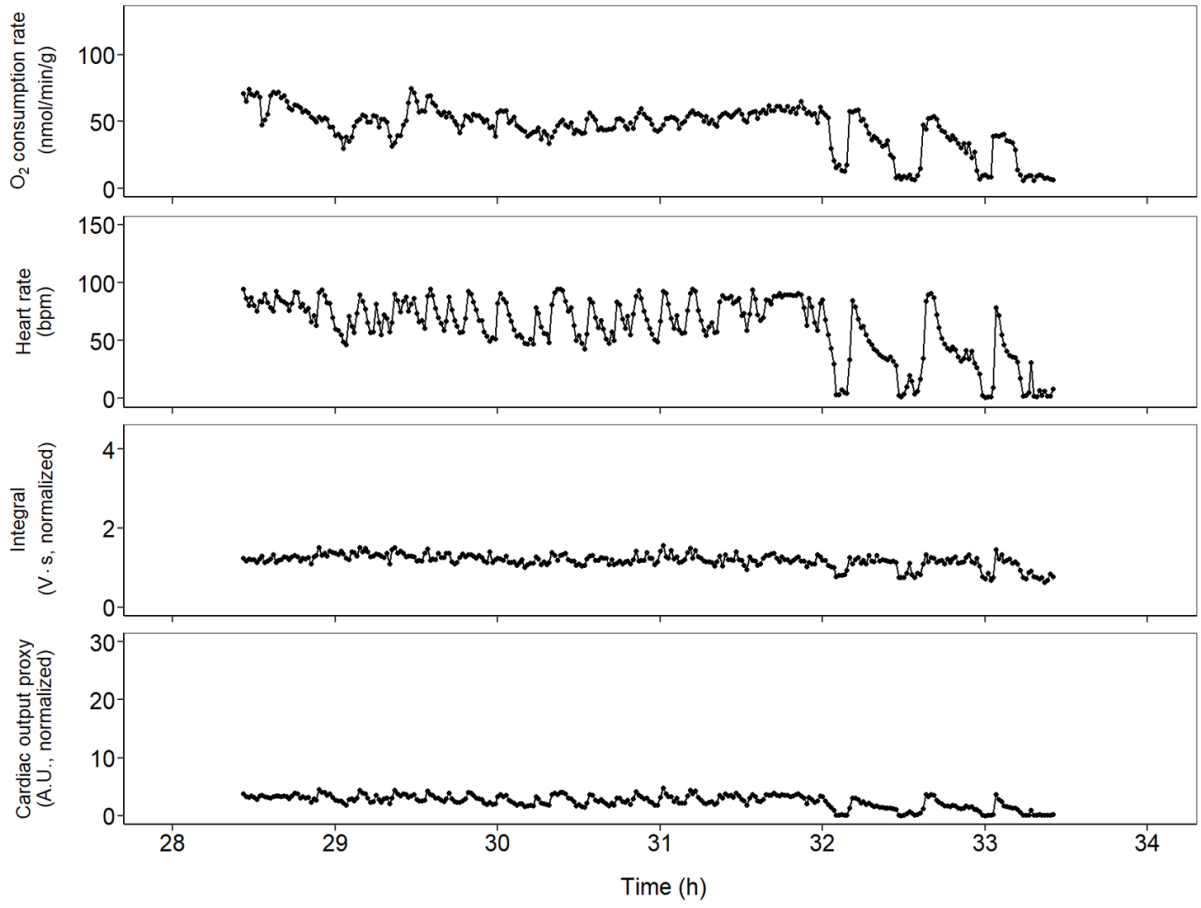

Fig. 39: Time course of cardiovascular parameters obtained for Cancer 1 at 14°C under normocapnic conditions.

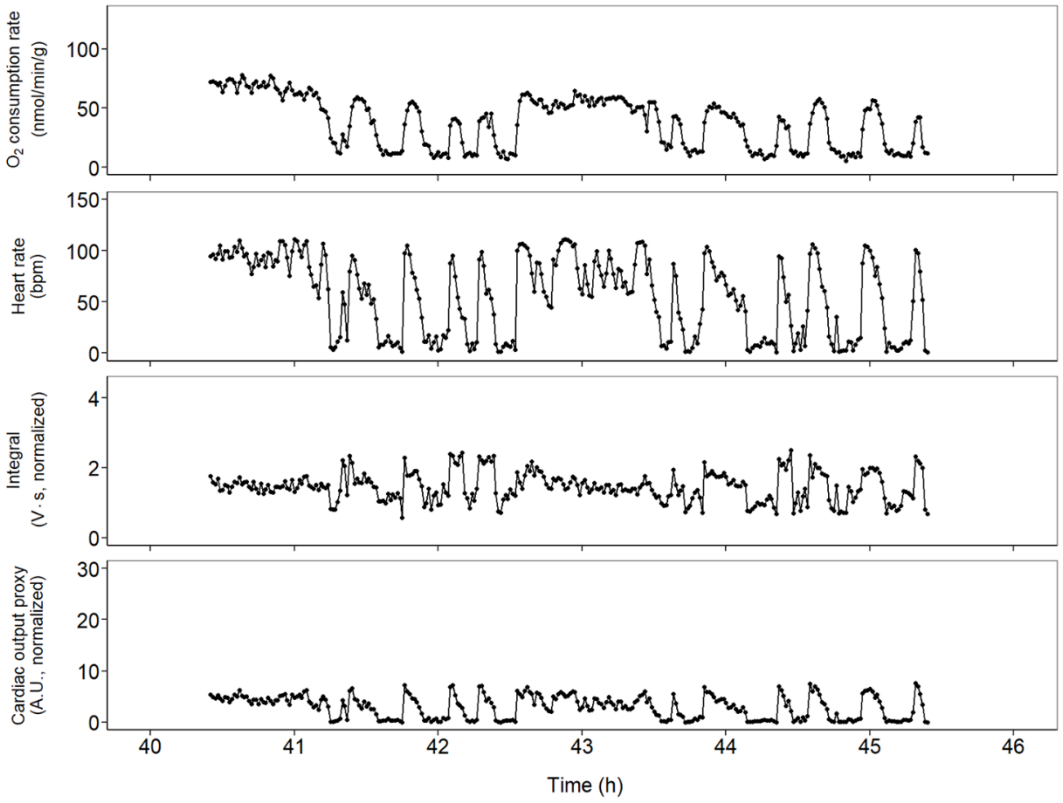

Fig. 40: Time course of cardiovascular parameters obtained for Cancer 1 at 16°C under normocapnic conditions.

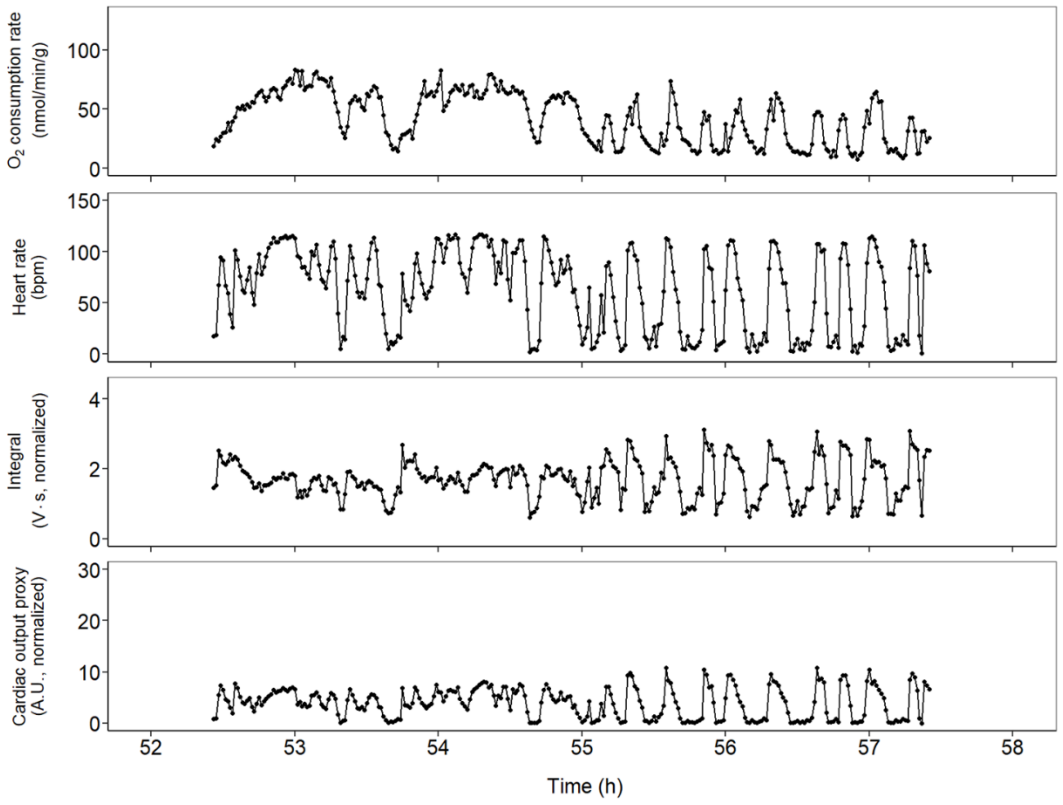

Fig. 41: Time course of cardiovascular parameters obtained for Cancer 1 at 18°C under normocapnic conditions.

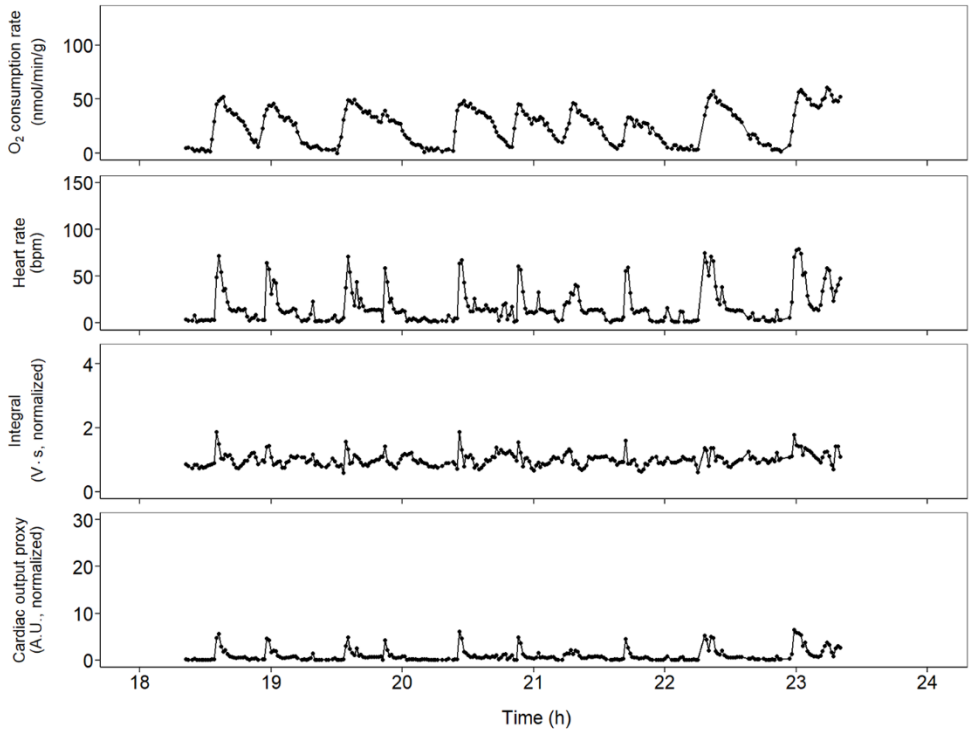

Fig. 42: Time course of cardiovascular parameters obtained for Cancer 1 at 12°C under hypercapnic conditions.

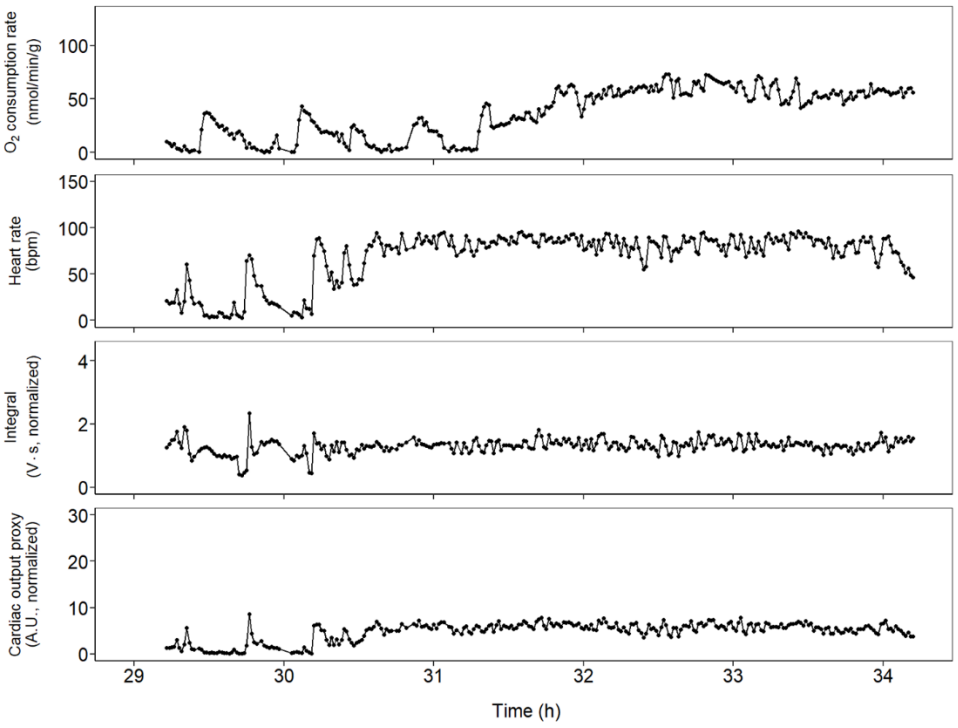

Fig. 43: Time course of cardiovascular parameters obtained for Cancer 1 at 14°C under hypercapnic conditions.

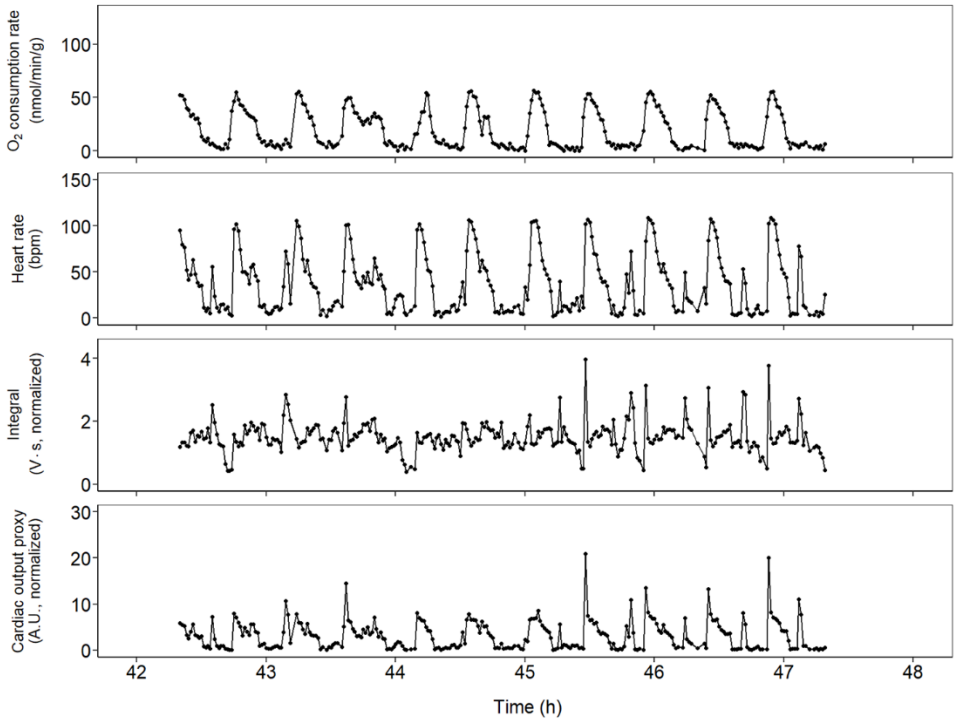

Fig. 44: Time course of cardiovascular parameters obtained for Cancer 1 at 16°C under hypercapnic conditions.

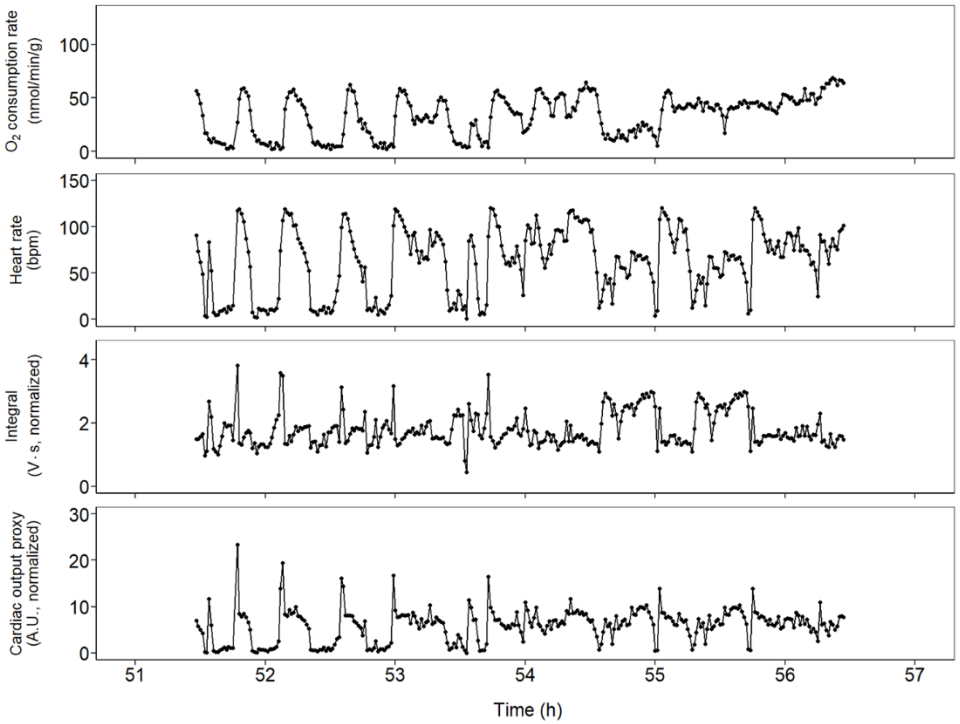

Fig. 45: Time course of cardiovascular parameters obtained for Cancer 1 at 18°C under hypercapnic conditions.

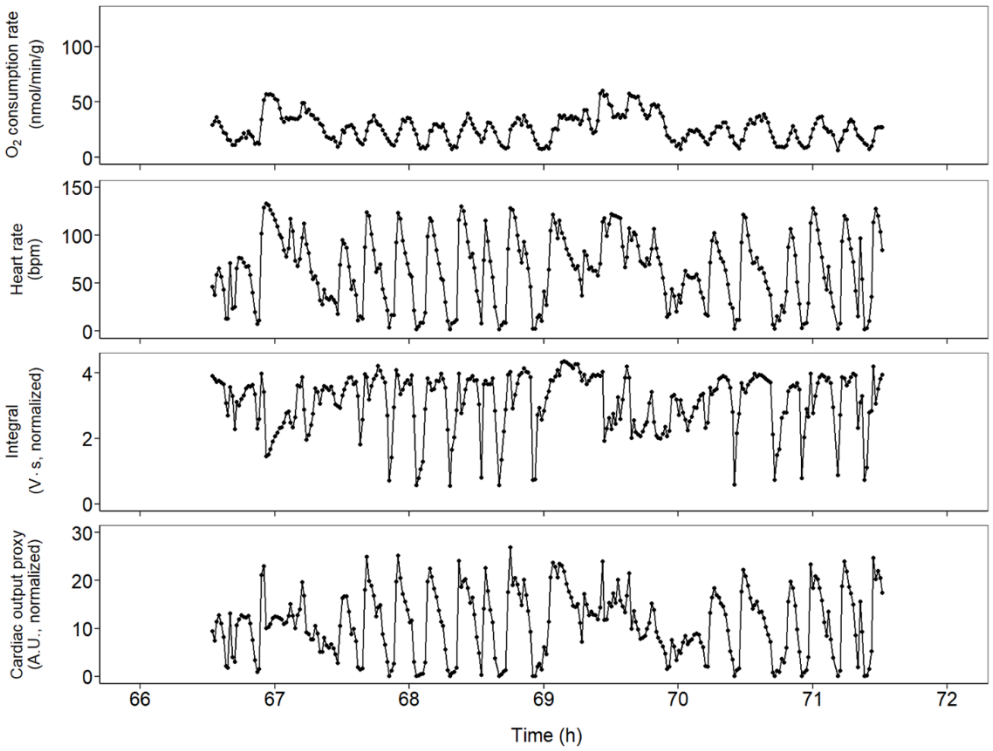

Fig. 46: Time course of cardiovascular parameters obtained for Cancer 1 at 20°C under hypercapnic conditions.

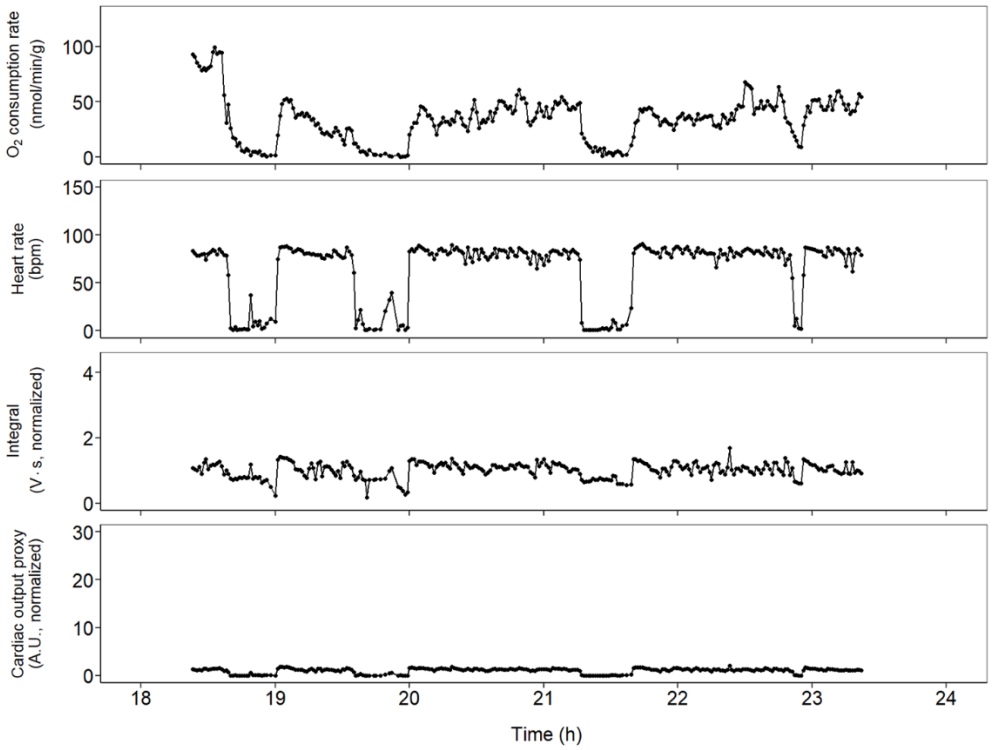

Fig. 47: Time course of cardiovascular parameters obtained for Cancer 4 at 12°C under normocapnic conditions.

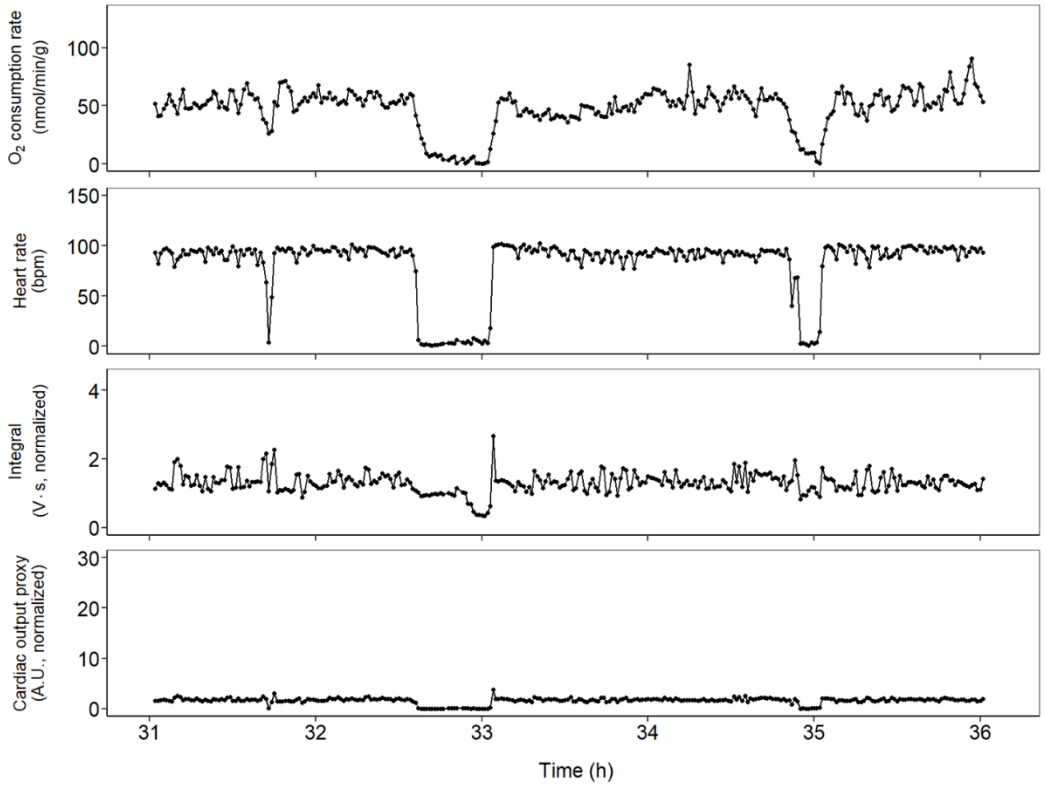

Fig. 48: Time course of cardiovascular parameters obtained for Cancer 4 at 14°C under normocapnic conditions.

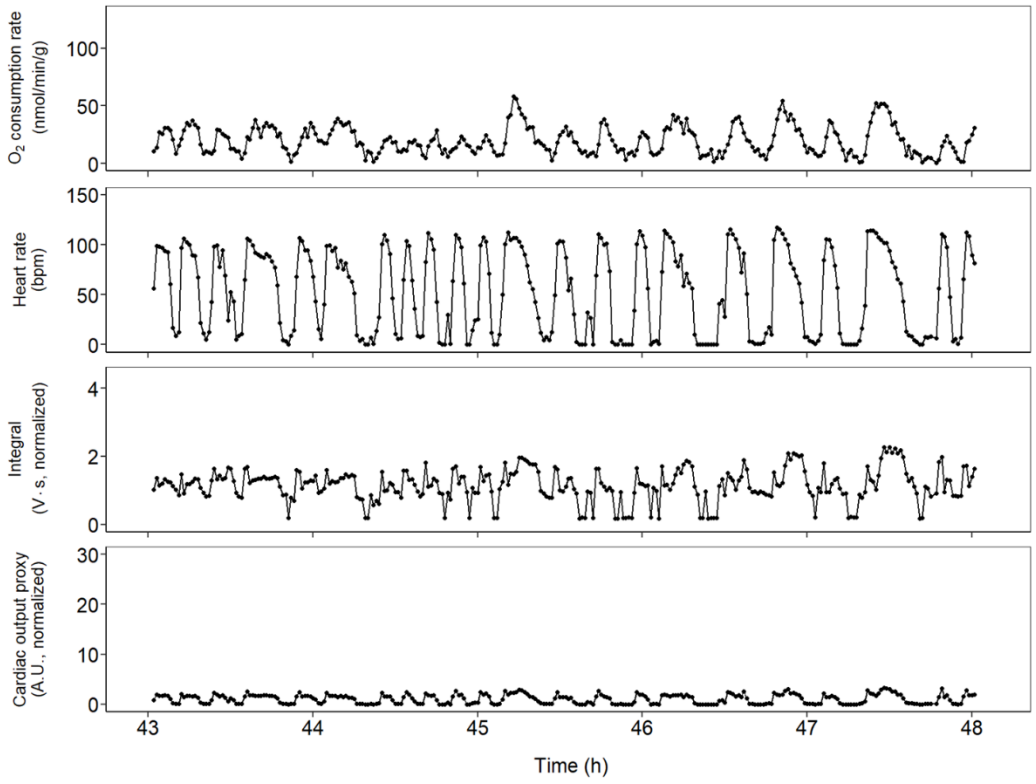

Fig. 49: Time course of cardiovascular parameters obtained for Cancer 4 at 16°C under normocapnic conditions.

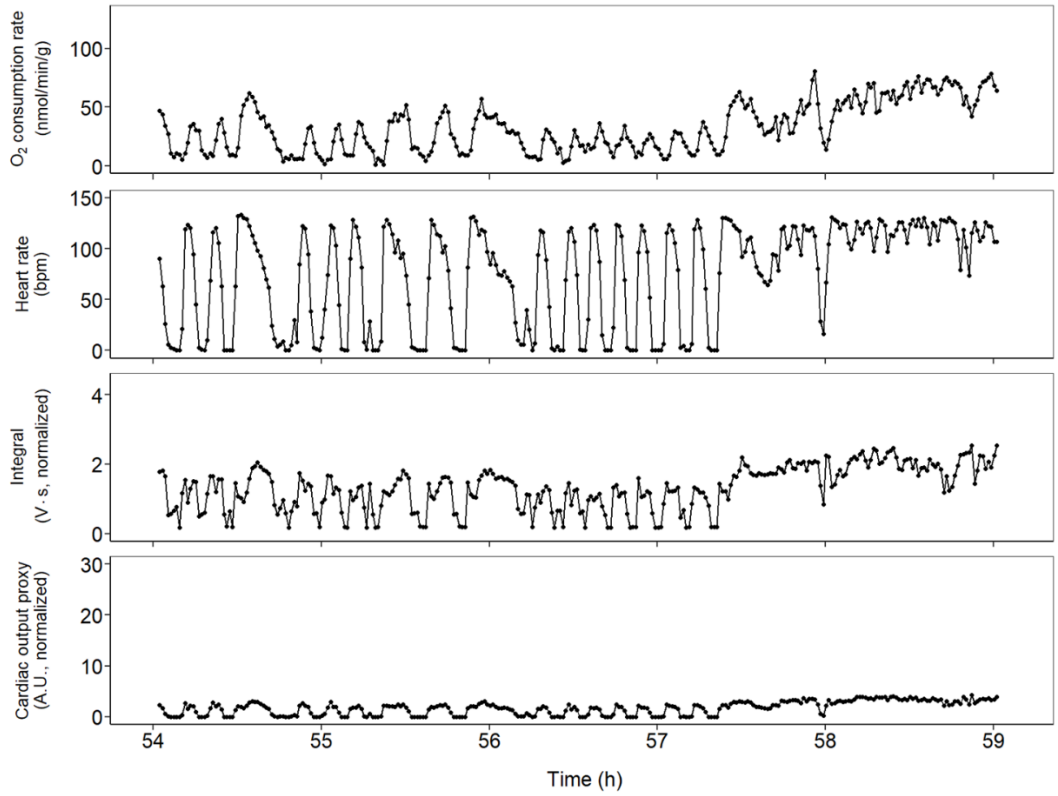

Fig. 50: Time course of cardiovascular parameters obtained for Cancer 4 at 18°C under normocapnic conditions.

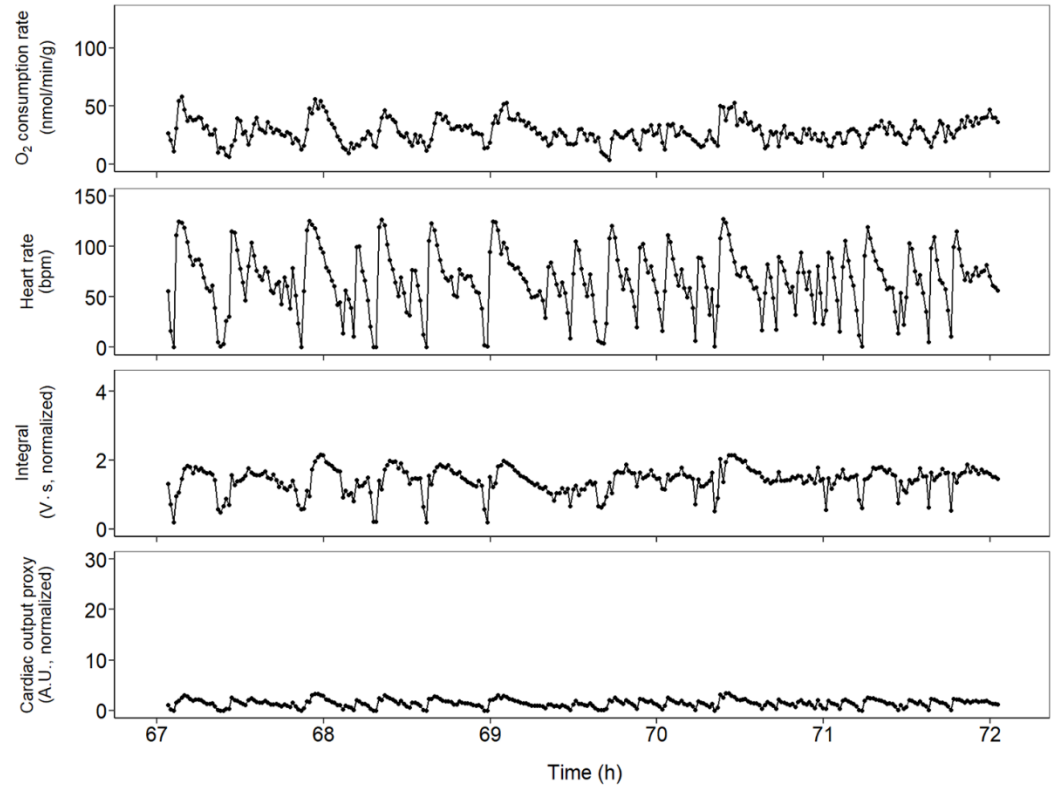

Fig. 51: Time course of cardiovascular parameters obtained for Cancer 4 at 20°C under normocapnic conditions.

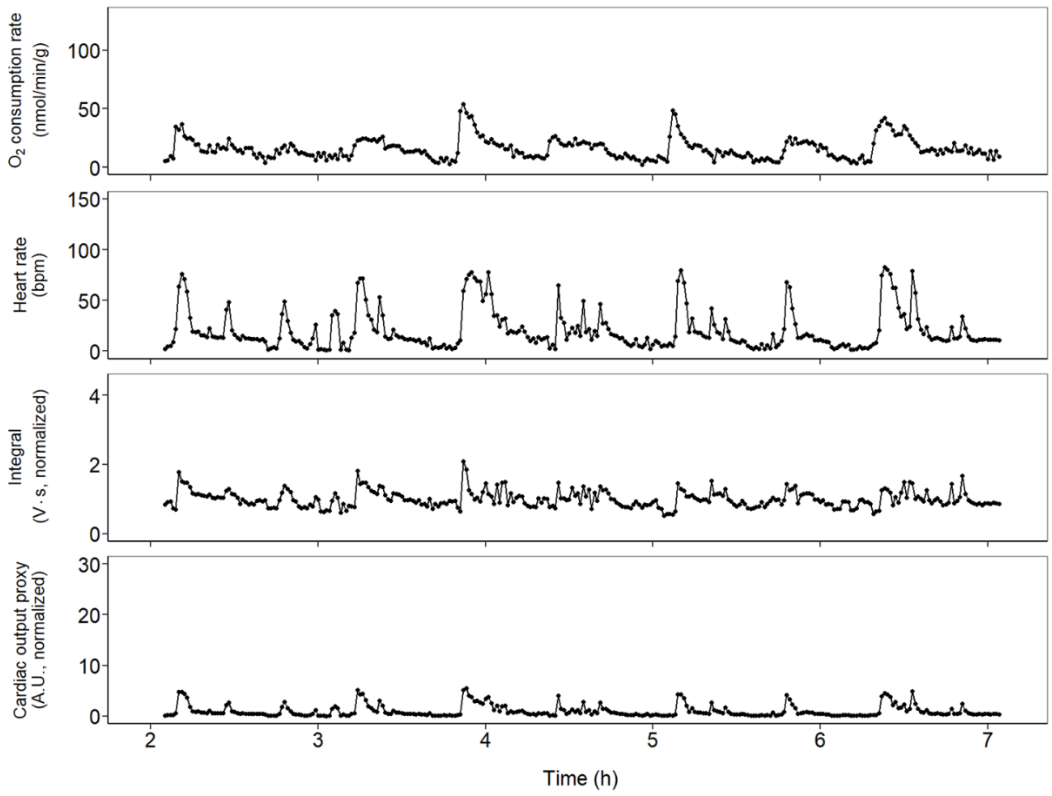

Fig. 52: Time course of cardiovascular parameters obtained for Cancer 4 at 12°C under hypercapnic conditions.

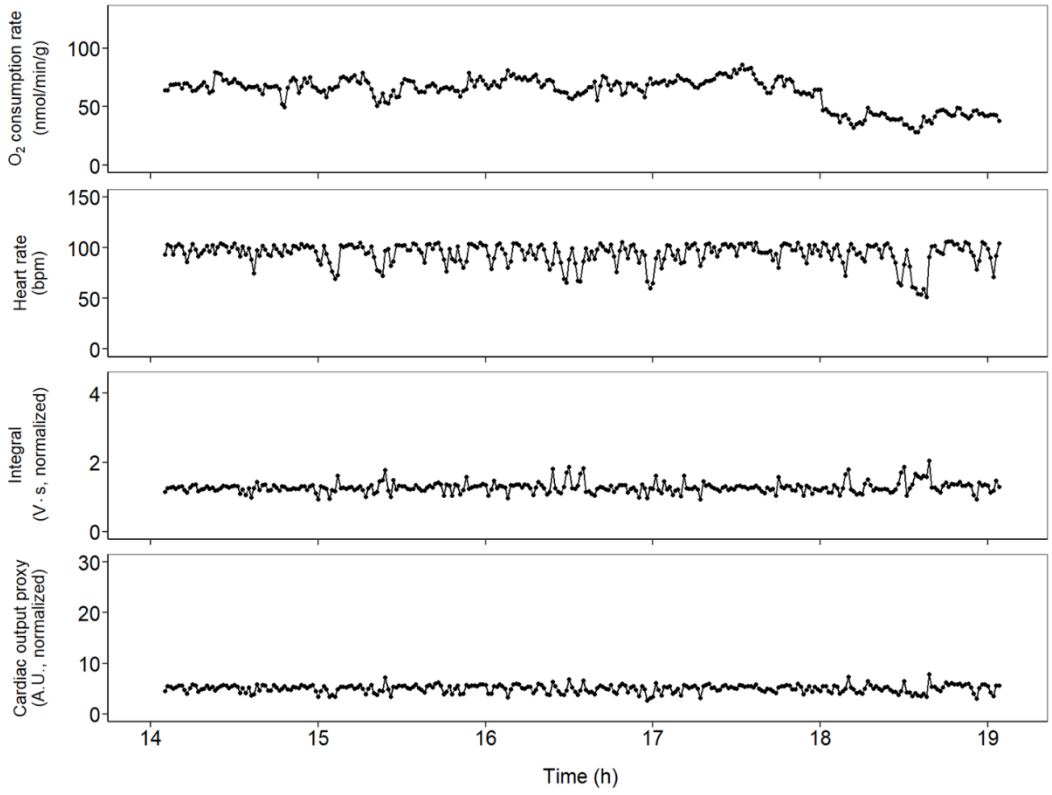

Fig. 53: Time course of cardiovascular parameters obtained for Cancer 4 at 14°C under hypercapnic conditions.

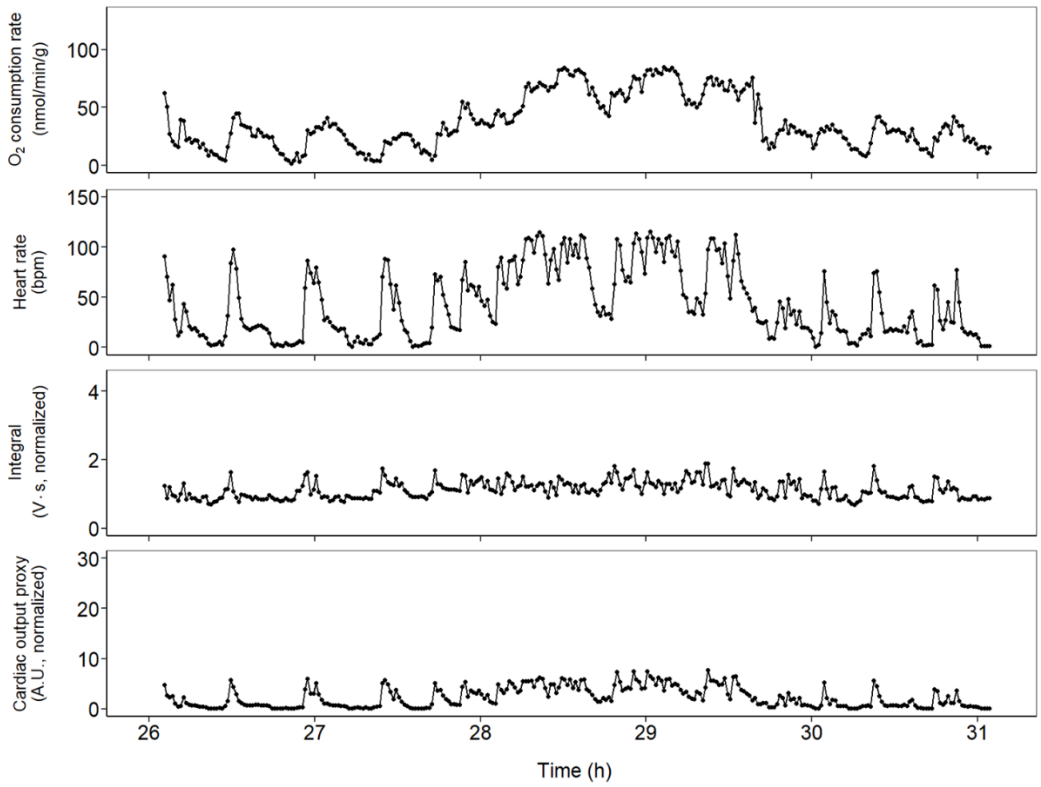

Fig. 54: Time course of cardiovascular parameters obtained for Cancer 4 at 16°C under hypercapnic conditions.

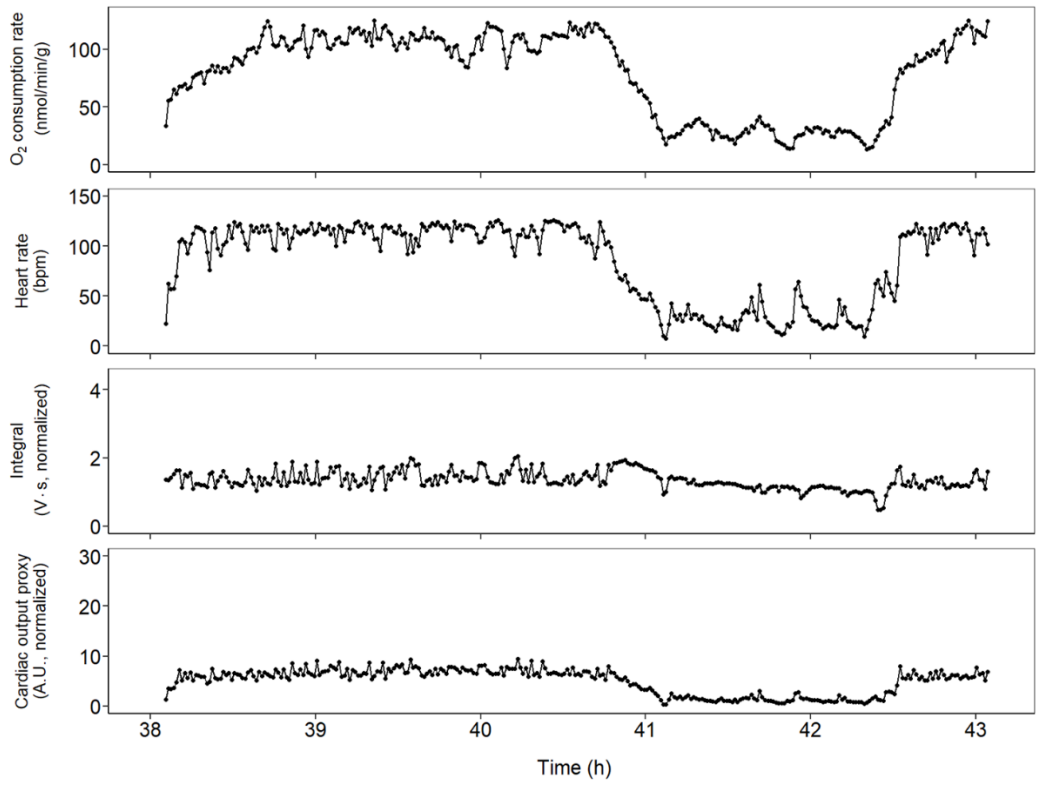

Fig. 55: Time course of cardiovascular parameters obtained for Cancer 4 at 18°C under hypercapnic conditions.

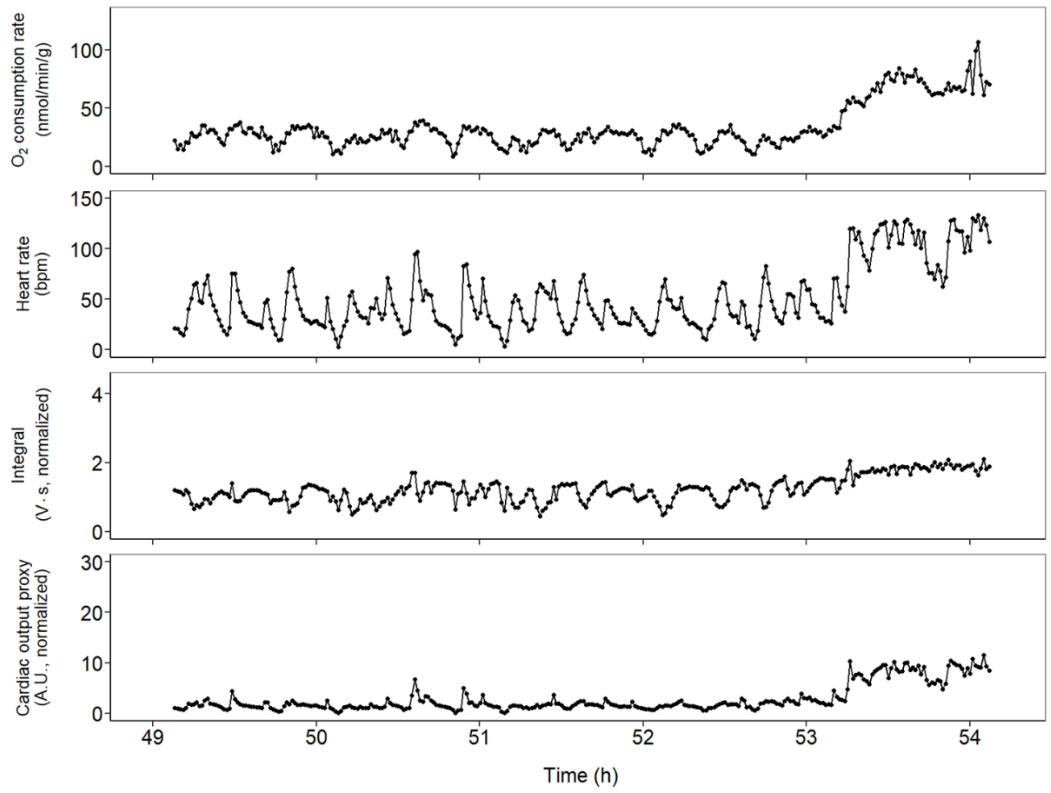

Fig. 56: Time course of cardiovascular parameters obtained for Cancer 4 at 20°C under hypercapnic conditions.

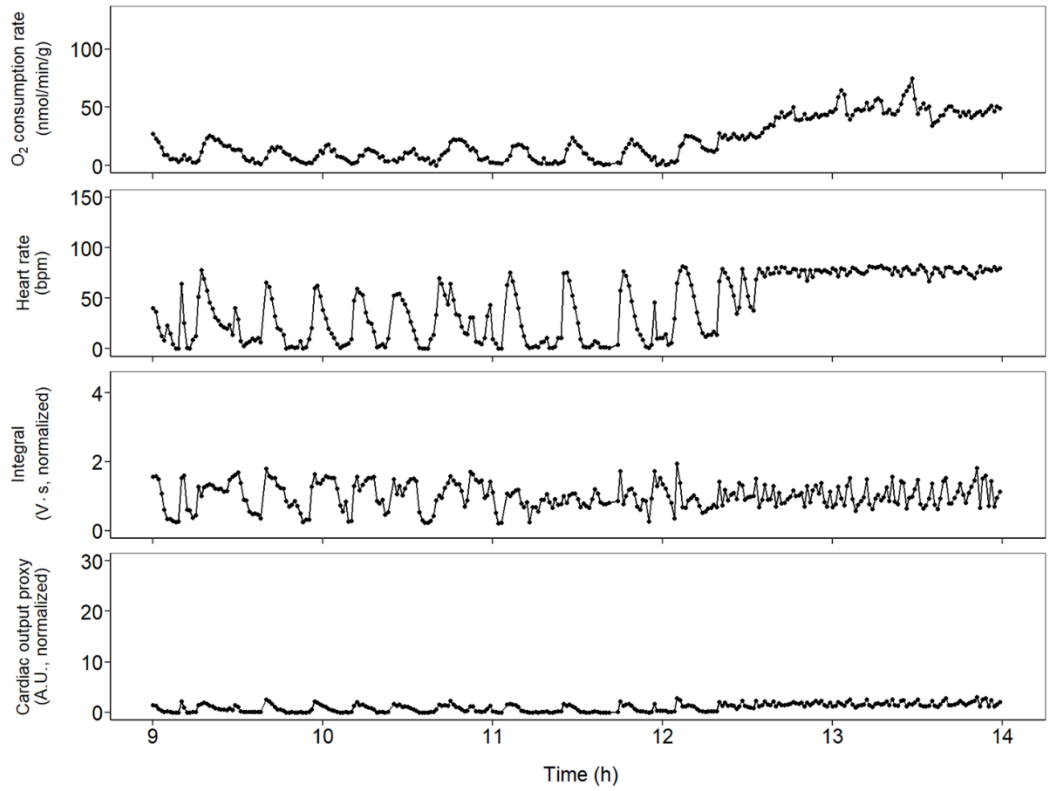

Fig. 57: Time course of cardiovascular parameters obtained for Cancer 5 at 12°C under normocapnic conditions.

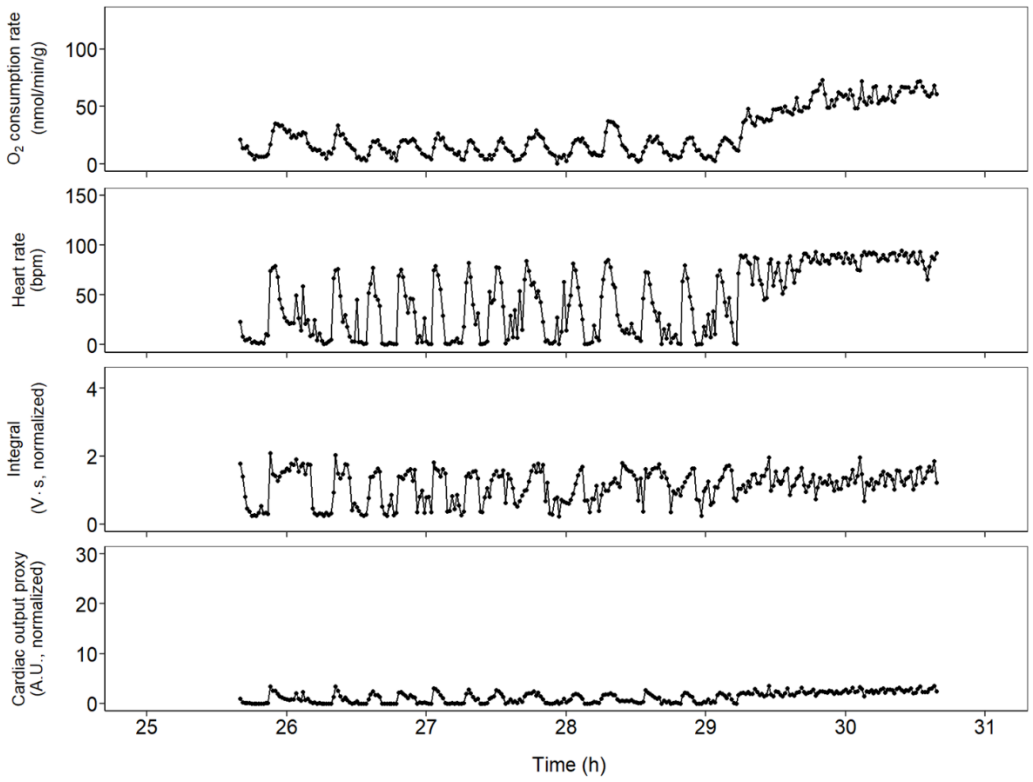

Fig. 58: Time course of cardiovascular parameters obtained for Cancer 5 at 14°C under normocapnic conditions.

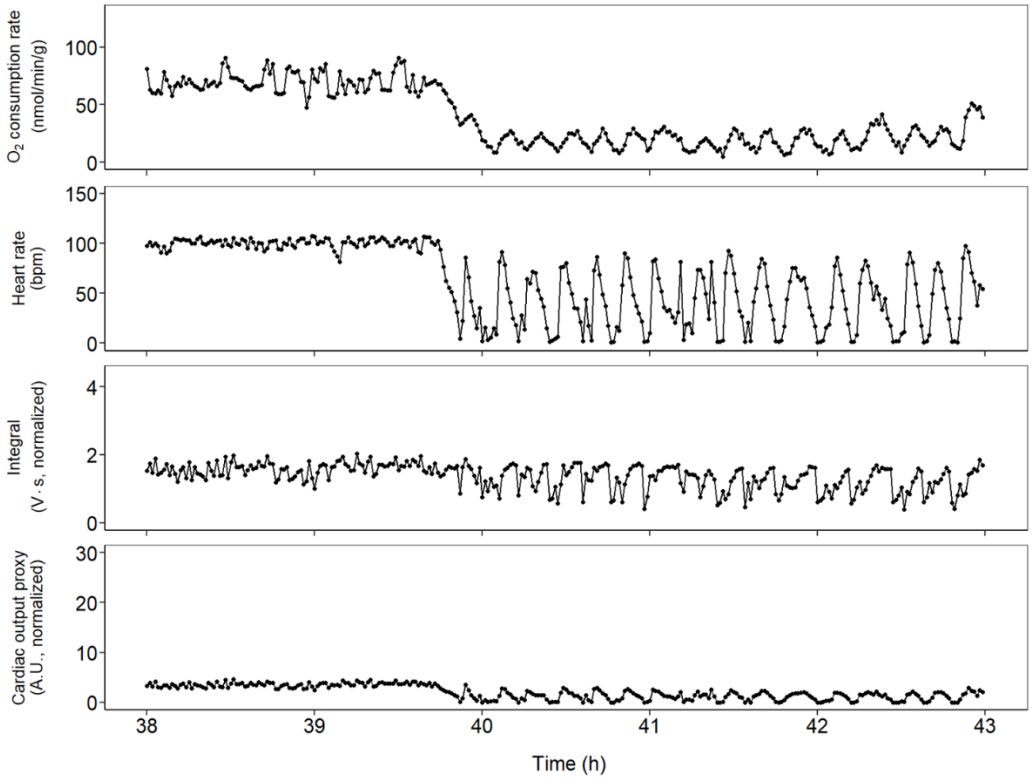

Fig. 59: Time course of cardiovascular parameters obtained for Cancer 5 at 16°C under normocapnic conditions.

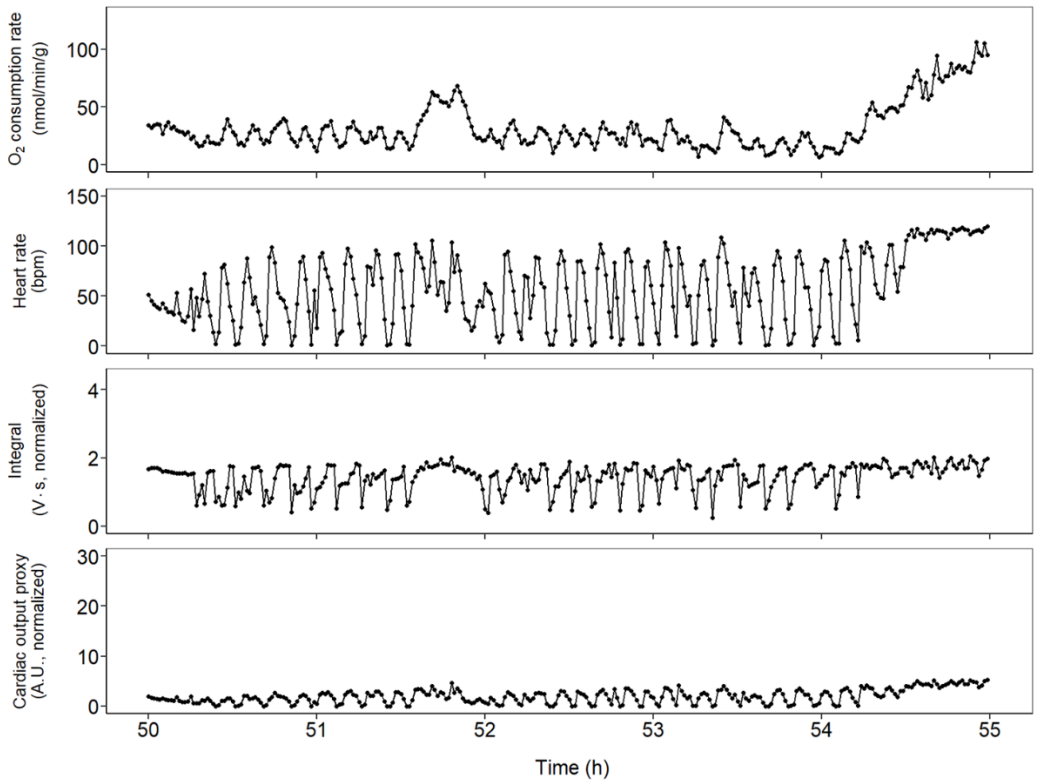

Fig. 60: Time course of cardiovascular parameters obtained for Cancer 5 at 18°C under normocapnic conditions.

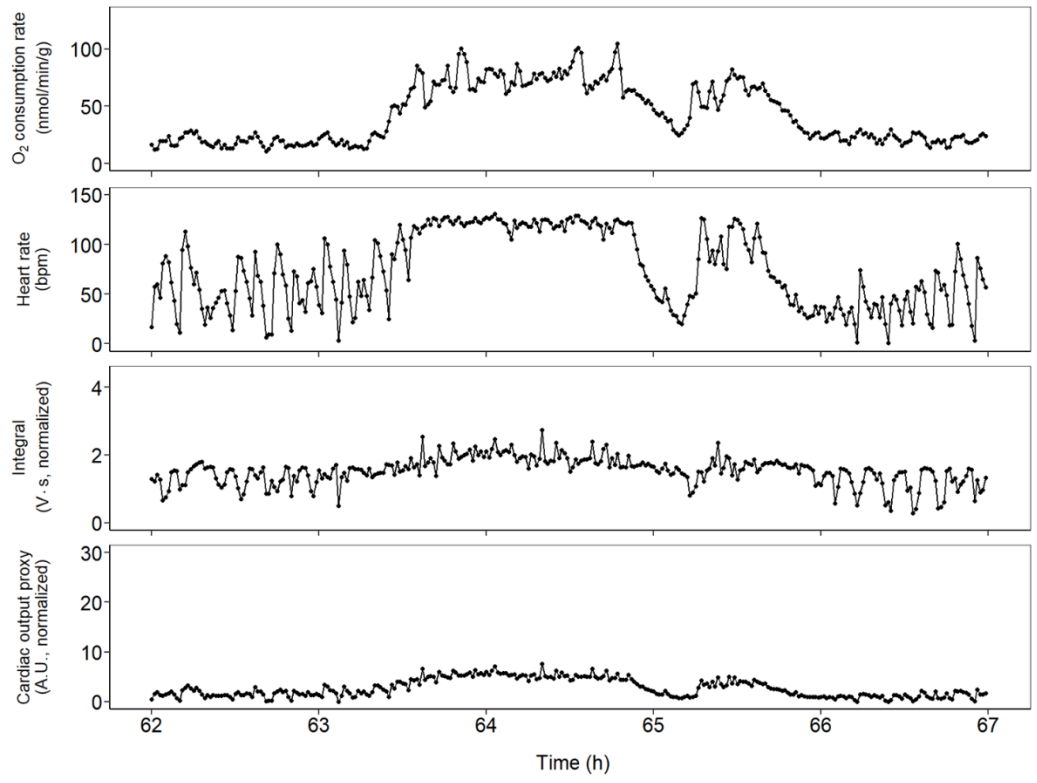

Fig. 61: Time course of cardiovascular parameters obtained for Cancer 5 at 20°C under normocapnic conditions.

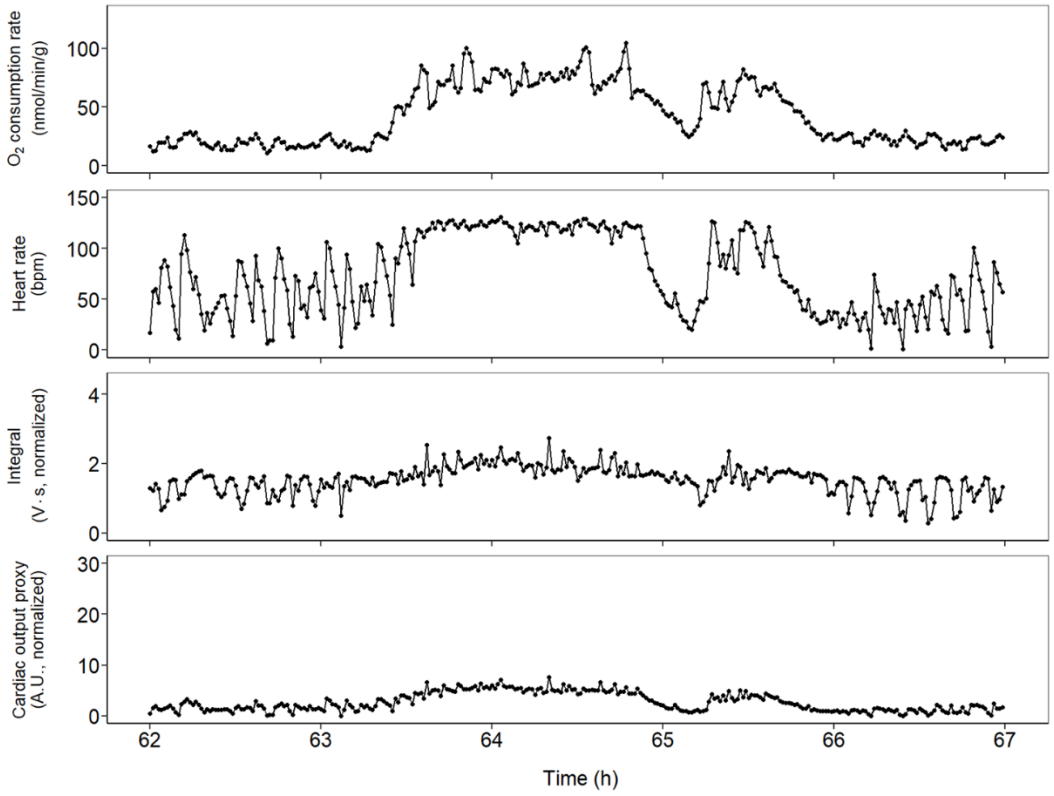

Fig. 62: Time course of cardiovascular parameters obtained for Cancer 5 at 12°C under hypercapnic conditions.

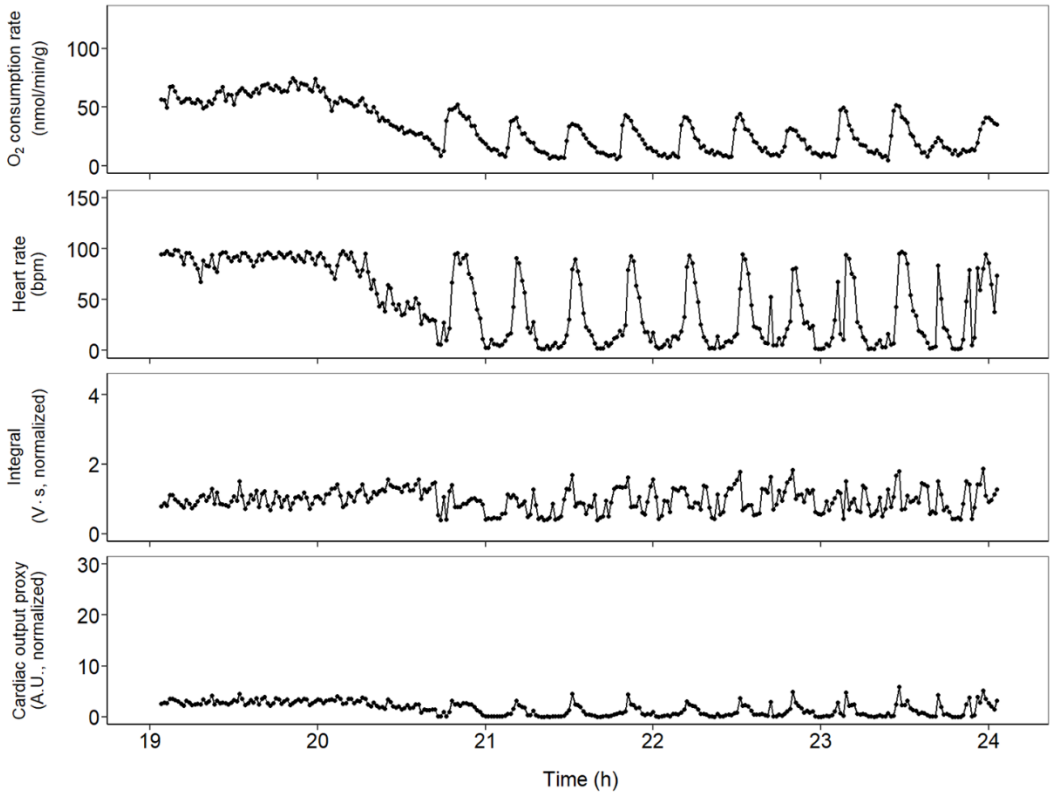

Fig. 63: Time course of cardiovascular parameters obtained for Cancer 5 at 14°C under hypercapnic conditions.

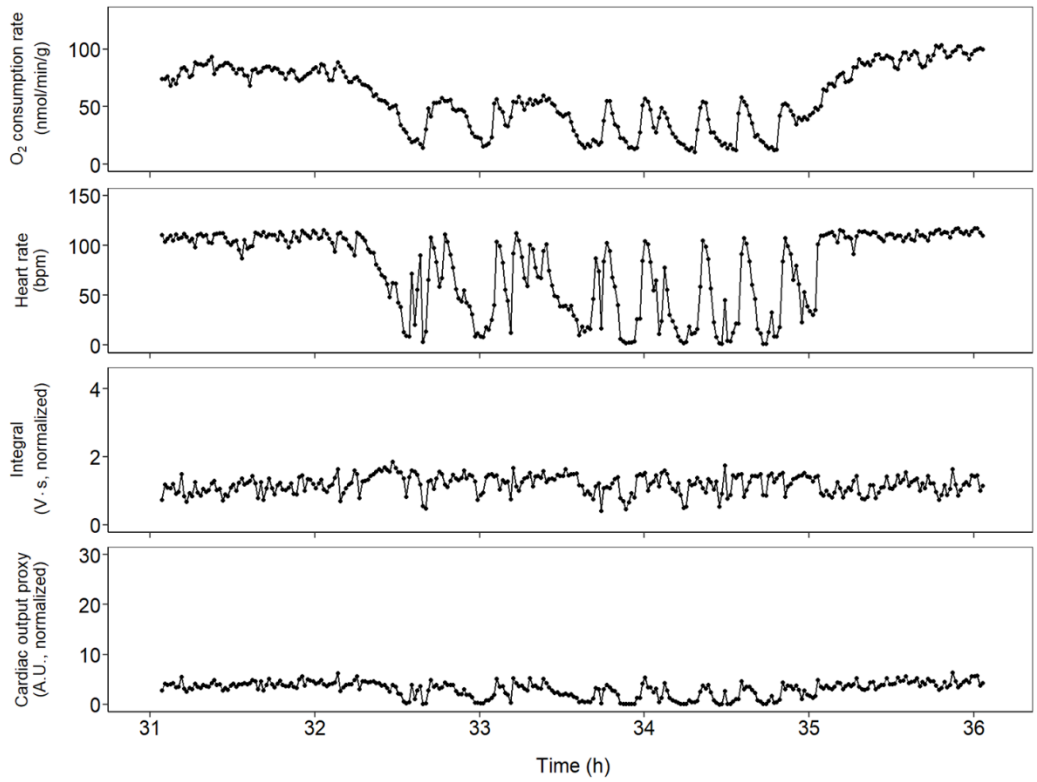

Fig. 64: Time course of cardiovascular parameters obtained for Cancer 5 at 16°C under hypercapnic conditions.

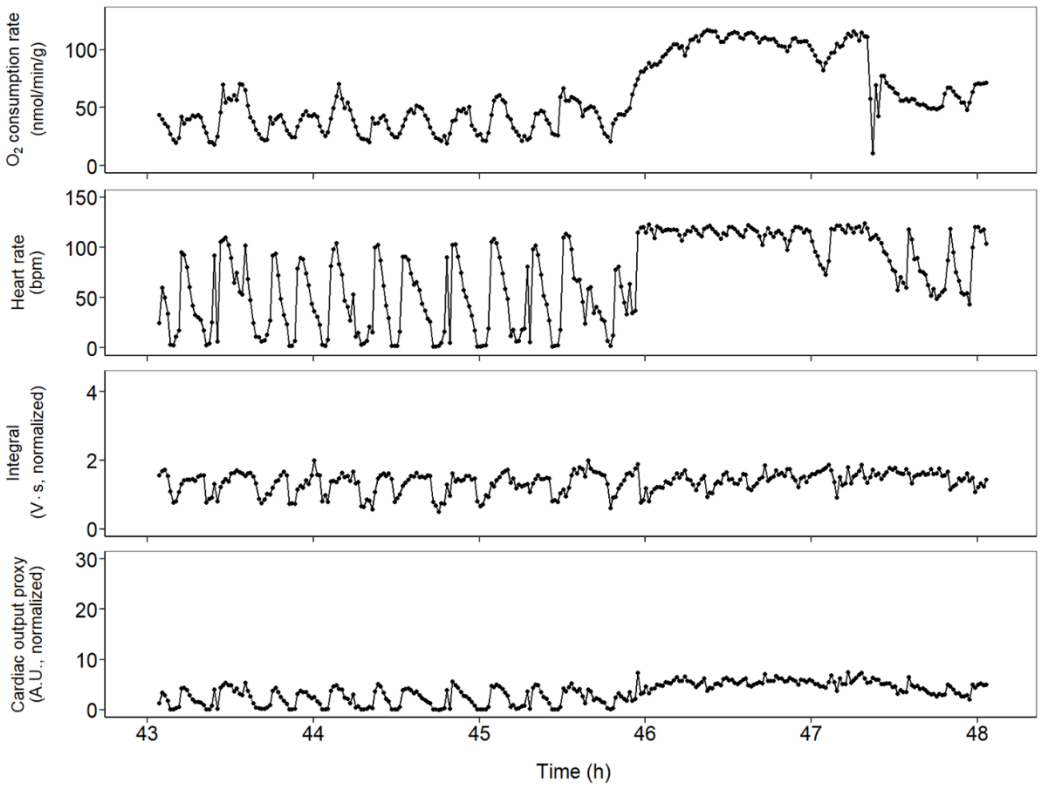

Fig. 65: Time course of cardiovascular parameters obtained for Cancer 5 at 18°C under hypercapnic conditions.

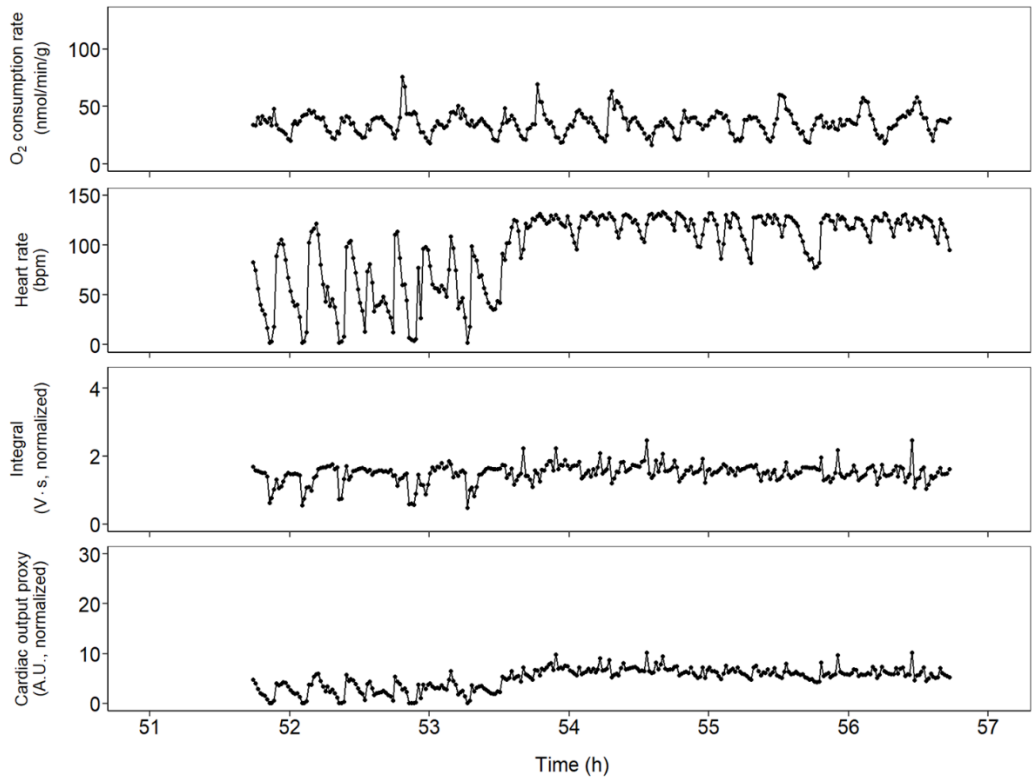

Fig. 66: Time course of cardiovascular parameters obtained for Cancer 5 at 20°C under hypercapnic conditions.

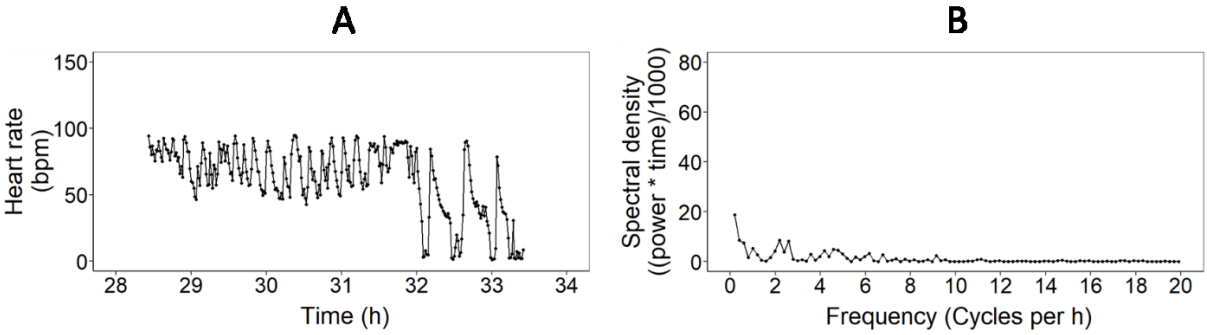

Fig. 67: Fast Fourier Transforms for the heart rates at 14°C of Cancer 1 under normocapnic conditions. (A) Time series of the heart rate. (B) Results of the FFT visualized as a spectral density plot of the underlying frequencies of the heart rate pattern.

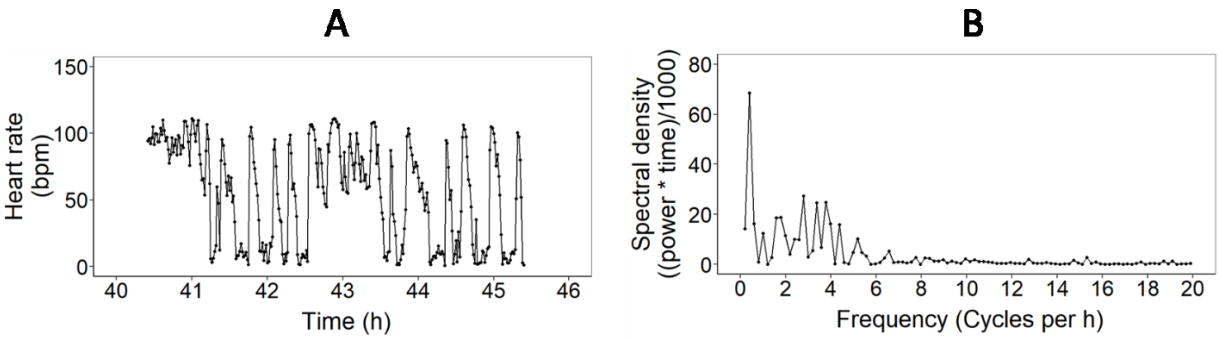

Fig. 68: Fast Fourier Transforms for the heart rates at 16°C of Cancer 1 under normocapnic conditions. (A) Time series of the heart rate. (B) Results of the FFT visualized as a spectral density plot of the underlying frequencies of the heart rate pattern.

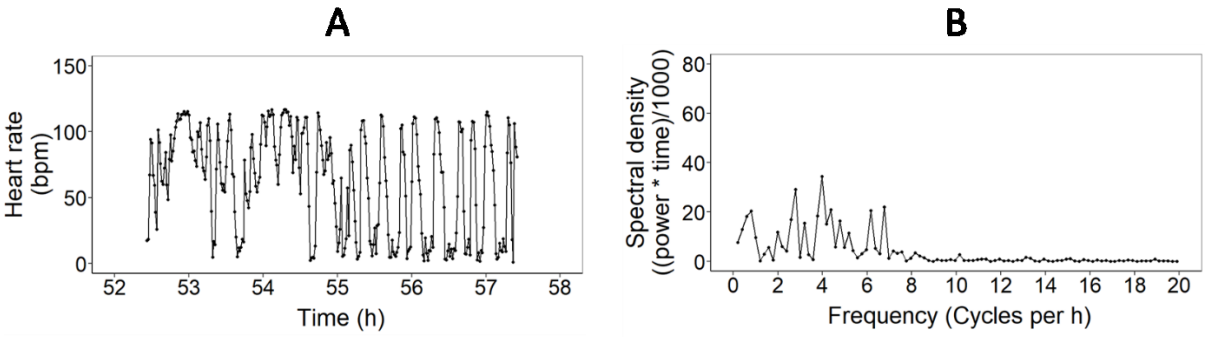

Fig. 69: Fast Fourier Transforms for the heart rates at 18°C of Cancer 1 under normocapnic conditions. (A) Time series of the heart rate. (B) Results of the FFT visualized as a spectral density plot of the underlying frequencies of the heart rate pattern.

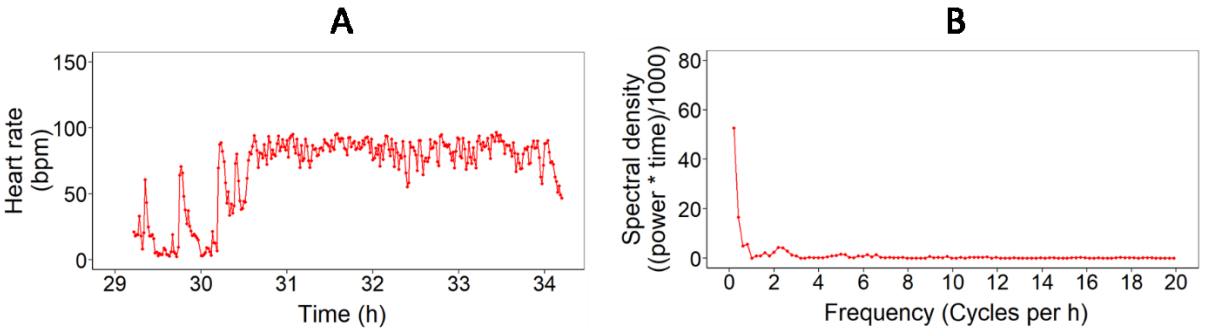

Fig. 70: Fast Fourier Transforms for the heart rates at 14°C of Cancer 1 under hypercapnic conditions. (A) Time series of the heart rate. (B) Results of the FFT visualized as a spectral density plot of the underlying frequencies of the heart rate pattern.

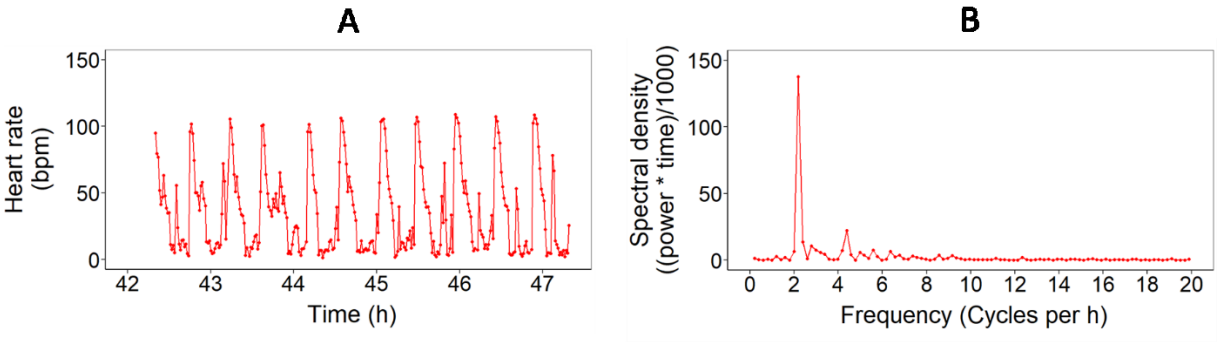

Fig. 71: Fast Fourier Transforms for the heart rates at 16°C of Cancer 1 under hypercapnic conditions. (A) Time series of the heart rate. (B) Results of the FFT visualized as a spectral density plot of the underlying frequencies of the heart rate pattern.

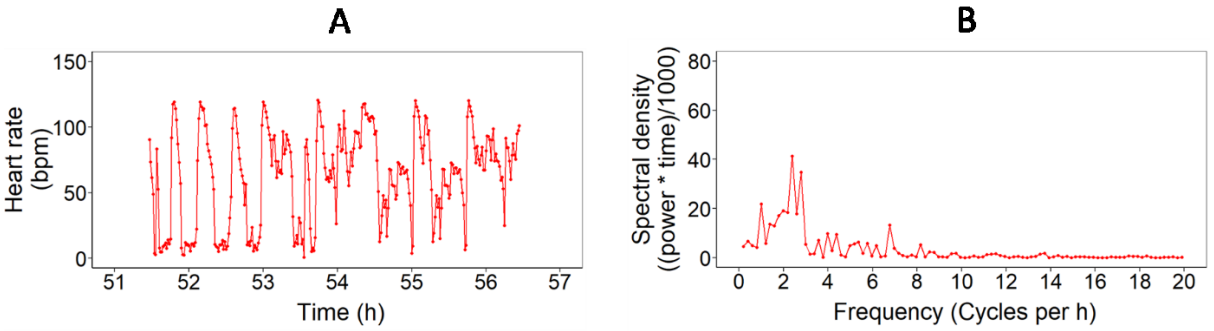

Fig. 72: Fast Fourier Transforms for the heart rates at 18°C of Cancer 1 under hypercapnic conditions. (A) Time series of the heart rate. (B) Results of the FFT visualized as a spectral density plot of the underlying frequencies of the heart rate pattern.

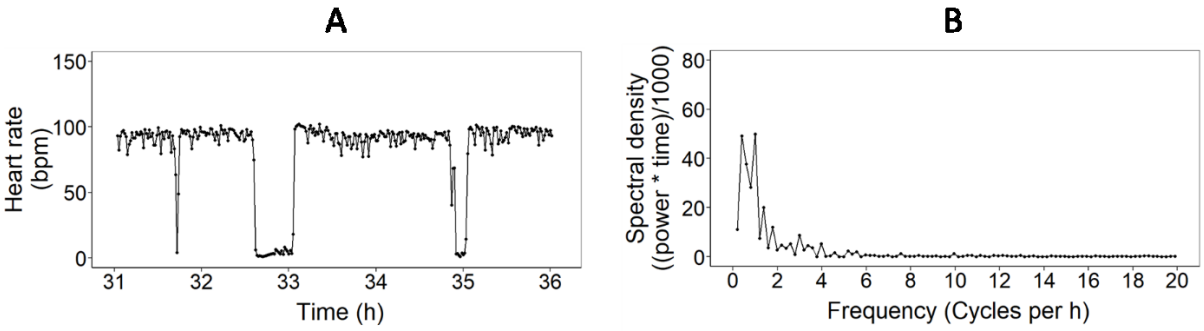

Fig. 73: Fast Fourier Transforms for the heart rates at 14°C of Cancer 4 under normocapnic conditions. (A) Time series of the heart rate. (B) Results of the FFT visualized as a spectral density plot of the underlying frequencies of the heart rate pattern.

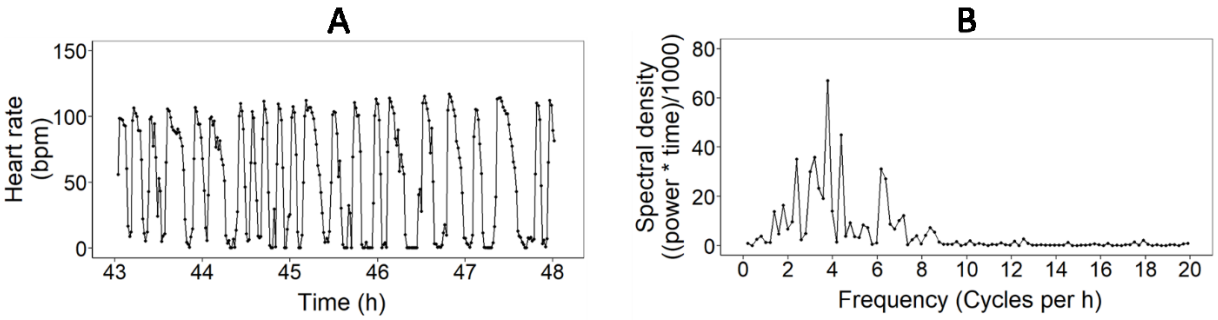

Fig. 74: Fast Fourier Transforms for the heart rates at 16°C of Cancer 4 under normocapnic conditions. (A) Time series of the heart rate. (B) Results of the FFT visualized as a spectral density plot of the underlying frequencies of the heart rate pattern.

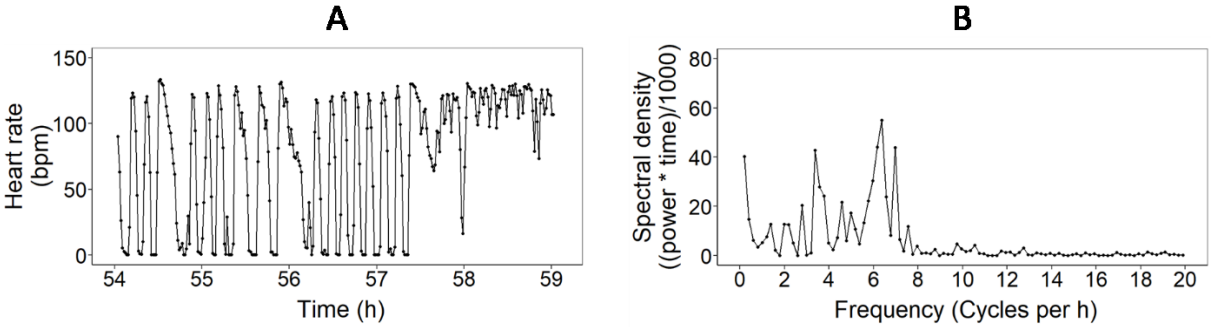

Fig. 75: Fast Fourier Transforms for the heart rates at 18°C of Cancer 4 under normocapnic conditions. (A) Time series of the heart rate. (B) Results of the FFT visualized as a spectral density plot of the underlying frequencies of the heart rate pattern.

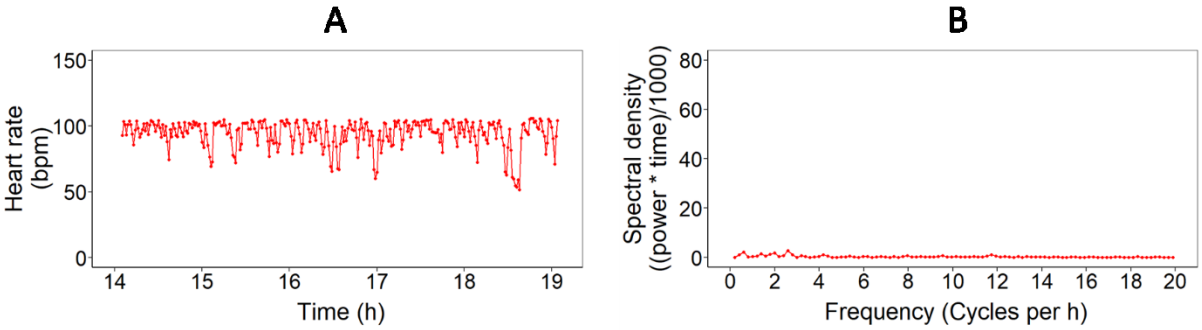

Fig. 76: Fast Fourier Transforms for the heart rates at 14°C of Cancer 4 under hypercapnic conditions. (A) Time series of the heart rate. (B) Results of the FFT visualized as a spectral density plot of the underlying frequencies of the heart rate pattern.

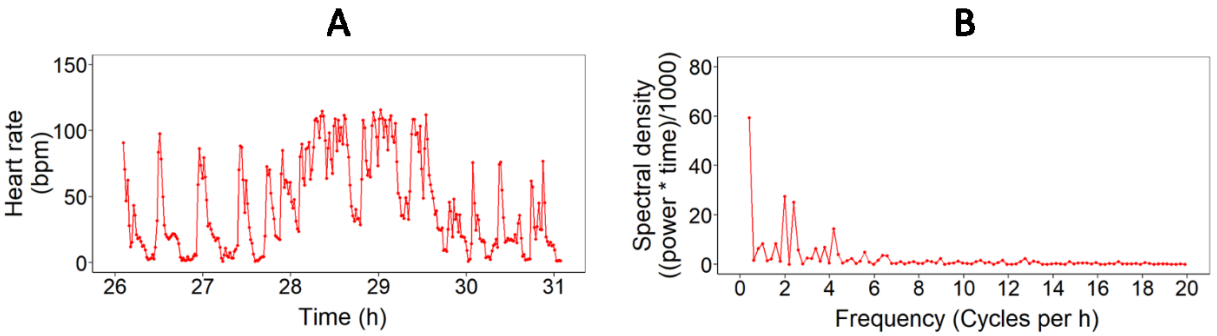

Fig. 77: Fast Fourier Transforms for the heart rates at 16°C of Cancer 4 under hypercapnic conditions. (A) Time series of the heart rate. (B) Results of the FFT visualized as a spectral density plot of the underlying frequencies of the heart rate pattern.

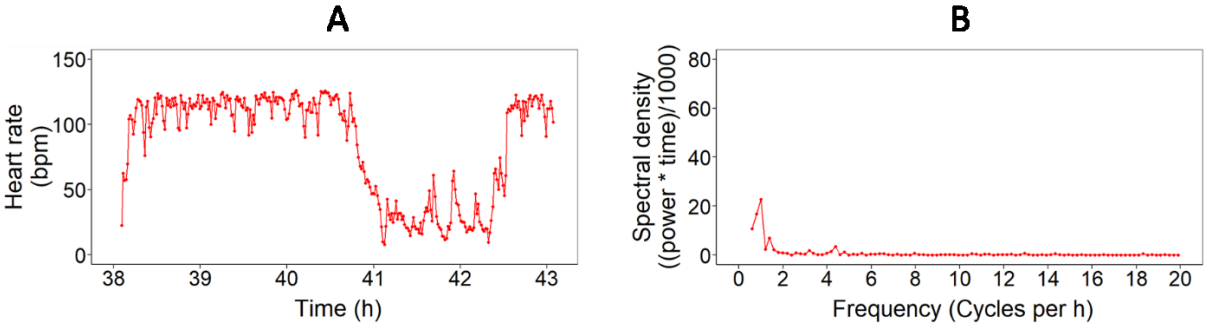

Fig. 78: Fast Fourier Transforms for the heart rates at 18°C of Cancer 4 under hypercapnic conditions. (A) Time series of the heart rate. (B) Results of the FFT visualized as a spectral density plot of the underlying frequencies of the heart rate pattern.

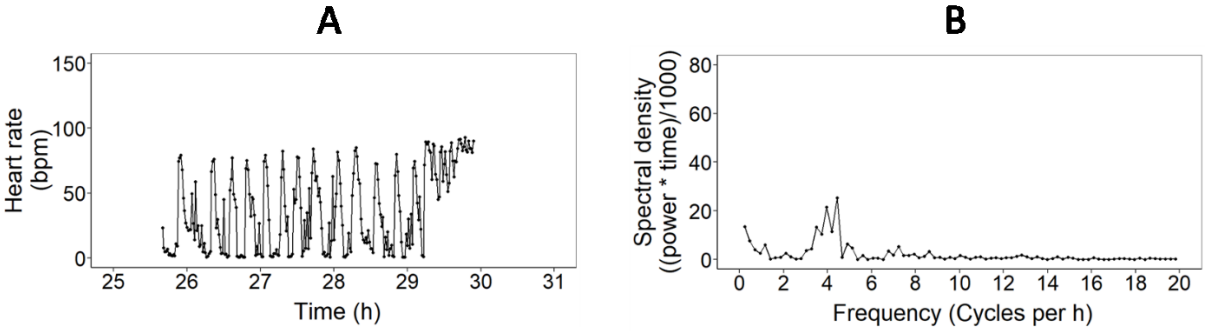

Fig. 79: Fast Fourier Transforms for the heart rates at 14°C of Cancer 5 under normocapnic conditions. (A) Time series of the heart rate. (B) Results of the FFT visualized as a spectral density plot of the underlying frequencies of the heart rate pattern.

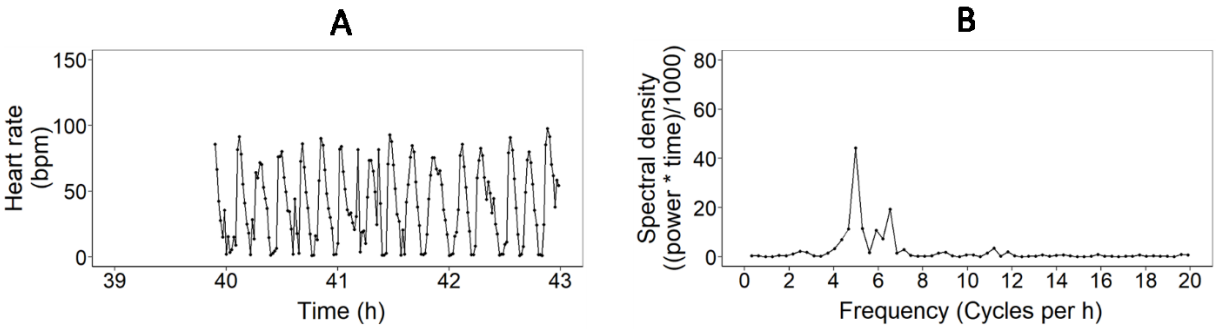

Fig. 80: Fast Fourier Transforms for the heart rates at 16°C of Cancer 5 under normocapnic conditions. (A) Time series of the heart rate. (B) Results of the FFT visualized as a spectral density plot of the underlying frequencies of the heart rate pattern.

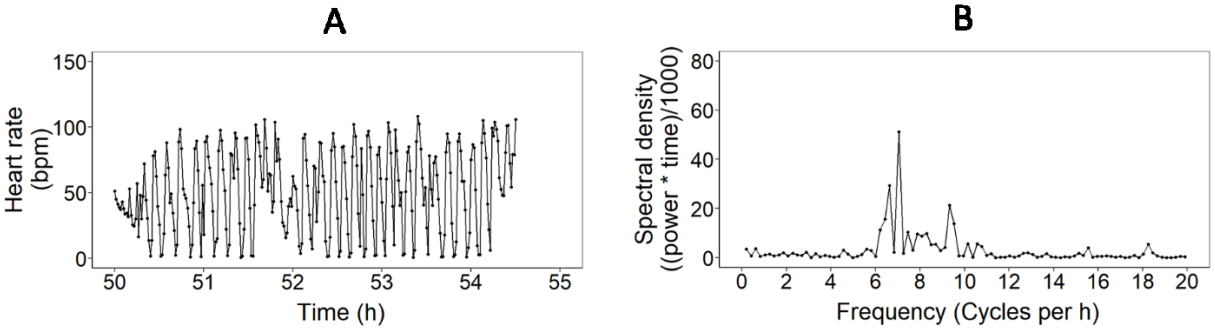

Fig. 81: Fast Fourier Transforms for the heart rates at 18°C of Cancer 5 under normocapnic conditions. (A) Time series of the heart rate. (B) Results of the FFT visualized as a spectral density plot of the underlying frequencies of the heart rate pattern.

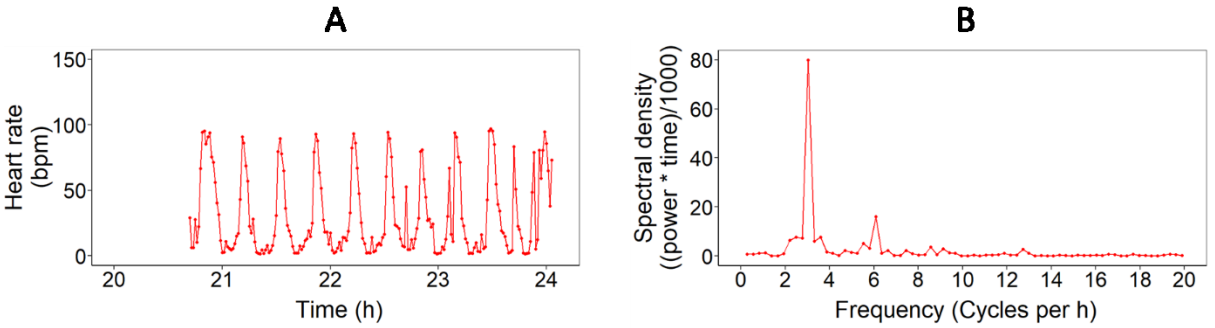

Fig. 82: Fast Fourier Transforms for the heart rates at 14°C of Cancer 5 under hypercapnic conditions. (A) Time series of the heart rate. (B) Results of the FFT visualized as a spectral density plot of the underlying frequencies of the heart rate pattern.

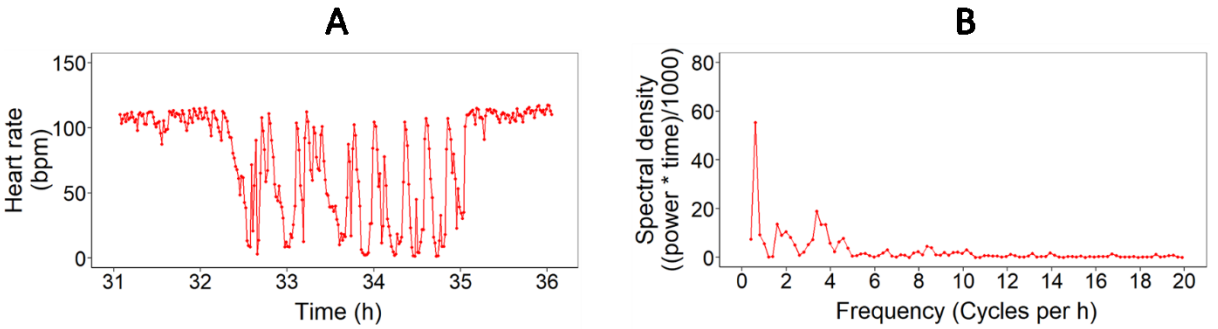

Fig. 83: Fast Fourier Transforms for the heart rates at 16°C of Cancer 5 under hypercapnic conditions. (A) Time series of the heart rate. (B) Results of the FFT visualized as a spectral density plot of the underlying frequencies of the heart rate pattern.

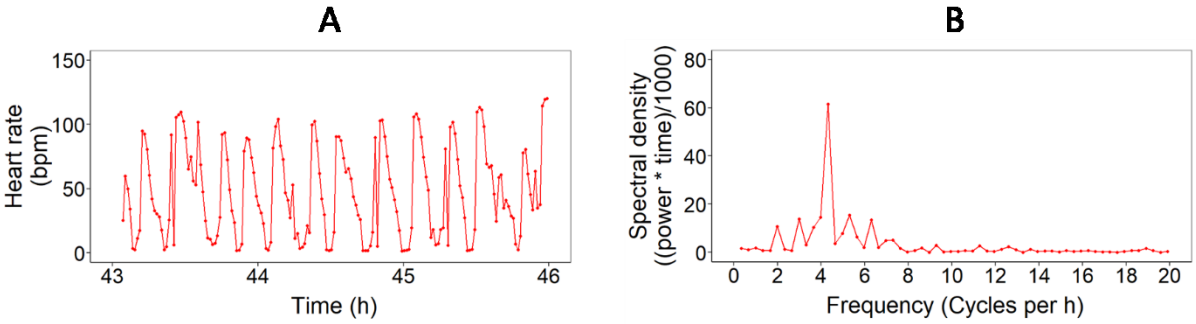

Fig. 84: Fast Fourier Transforms for the heart rates at 18°C of Cancer 5 under hypercapnic conditions. (A) Time series of the heart rate. (B) Results of the FFT visualized as a spectral density plot of the underlying frequencies of the heart rate pattern.

Acknowledgements

Firstly, I would like to thank Dr. Christian Bock and Prof. Dr. Hans-Otto Pörtner for giving me the opportunity to conduct my external Master-Thesis at the section of Integrative Ecophysiology at the AWI Bremerhaven.

Secondly, I would like to thank Dr. Michael Heethoff for undertaking the first supervision and Prof. Dr. Gerhard Thiel for undertaking the second supervision of this thesis at the TU Darmstadt.

Special thanks go to Dr. Christian Bock for his general supervision and Bastian Maus for his supervision of the practical work. Thank you for the very enjoyable working atmosphere, your patience, very helpful and constructive advises as well as countless (and necessary) crash courses in marine biology. As a non-marine biology student, I really enjoyed them as they helped me to better understand the bigger context of my project and the diverse facets of marine biology. Furthermore, thank you for your support during the writing process.

I would like to thank all the members of the section of Integrative Ecophysiology for their warm welcome, their helpful assistance, namely Charlotte Eymann, Sandra Götze, Anette Tillmann, Fredy Véliz Moraleda, Nils Koschnik, Dr. Daniela Storch and Dr. Astrid Wittmann concerning technical and theoretical questions, and the enjoyable atmosphere.

Furthermore, I thank Dr. Michael Heethoff and Dr. Sebastian Schmelzle for giving me the opportunity to conduct the 3D reconstructions at the working group for Ecological Networks at the TU Darmstadt. Special thanks go to Dr. Sebastian Schmelzle for his supervision of this process.

Last but not least, I would like to thank my family and Sarah for their support and understanding, not only during this thesis, but during my whole studies.